Experimental Investigation on the Morphology of Interstellar Ice Analogues

Mario Accolla

To cite this version:

Mario Accolla. Experimental Investigation on the Morphology of Interstellar Ice Analogues. Astrophysics [astro-ph]. Université de Cergy Pontoise, 2010. English. NNT : . tel-00609347

HAL Id: tel-00609347

https://theses.hal.science/tel-00609347

Submitted on 18 Jul 2011

If I have seen further,
it is by standing on
the shoulders of Giants
(Sir Isaac Newton)

Questo lavoro è dedicato alla mia piccola figlioletta,
e alla sua contagiosa voglia di vivere

Preface

Laboratory astrophysics is one of the youngest branches of Astrophysics. Specifically, it denotes the investigation of solid or gas phases in the different astrophysical environments by laboratory simulation experiments. Actually, prosperous developments in astrophysics would have been impossible without a strong laboratory background. So, for example, it was the case of spectroscopy: the interpretation of extraterrestrial absorption and emission spectra of dust, molecules, ions and radicals would have been impossible without the comparison with the laboratory ones.

Moreover, laboratory studies have allowed and allow the comprehension of many chemical and physical phenomena in the interstellar medium, as the origin and the evolution of some molecules. To date, around 150 molecular species have been tentatively or definitively identified in interstellar or circumstellar clouds[1]. However, the problem of their formation still remains in many case an open question. For instance, many papers have been dedicated to the problem of molecular hydrogen formation both through laboratory simulations (*Duley & Williams*, 1984; *Pirronello et al.*, 1997; *Manicó et al.*, 2001) and through numerical simulations (*Katz et al.*, 1999; *Cazaux & Tielens*, 2004; *Perets et al.*, 2005). Actually, H_2 is the most abundant molecule in the Universe, and it has been observed in a wide variety of galactic and extragalactic environments, such as diffuse or molecular clouds, PDRs, planetary nebulae, supernova remnants, AGN, etc. Although many steps forward

---

[1] You can find a list of the interstellar and circumstellar molecules continuously updated in the following web-site: *http://www.astro.uni-koeln.de/cdms/molecules*

have been taken, at the moment the problem of the H_2 formation is only partially understood. Anyway, it has been recognized that gas phase chemistry alone is not efficient enough to explain its observed high abundances. So, as long ago as 1963, *Gould & Salpeter* began to consider the possible interplay between gas and dust grains. Actually, grain surface chemistry is now recognized as the most efficient route to form H_2 and other simple molecules in environments where the ionization degree is low.
For this reason, chemical models and experiments have been aimed at describing the complicated chemistry that occurs on grain surfaces. So, an important part of the laboratory astrophysics (sometimes known as **Astrochemistry**) is dealing with the kinetics of grain surface reactions in astrophysical conditions. Astrochemistry, describing the different pathways by which the molecules are formed and destroyed, is today a firmly established subject (*Fraser et al.*, 2002). Although the extreme astrophysical environments are reproduced into a laboratory in a quite simplified manner, this kind of experiments try to reproduce in the conditions encountered in interstellar clouds in the short span of a few hours the chemical-physical reactions occurring there in thousands of years.

I spent about half of my Italian doctorate in the astrophysical laboratory in Cergy - Pontoise University (France), where I carried out all the experiments discussed in this thesis. The impressive experimental set-up housed in this laboratory (called **FORMOLISM**, i.e. **FOR**mation of **MOL**ecules in the **ISM**) has been developed with the purpose of studying the interaction of atoms and molecules and the chemical reactions among them on surfaces that simulate those of dust grains under interstellar conditions. Specifically, the surface chemistry investigated by FORMOLISM regards the interaction between gas and interstellar ice analogues. Indeed, laboratory simulations on icy samples allow us to understand why there is a great difference between gas and solid composition. It is known, in fact, that in dense molecular clouds, ices are irradiated by a weak flux of UV photons and by cosmic rays, that are able to break the chemical bonds of the species there present, and the fragments so created are able to recombine producing new chemical species that were not present within the ice. In the astrophysical laboratory, it is possible to simulate the effects induced by photons and energetic ions on the composition and morphology of the ices.
As it will be described in Chapter 1, in interstellar dark clouds dust grains

are covered with icy mantles, mainly constituted by amorphous solid water (**ASW**). Although the morphology of these ices plays an important role in the interstellar chemistry, to date we have poor knowledge about their internal structure. Within this picture, it lies the heart of the present thesis. In fact, the first set of experiments has been developed to study the gradual compaction of an highly porous ice following the atomic hydrogen exposure. The second set of experiments shows that the solid water formed through the hydrogenation of solid O_2 under ultrahigh vacuum conditions is amorphous with a rather compact (or non-porous) structure.

This thesis is organized as follows:

Chapter 1: The subject of this chapter is the interstellar medium (ISM). In particular, it has been dealt with the gas and the solid phase and their mutual interaction in the ISM, the different kinds of clouds and their chemical and physical characteristics. The aim of this chapter is to emphasize the astrophysical framework of the experiments performed, described and discussed in the Chapters 4 and 5.

Chapter 2: A quite detailed description of the different parts that form the set-up FORMOLISM (the laboratory equipment in Cergy-Pontoise University) is given in this chapter.

Chapter 3 : This chapter describes the experimental procedures used to carry out the experiments. Therefore, it is described the different methods of water ice growing used in our set-up, the TPD technique (by stressing its use as probe of ice morphology) and eventually the methods that allow to calibrate the flux of each experimental beam.

Chapter 4 : The present chapter deals with the description and the analysis of the experimental result that emphasize the gradual compaction of an highly porous interstellar ice analogues as consequence of the atomic hydrogen exposure.

Chapter 5 : The experiments discussed in this chapter study a water formation mechanism due to the hydrogenation of molecular oxygen. This water formation pathway seems to be very efficient in the interstellar conditions. Moreover, the water produced through this route is amorphous and with a compact structure.

Contents

Chapter 1

Astrophysical Framework: the Interstellar Medium

Borrowing a definition of Donald Osterbrock, we can say that *the interstellar medium is anything not in the stars.* Actually, the space among the stars is not empty, but is filled with a tenuous hydrogen and helium gas, and a sprinkling of heavier atoms and molecules, mixed with dust grains.

This matter is not uniformly spread out in space, but it is for the majority concentrated in very large regions, called **interstellar clouds** (look at the section 1.3). In the Milk Way, the galaxy to which the solar system belongs, clouds are concentrated along the spiral arms, but also occur in the regions between the arms and in the galactic halo, above and below the galactic plane.

In the past, the obscuration due to the interstellar medium was regarded merely as a hindrance to the observation of astronomical objects as stars and galaxies. Therefore, the efforts that astronomers made were simply to find ways of accounting for the extinction of the light of distant objects as accurately as possible, so that the propriety of stars and galaxies might be accurately known. Gradually, however, it became clear that the obscuring medium was interesting in itself. As a matter of fact, for instance, interstellar clouds take legitimately part in the cyclic process of stellar evolution.

In fact, dense regions inside molecular clouds can be considered proper *stellar nurseries*: their chemical-physical characteristics allow the gravitational collapse of dust and gas, thereby giving life to stellar objects. On the other hand, interstellar material is continuously yielded by stellar winds and supernovae explosions. In this way, the metal contents of the interstellar medium is continuously enriched with heavier elements synthesized during the nucleosynthesis taking place in the various evolutionary stages of stars.

In the visible part of the electromagnetic spectrum, it is the dust responsible for the interstellar extinction, namely the partial blocking of starlight, that arises from two physical processes, *scattering* and *absorption.*

Hence, the ISM is not just detritus of previous generations of stars that blew out matter in the form of dust particles and gas; it is also the site where all the interactions between matter and the different energetic sources (such as cosmic rays, ultraviolet radiation fields, X-rays, shock waves generated by supernovae explosions, gravitational and magnetic fields, etc) take place. For this reason, this astrophysical environment is as much physically and chemically complex as crucial to understand the lifecycle of stars in the Galaxy and hence the structure and the dynamics of the galaxy itself.

1.1 The Milk Way

The Milk Way is a spiral galaxy that can be represented as a disc with a spheroidal bulge, and some spiral arms. Fig.1.1.1 shows a schematization of the Milk Way, while Fig.1.1.2 shows what we are able to observe at different wavelengths from our position in the Galaxy.

It was *H. Shapley* that in the early 1920s determined for the first time the position of the solar system into the Galaxy. In fact, from the observation of *Cepheids* and *RR Lyrae variables*[1], he found that the majority of the observable star clusters (called *globular clusters*) form a spherical distribution. The center of this distribution coincides with the center of the Galaxy and it

---

[1] *Cepheids* and *RR Lyrae variables* are two particular classes of pulsating variable stars. They present two important characteristics: first of all, it is not hard to know their mean absolute magnitude; then, there is a quite precise relationship between the variable luminosity and the pulsation period. As the difference between absolute and relative magnitude is the distance modulus, the observation of these variable stars provide us two methods of measuring distances, even in other galaxies.

is about 10 *kpc* [2] far from the Sun. Moreover, the Sun moves in a quasi circular orbit around the center of the Galaxy, with a rotation period of about 2.3×10^8 *years*.

According to their abundances of metals, we refer to high metal stars as *Population I* and low metal stars as *Population II*. Population I stars are

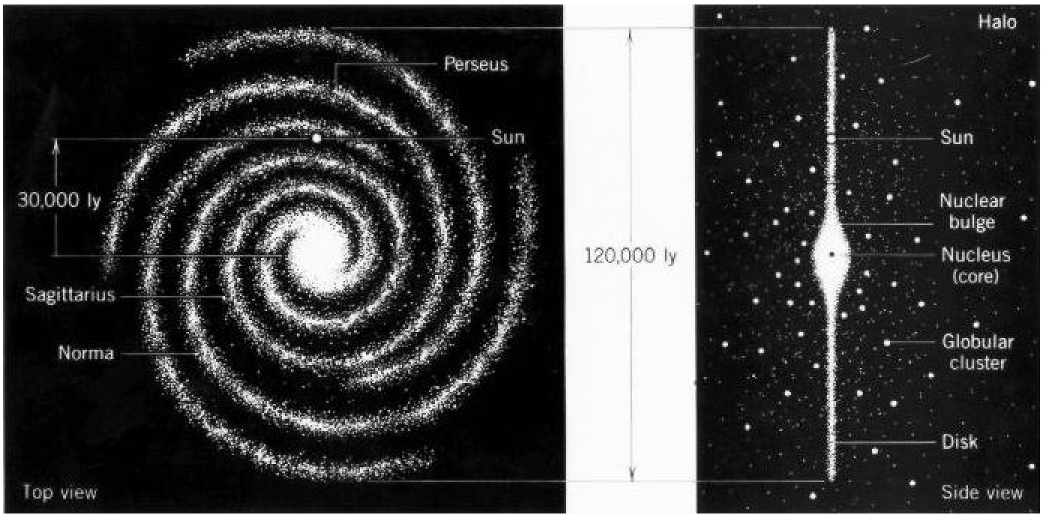

Figure 1.1.1: Schematic drawn of our Galaxy, the Milk Way. Top and side view are shown here.

---

[2] In Astronomy, the *parsec* (abbreviated **pc**) is a basic unit of length.

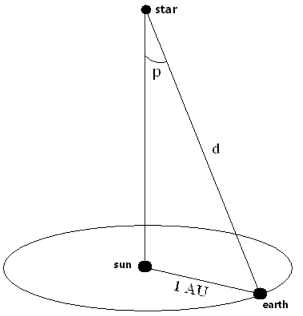

1 *pc* is defined as the distance (**d**) from the Earth to an astronomical object which has a parallax angle (**p**) of 1 *arcsecond*.

$$1\ pc = 2.06 \times 10^5\ AU = 3.26\ light\ years$$

confined to the galactic plane: they are young enough to have some of their parent cloud around them. On the contrary, Population II stars have no gas and dust around them. They are found in globular clusters and for this reason form a spherical distribution (the so-called halo).
Therefore, the halo consists of the oldest stars known and it is also filled with a very diffuse, hot, highly ionized gas. The spiral arms of our Galaxy contain the interstellar matter, diffuse nebulae, young stars and open clusters emerging from this matter. Because of the difficulties of studying the spiral arms in our Galaxy, much of our understanding of spiral structure comes from comparing our Galaxy to other galaxies. Thus, for instance, it has been observed that spiral arms are sites of ongoing star formation and are brighter than the surrounding disc because of young, hot OB stars that inhabit them.
Finally, the visual extinction in the galactic plane makes optical studies of the galactic centre virtually impossible. On the contrary, we are able to observe the galactic centre in the radio and in the infrared parts of spectrum. It is known that the centers of many other galaxies are not simply geometrical locations, but they are sites of unusual activity. Even in the Milk Way, some evidences seem to suggest the presence of a central object, that might be a few million $M_\odot$ black hole. However, this is an hypothesis, still to be confirmed.

1.2 The interstellar medium

The interstellar medium (**ISM**, for short) fills the volume of space among the stars and accounts for 10 - 15% of the total barionic mass of the Galaxy. The gas represents about 99% by mass of the ISM, while the remainder 1% by mass is in the form of dust grains. Usually, gas and dust are well mixed in the clouds: in fact, the 21 cm line emission (due to the spin flip transition in the atomic hydrogen) is strictly related to the optical obscuration due to the presence of dust. Actually, it is the interaction between gas and dust that allows the formation of new molecules or the accretion of dirty ices on the grain surface.
Gas and dust will be the object of the next two subsections.

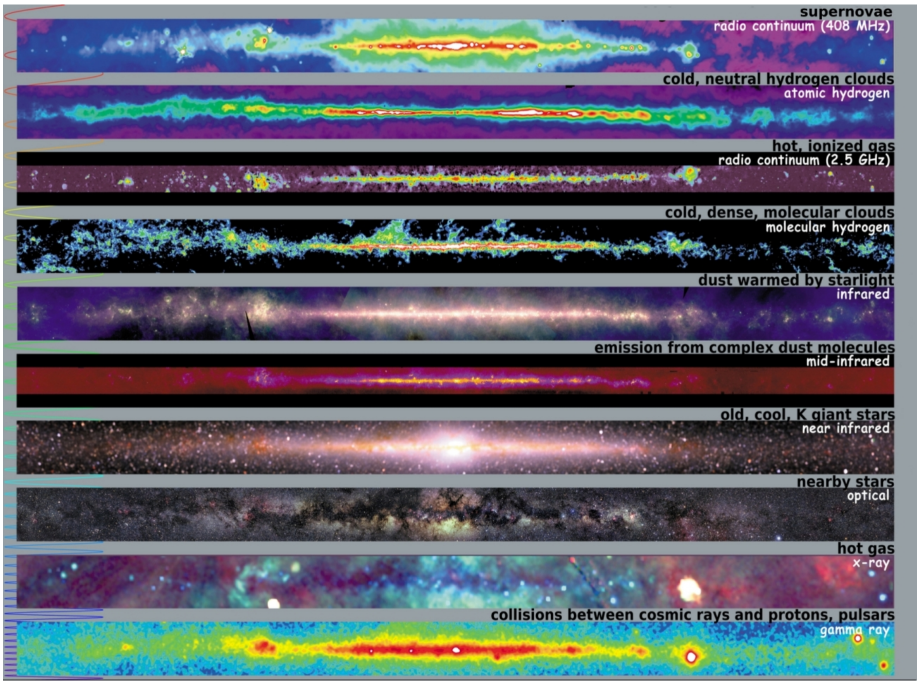

Figure 1.1.2: Images that show the Milk Way at different wavelenghths (*http://adc.astro.umd.edu/mw/*).

1.2.1 The interstellar gas

The chemical composition of the interstellar matter is close to the so called *cosmic composition* inferred from element abundances in the Sun. Thus, interstellar gas consists mostly of hydrogen ($\sim$ 90% by number) and helium ($\sim$ 10 % by number). Oxygen, carbon and nitrogen comprise about 0.1% by number; all other elements are present only in trace quantities. Because of its higher abundance with respect to the dust, it is the gas that determines the main characteristics of an interstellar cloud. For this reason, as it will be discussed in one of the next sections, interstellar clouds are classified according to the form in which the hydrogen is found.
Earlier studies of cold interstellar gas utilized optical absorption lines. When the light of an embedded object in the star-forming region or the light from a star passes through a cloud (*field star*), some energy is removed at wavelenghts corresponding to the transitions in the atoms and molecules (see Fig.1.2.1). These studies have allowed the identification of many species (*Snow*, 1980), some of them result unstable in terrestrial laboratory. However, no hydrogen adsorption line can be observed in this way: in fact, most of the hydrogen is in its ground state because of the low temperature in clouds. Therefore, *Lyman lines* are the only spectroscopic features of H detectable in the far ultraviolet by satellites.

Most of what we know about the interstellar gas comes from radio observations. In the early 1950s, *Purcell* and his collaborators made the first detection of the *21 cm hyperfine structure line* from interstellar neutral atomic hydrogen[3]. At once, the extensive observation of the 21 cm line became a powerful tool for studying the interstellar gas. In fact, as the interstellar dust is transparent at radio wavelengths, radio telescopes are able to detect objects across the Galaxy, far beyond what we can see optically in the presence of dust. However, in this way, it is possible to map only the clouds in which the hydrogen is mostly in the atomic form (the so called *HI clouds*). About

---

[3] Atomic hydrogen in the ground electronic state can produce a radio line at wavelength of 21 cm. This line is due to the *hyperfine splitting* arising from the spins of the proton and the electron changing from a parallel to an anti-parallel configuration, and vice versa. Indeed, electron and proton spins can be either parallel and anti-parallel. To the state with the spins of the protons and the electron parallel corresponds a higher energy than to the state with spins anti-parallel. The atom can undergo transitions between these two states: their energy difference (of the order of 10^{-6} eV) corresponds to a frequency of about 1400 MHz ($\lambda \approx 21$ cm)

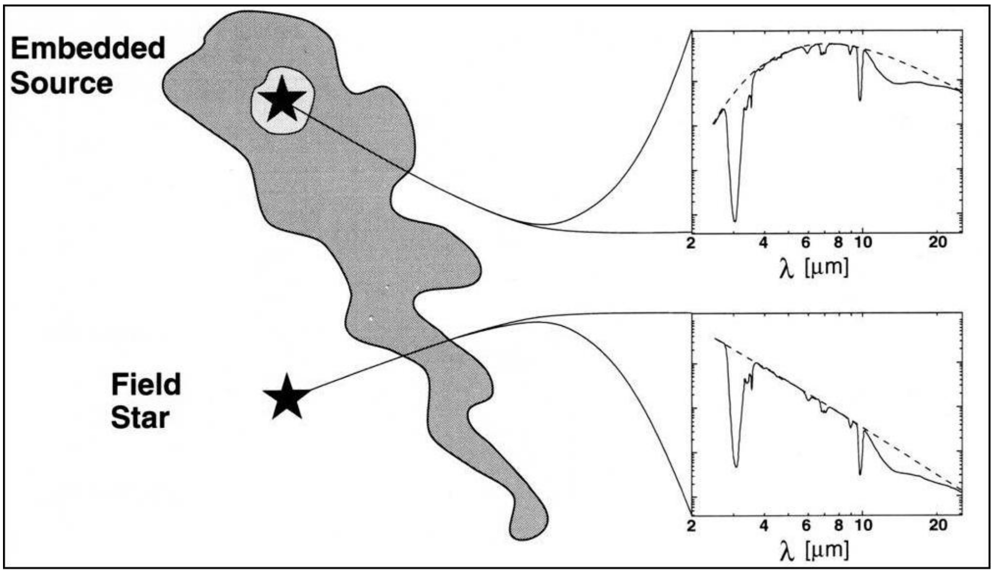

Figure 1.2.1: The interaction between the starlight and the interstellar matter that lies along roughly the same line of sight allows to study the elements that populate the cloud.

the clouds in which the hydrogen is mostly molecular (*molecular clouds*), other methods have to be used.
Actually, in the Universe, H_2 is the most abundant molecule by far, but it is also the most elusive: in fact it is a homonuclear diatomic molecule, and for this reason it has not permanent electric dipole moment, which means that only quadrupole transitions are allowed by which H_2 molecule can radiate. Thus, cold H_2 is invisible for radio or sub-mm observations. As the majority of the cold H_2 remains invisible to direct study, most of our knowledge about the H_2 contents is estimated only indirectly, coming from observations of other molecules, primarily CO that is the second most abundant molecule in the ISM ($10^{-4} - 10^{-5}$ times the hydrogen abundances). Thus, in molecular clouds, H_2 makes its presence felt by forcing the electronic transition J = 1-0 of the carbon monoxide, observed in the millimetric region of spectrum. In fact, when an H_2 strikes a CO, H_2 can loose kinetic energy, by exciting collisionally CO to a higher roto-vibrational energy state; when CO de-excites radiatively emitting a photon, it carries to the observer the information of the presence of molecular hydrogen, that is most frequent collisional partner

of CO. In rarer cases, H_2 can gain kinetic energy de-exciting CO.

The ratio of the abundances of molecular to atomic gas (H_2 / H) varies as a function of position in our Galaxy. Molecular hydrogen is most tightly confined to the plane of the Galaxy, with vertical scale height above or below the Galactic midplane of roughly 90 *pc*. On the contrary, atomic hydrogen can be found in the region from 3 *kpc* out to the edge of the Galactic disk. In the solar neighbourhood the total mass density of gas is 0.04 $M_{\odot}\ pc^{-3}$, of which atomic hydrogen accounts for approximately 77%, molecules contribute for about 17% and ions add an additional 6%.

The optically obscured regions of ISM are dominated by H_2 and are underabundant in atomic H, whereas regions irradiated by strong radiation fields are dominated by atomic H. The problem of H_2 formation at a rate compatible with estimated abundances and the photo-dissociation has been investigated by several authors both from a theoretical point of view (recently *Cazaux & Tielens*, 2004; *Perets & Biham*, 2006) and from an experimental one (e.g. *Pirronello et al.*, 1997; *Manicó et al.*, 2001; *Hornekær et al.*, 2003).

It has long been recognized that hydrogen recombination ($H + H \rightarrow H_2$) occurs with high efficiency on surfaces of interstellar dust grains (that serve as catalyst for this process) under a wide range of physical condition. On the contrary, it is widely accepted that gas phase routes for the conversion of hydrogen atoms to molecules are not rather efficient to account for observed H_2 abundances (*Hollenbach & Salpeter,* 1971).

1.2.2 The interstellar dust

Although dust grains contribute only approximately 1% of the barionic mass in interstellar clouds, they play a crucial part in the interstellar chemistry and in the evolution of clouds. Indeed, dust grains act as catalyst in ISM, allowing the atoms adsorbed on the surface to move along their surface, meet each other and react. The grains also allow the newly formed molecules to lose their energy, and therefore prevent them from redissociating once they are formed (it is the case, for instance, of the molecular hydrogen).

Many evidences confirm the presence of solid small particles in the ISM, with a range of sizes between 1 *nm* and 3 *µm* [4]. First of all, the so called

---

[4] It is possible to estimate grain sizes, studying the variation of the interstellar extinction with the wavelength. So, if the grain size r is much greater than the wavelength λ,

extinction curve of starlight in the visible and ultraviolet wavelengths, due to the scattering and the absorption of the starlight. The amount of extinction is wavelength-dependent: the shorter the wavelength, the higher the extinction. Thus, red light is not scattered as strongly as blue light. For this reason, starlight, passing through dust clouds, becomes reddened as the blue is removed. This effect, called *interstellar reddening*, causes stars to appear redder than their effective colour.

Even the weak linear polarization of starlight is a proof of the existence of dust grains in the ISM. This necessarily implies that cannot be spherical, as often assumed in modelling. Grains are elongate particles, modeled as asymmetric spheroids made of paramagnetic material and therefore partially aligned by interstellar magnetic field.

The analyses of the infrared absorption features (for example those acquired by the satellite ISO) indicate that interstellar dust grains are mainly composed of silicates or carbonaceous material. The adsorption features observed at 10 μm and 12 μm are due to the vibrational transitions in silicates (SiO and SiO_2) and water ice. On the contrary, the interstellar extinction on the ultraviolet window can be explained by small graphite grains.

Information about the composition of cosmic dust can be worked out also from considerations of the so-called *elemental depletions*. In fact, while some species, such as N and S, have gas phase abundances (relative to H) which are approximately solar, certain others (such as Mg, Al, Si, Ti, Ca, Fe, Ni, Cr) show abundances which are far below solar. Since we presume that the interstellar abundances are approximately solar (*Sofia & Meyer*, 2001), the atoms missing from the gas must be locked up in dust grain (*Snow & Witt*, 1996). Therefore, the observed elemental depletions provide a clue to the composition of interstellar dust (Fig.1.2.2). Interstellar dust grains are presumably ejected from hot stars: in fact, the densities in the interstellar clouds are too low for the grains to be formed directly where they are

---

then geometric optics can be applied and the extinction is roughly constant. If $r \ll \lambda$, the extinction is very small. If r is comparable to λ, the diffraction effects in the scattering process are important. Hence, the wavelength dependence of the extinction is very important when $r \cong \lambda$. Comparing observation with theoretical calculation, we find that interstellar grain are not all the same size: the visible extinction is due to grains with a typical size of 0.2 μm. The ultraviolet extinction, on the other hands, reflects the presence of grains with sizes in the range 5-20 nm, and the size distribution is believed to follow a power law of the radius with exponent -3.5 (*Mathis*, 1996).

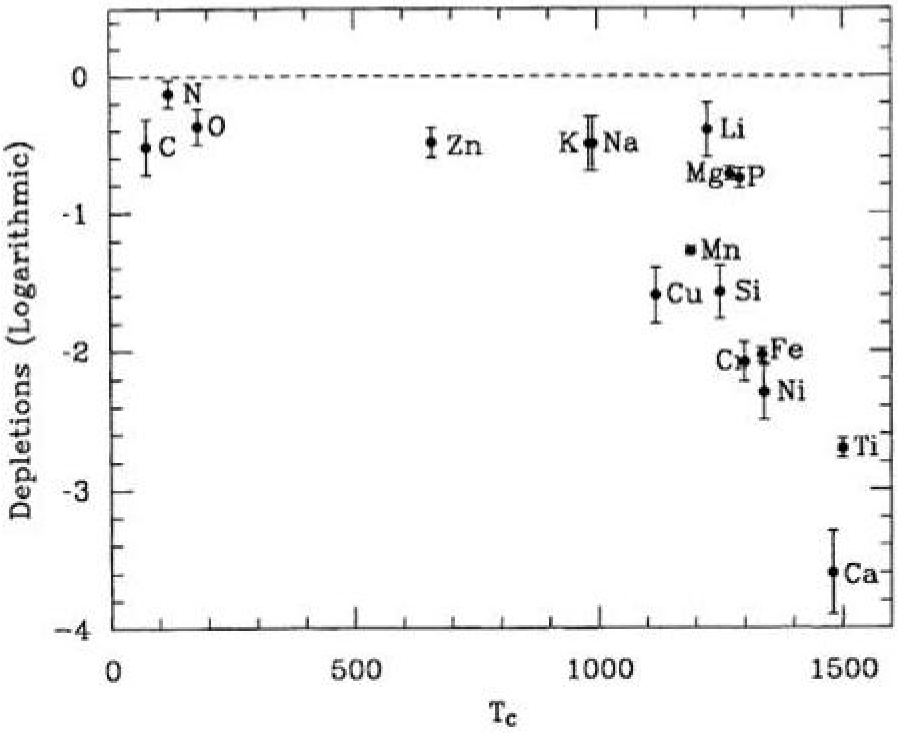

Figure 1.2.2: Elemental depletion (i.e. the difference: *log* (abundance measured) - *log* (abundance cosmic)) in the molecular cloud ζ Oph is plotted as a function of the condensation temperature of elements. Elements with $T_c \geq 1200\ K$ are able to form "refractory" solid. For instance, look at the depletion of Ca: *log* D $\sim$ -4 $\rightarrow 10^4$ times less than solar abundance

observed. Thus, towards the end of their lives, stars on asymptotic giant branch of the *H-R diagram* (**AGB** stars) are known to eject much of their envelope into space. So, these stars are surrounded by rather extended atmospheres, that are cool and dense enough to facilitate the nucleation of atoms and molecules, forming small solid particles. Stellar outflows can be carbon reach or oxygen rich: the two types determine the nature of the dust that is produced. Where carbon is more abundant than oxygen, oxygen is almost entirely locked up in carbon monoxide, and the excess carbon produces a rich chemistry of carbon-based molecules and carbonaceous dust. On the other hand, where oxygen in an envelope is more abundant than carbon, the excess of oxygen makes metallic oxide that nucleate to form solid oxide and silicates (*Williams & Herbst*, 2002).

1.2.3 Interstellar ices

In cold and dense clouds (that are interstellar regions well shielded from the far ultra-violet radiation) spectroscopy studies have shown the existence of ice mantles on the grain surfaces (e.g. *Pontoppidan et al.*, 2004). Interstellar ices are mainly formed of water, unambiguously identified by bending mode of amorphous H_2O ice (6.0 μm) and by the O-H stretching mode in H_2O ice (3.1 μm). However, interstellar water ice is mixed with several other species such as CO, CO_2, CH_3OH, CH_4, NH_3, OCS, etc (look at Table 1.1 and Fig. 1.2.3). In part, these molecules freeze out onto the grains from the gas phase; however, mantle composition doesn't reflect gas phase composition or abundances. For instance, despite numerous searches, CO_2 has not yet been observed in gas phase, while it is widely detected as an ice condensed onto dust surfaces (*Boonman et al.*, 2000).

Hence, new molecules are formed when reactive gaseous species condense on the grain surfaces or when ices are energetically processed by UV radiation and cosmic rays; several laboratory investigations support this interpretation too. Indeed, it is generally accepted that also water ice forms because of surface reactions on grain mantle at low temperature. On the contrary, direct accretion of most complex gas phase species play a very minor role in determining interstellar ice composition.

Actually, ice composition in molecular clouds depends on the local conditions (Fig.1.3.1); being hydrogen largely the most abundant element in the Universe, overall grain surface chemistry is moderated by the H/H_2 ratio.

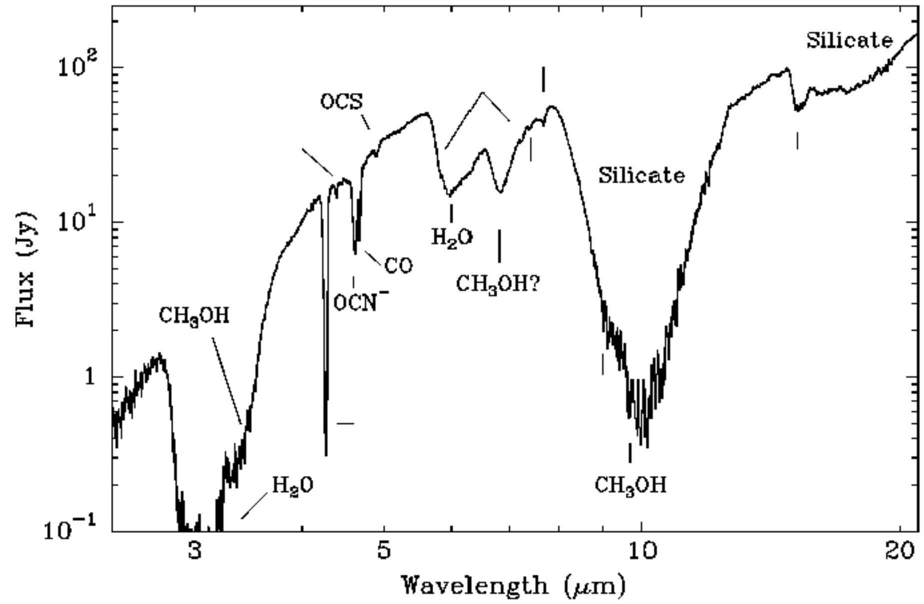

Figure 1.2.3: This spectrum (*Gibb et al.*, 2000) is an inventory of interstellar ices toward the embedded protostar W33A. It shows the absorption features both due to the dust grains (silicate bands) and due to the "dirty" ice mantles.

Molecule	**Abundance(%)**	**Molecule**	**Abundance(%)**
H_2O	100	CO	3-50
CO_2	7-25	NH_3	< 10
CH_3OH	2-25	CH_4	0.9-1.9
H_2CO	3-7	OCS	0.1
C_2H_6	≤ 0.4	OCN^-	≤ 1.9
NH_4^+	3-17	$HCOOH$	≤ 1.7

Table 1.1: Molecules detected in interstellar ices towards protostars. Molecular abundances are relative to the water ice (*Van Broekhuizen*, PhD thesis)

In regions where this ratio is large, H atom addition dominates and species as H_2O, NH_3 and CH_4 are expected to be prominent. If the H/H_2 ratio is less than 1, reactive species such as O and N are free to interact with one another, forming molecules such as CO, CO_2, O_2 and N_2. Thus, at least two qualitatively different types of ice mantles are expected to be produced by grain surface reactions, one dominated by polar H-bounded molecules and the other dominates by non-polar (or only slightly polar) highly unsaturated molecules (*Tielens et al.*, 1991). By way of an example, analyzing the profile of solid CO band coming from young stellar objects, it is possible to recognize the two kinds of ice mixture (polar and non-polar one) and in addition a third kind, which nature is still uncertain. In fact, CO stretching profile (2140 cm^{-1}) can be thought as superposition of 3 components, each one describing a different icy mixture. Thus, according to the physical condition of each cloud, it can be prevalent one of this component (*Pontoppidan et al.*, 2003).

Even though water is the main constituent in interstellar ice mantles, its chemical origin is not well understood. Some theoretical works (e.g. *Tielens*

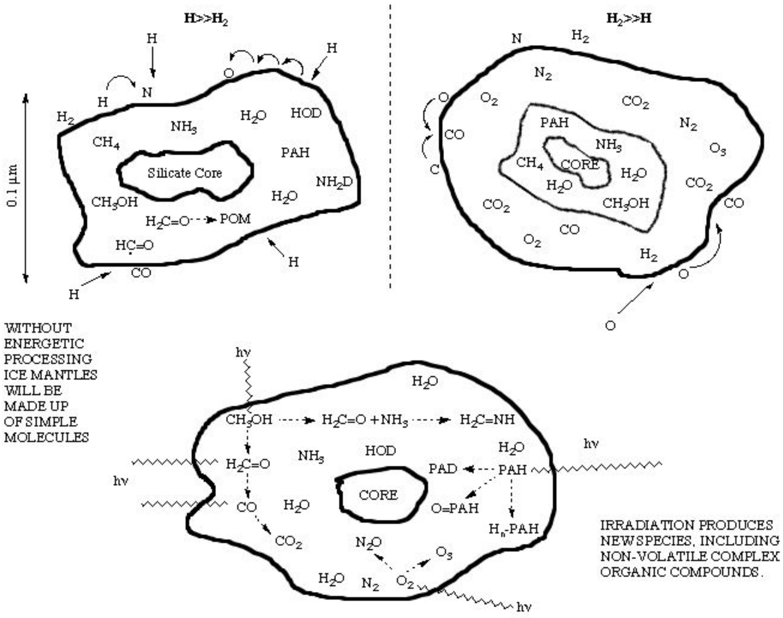

Figure 1.2.4: Schematic representation of the different types of ices mantles and their components. The interstellar ice composition in dark clouds depends on the local condition, as the ratio H_2/H or the cosmic ray and the radiation field.

& Hagen, 1982 ; *Cuppen & Herbst*, 2007) have suggested three main possible pathways for water formation: hydrogenation of O, O_2 and O_3. However, up to the time, the lack of realistic experimental simulations has not allowed to clarify the real contribution of each pathway. In the last years, many steps forward have been taken about this subject. Thus, now it is widely accepted that water molecule formation in the gas phase and the following direct accretion on the grain is not efficient enough to reproduce the observed H_2O ice abundances (e.g. *Ceccarelli et al.*, 2007). In 2006, some experiments performed through the set-up FORMOLISM have allowed to study the formation of water molecules by exposing a water ice substrate to D and O atoms and O_2 molecules, thus simulating water formation in dense interstellar clouds (*Dulieu et al.*, in preparation). During these experiments, it has been shown that D_2 molecules do not react with O atoms nor with O_2 molecules residing on the ASW ice surface. Therefore, the water formation process requires hydrogen in atomic form.

Very recently, the $H + O_2$ pathway has been analysed using IR spectroscopy in situ, by different groups dealing with Astrochemistry. All the experiments (performed in condition roughly similar to the interstellar one) show that the formation route that converts O_2 into H_2O via H_2O_2 is more efficient than previously assumed by theoretical study (*Miyauchi et al.*, 2008; *Ioppolo et al.*, 2008). Moreover, it has been confirmed that the hydrogenation of the molecular oxygen produces amorphous water, with a compact (or non-porous) structure (*Oba et al.*, 2009).

Interstellar water ice is believed to be mainly amorphous, that is to say without a distinct crystalline structure. This has been shown both observationally (*Smith et al.*, 1989) and theoretically (*Kouchi et al.*, 1994). So, while there is quite a general consensus that interstellar water ice is mainly amorphous, its morphology still remains poorly known, although this parameter has a great importance for interstellar gas-grain reactions. Indeed, laboratory simulations have demonstrated that ice porosity influences greatly both the efficiency of H_2 formation (*Roser et al.*, 2002) and the energy contents of H_2 as it is released from the grain on the ISM just upon its formation (*Hornekær et al.*, 2003). Moreover, it has been observed (*Ayotte et al.*, 2001) that a porous ice film is able to adsorb between 20 and 50 times more gas than a compact one.

Identification of ice porosity can be based on weak infrared absorption features ($\sim 2.7\ \mu m$) due to the $O-H$ vibration of dangling bonds on the pore surface (*Rowland et al.*, 1991). But, according our knowledge, to date there have been no detection of dangling bond adsorptions in the infrared spectra of interstellar ices, perhaps suggesting that they have a compact nature (*Keane et al.*, 2001). So, it is possible that, after surface reactions only compact amorphous water ice forms on interstellar grains. Otherwise, in conformity with the results of several laboratory simulations, interstellar porous ice could be compacted by transient heating or stellar radiation or cosmic rays or by some other process.

The work in the present thesis takes place in this picture. Chapter 4, it is shown experimentally the gradual compaction of the porous interstellar ice analogues following atomic hydrogen exposure; whereas, Chapter 5 emphasizes that the water ice formed through the pathway $D + O_2$ has a non-porous structure.

1.3 Interstellar clouds

Although it is difficult to classify rigorously the complexity of the interstellar medium, it is possible to identify five broad kinds of interstellar environments according to temperature, phase and density of the hydrogen (see Table 1.2). The physical characteristics of each interstellar cloud depend on the balance between the different heating and cooling mechanisms.

For the subject discussed in the present thesis, denser and cooler interstellar regions are indisputably the more interesting, because only in these regions dust grains are covered by ice. However, for the sake of completeness, a brief description of the other important interstellar environments is given hereafter.

A large fraction of the volume of the Milky Way ($\sim$ 50 %) is filled with a tenuous ($\sim 10^{-3}\ cm^{-3}$), ionized and very hot gas (T $\sim 10^5 - 10^6$ K), known as **coronal gas**, because comparable to that of the solar corona. This hot gas can be traced through UV absorption lines of highly ionized species (e.g. $C\ IV$, $S\ VI$, $O\ VI$) observed against bright background sources. Moreover, such hot plasmas emit continuum (such as bremsstrahlung and radiative recombination) and line radiation in the extreme ultraviolet and X-ray wavelenght regions. Supernovae explosions and early type stars generate the

Figure 1.3.1: The *Horse Head Nebula* is part of Orion molecular cloud. The nebula is formed by the dust blocking the light from the glowing gas in the background. The fuzzy blue patch at lower left of the Horsehead is a reflection nebula, where dust is scattering light from a hidden background star towards us.

ISM component	**Common designations**	**T(K)**	**Density (cm^{-3})**	**State of Hydrogen**
Hot ionized medium (HIM)	Coronal gas	10^6	0.003	H^+
Warm Ionized Medium (WIM)	H II regions	10^4	> 10	H^+
Warm Neutral Medium (WNM)	Interclouds regions	10^3 - 10^4	0.1	H^0
Cold Neutral Medium (CNM)	Diffuse clouds	100	10 - 100	$H^0 + H_2$
Molecular cold medium (CNM)	Molecular Clouds	10 - 50	10^3 - 10^5	H_2
	Dense Clouds			
	Dark Clouds			

Table 1.2: Classification of interstellar clouds. This table is compiled according to the information got in *Wooden et al.,* 2004.

coronal gas when their energetic winds collide with and shock the surrounding medium. Dust grains in such gas are rapidly destroyed by sputtering.

Ionized gas nebulae (or *H II* **regions**) are often detected either as bright visible nebulous objects or through optical and UV ionic absorption lines against background sources, or through the emission in the $H\ \alpha$ recombination line. These regions have a low density ($\sim 0.1\ cm^{-3}$) and relatively high temperatures ($\sim 10^4$ K). The source of ionization is not entirely clear. It seems that these regions are formed by young massive stars with spectral type earlier than B1. These stars emit copious amount of energetic photons ($E = h\nu > 13.6\ eV$) able to ionise and heat the surrounding clouds of gas. In *H II* regions, dust tends to be eroded.

As already discussed, the 21 cm line due to the atomic hydrogen traces the neutral gas of the ISM. This neutral gas can also be observed in optical and UV absorption lines of various element towards bright background stars. The neutral medium is organized in cold ($\sim 80-100$ K) diffuse *H I* clouds (**CNM**, cold neutral medium) and warm ($\sim$ 8000 K) interclouds gas (**WNM**, warm neutral medium). A standard *H I* cloud has a typical density of 50 cm^{-3} and a size of 10 pc. Interclouds (or WNM) regions have lower density ($\sim 0.5\ cm^{-3}$); they occupy $\sim$ 30% of the volume of the ISM, and are located mainly in photodissociation regions, on the boundaries of HII regions or molecular clouds.

Diffuse clouds are characterized by a low number density; so, UV and visible light from stars can penetrate them and ionise most of the elements, except for the case of hydrogen, which is roughly equally divided into neutral atoms and molecules. In these regions, the coexistence of gas and dust is verified: the hydrogen column density shows a correlation with the visual extinction. Furthermore, the high H_2 abundance detected in diffuse clouds concurrently with photo-dissociation entails the presence of an active grain-surface chemistry. The detection of more complex molecules is a further evidence that gas and dust are well mixed.

Molecular clouds are dense enough that they are opaque to starlight. They comprise $\sim 30\%$ of the mass of ISM, but occupy only ~ 0.05 % of its volume. Although a small but detectable amount of the atomic hydrogen remains (*Li & Goldsmith*, 2003), the hydrogen is mainly molecular, thereby remaining for the majority invisible to direct study. Therefore, the transition at 2.6 mm due to the carbon monoxide is commonly used as a tracer of molecular gas, even though H_2 is always the dominant molecular species, with a H_2/CO ratio of $10^4 - 10^5$. In molecular clouds, the material is shielded so well from the ultraviolet radiation fields than complex molecules can form and dust grains can be covered by thin icy mantles whose composition does not reflect that in the gas phase, thereby stressing a rich grain surface chemistry. In fact, to date more than 150 different molecular species have been detected (mainly through their rotational transitions in the submillimeter wavelength regions) in the shielded environments of molecular clouds. A list of the molecules detected till now is shown in Fig.1.3.2. It is widely recognized the role of the molecules as crucial in the thermal balance of gas in astrophysical objects. In fact, in the Universe, molecules act as natural temperature regulators. They can cool gas to low temperatures and, thereby, allow gravity to overcome thermal forces and clouds to collapse to form new stars and planets. Because of its predominance, molecular hydrogen is turned out to be the most important coolant: this molecule is, in fact, able to extract kinetic energy from the gas and lose it via radiative emission. For the mentioned reasons, in a friendly way, molecular clouds are also called *stellar nurseries*.

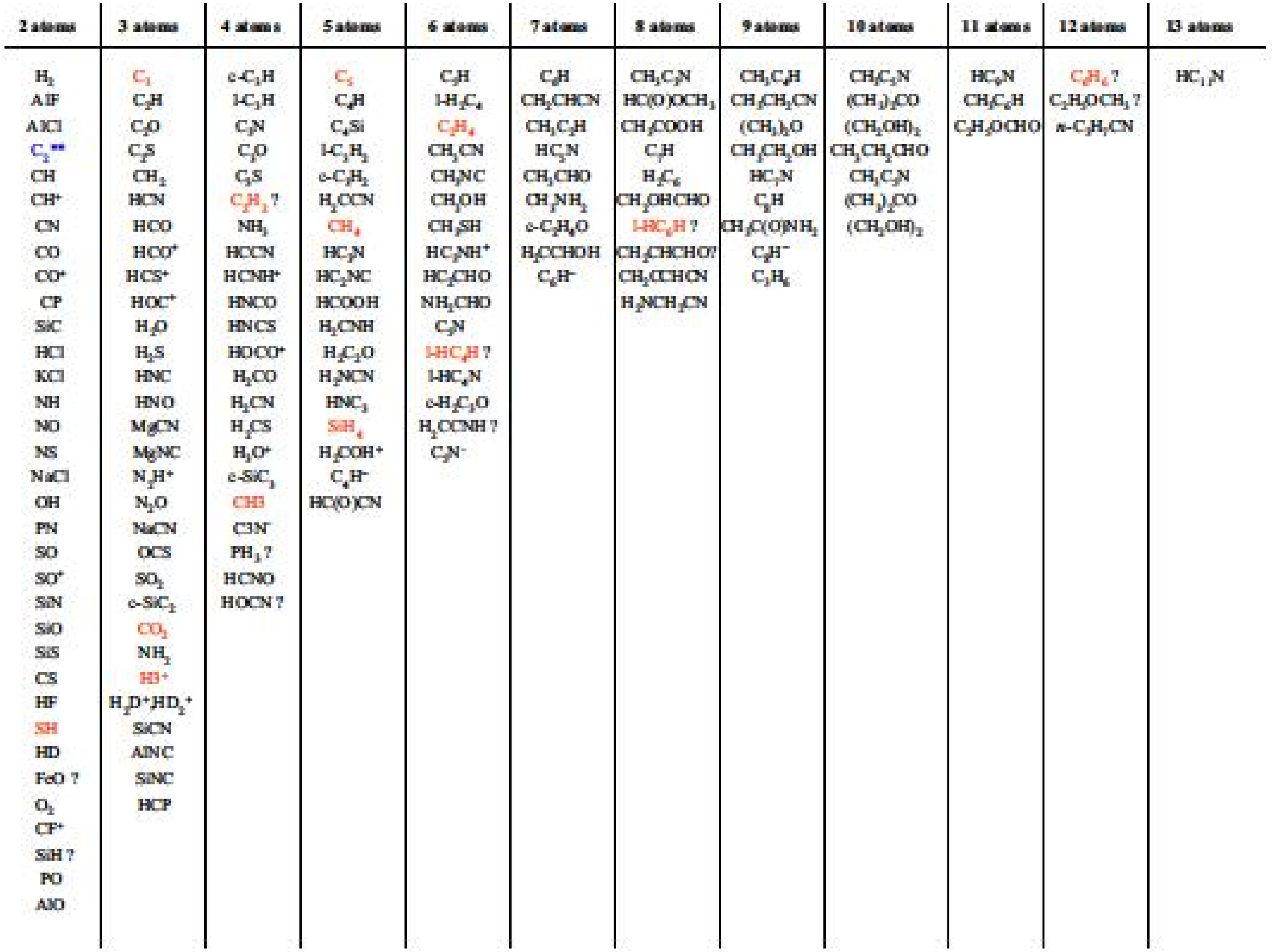

2 atoms	3 atoms	4 atoms	5 atoms	6 atoms	7 atoms	8 atoms	9 atoms	10 atoms	11 atoms	12 atoms	13 atoms
H_2	C_3	c-C_3H	C_5	C_5H	C_6H	CH_3C_3N	CH_3C_4H	CH_3C_5N	HC_9N	C_6H_6 ?	$HC_{11}N$
AlF	C_2H	l-C_3H	C_4H	l-H_2C_4	CH_2CHCN	$HC(O)OCH_3$	CH_3CH_2CN	$(CH_3)_2CO$	CH_3C_6H	$C_2H_5OCH_3$?	
AlCl	C_2O	C_3N	C_4Si	C_2H_4	CH_3C_2H	CH_3COOH	$(CH_3)_2O$	$(CH_2OH)_2$	C_2H_5OCHO	n-C_3H_7CN	
C_2**	C_2S	C_3O	l-C_3H_2	CH_3CN	HC_5N	C_7H	CH_3CH_2OH	CH_3CH_2CHO			
CH	CH_2	C_3S	c-C_3H_2	CH_3NC	CH_3CHO	H_2C_6	HC_7N	CH_3C_5N			
CH^+	HCN	C_2H_2 ?	H_2CCN	CH_3OH	CH_3NH_2	CH_2OHCHO	C_8H	$(CH_3)_2CO$			
CN	HCO	NH_3	CH_4	CH_3SH	c-C_2H_4O	l-HC_6H ?	$CH_3C(O)NH_2$	$(CH_2OH)_2$			
CO	HCO^+	HCCN	HC_3N	HC_3NH^+	H_2CCHOH	CH_2CHCHO?	C_8H^-				
CO^+	HCS^+	$HCNH^+$	HC_2NC	HC_2CHO	C_6H^-	CH_2CCHCN	C_3H_6				
CP	HOC^+	HNCO	HCOOH	NH_2CHO		H_2NCH_2CN					
SiC	H_2O	HNCS	H_2CNH	C_5N							
HCl	H_2S	$HOCO^+$	H_2C_2O	l-HC_4H ?							
KCl	HNC	H_2CO	H_2NCN	l-HC_4N							
NH	HNO	H_2CN	HNC_3	c-H_2C_3O							
NO	MgCN	H_2CS	SiH_4	H_2CCNH ?							
NS	MgNC	H_3O^+	H_2COH^+	C_5N^-							
NaCl	N_2H^+	c-SiC_3	C_4H^-								
OH	N_2O	CH3	HC(O)CN								
PN	NaCN	$C3N^-$									
SO	OCS	PH_3 ?									
SO^+	SO_2	HCNO									
SiN	c-SiC_2	HOCN ?									
SiO	CO_2										
SiS	NH_2										
CS	$H3^+$										
HF	H_2D^+,HD_2^+										
SH	SiCN										
HD	AlNC										
FeO ?	SiNC										
O_2	HCP										
CF^+											
SiH ?											
PO											
AlO											

Figure 1.3.2: List of the interstellar and circumstellar molecules observed until the beginning of 2009. In red are molecules that have been detected by their ro-vibration spectrum, (*) denotes those that have been detected by electronic spectroscopy and (?) denotes tentative detections that have a reasonable chance to be correct but remain uncertain (*http://www.astro.uni-koeln.de/cdms/molecules.*).

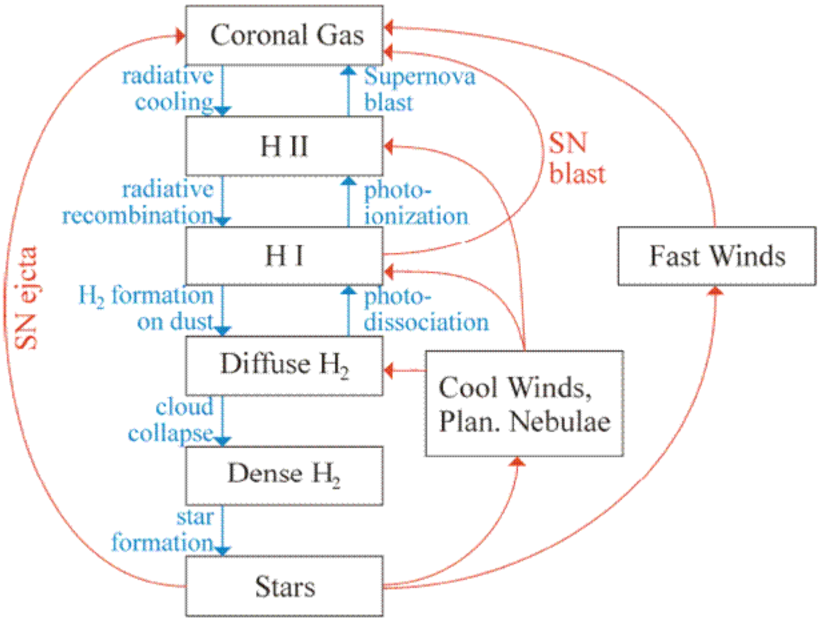

Figure 1.3.3: Scheme of life cycle of the interstellar clouds.

1.4 The lifecycle of the Galaxy

There is a complex link between star formation and the interstellar medium. The interaction between stars and ISM determines the structure, composition, chemical evolution and observational characteristics of the interstellar medium in the Milk Way.
The cold clouds characterized by molecular hydrogen are the birthplace of new stars when they become gravitationally unstable and collapse. Depending on the mass, the formation of the star can follow different routes producing: Sun-like mass, high-mass or giant-mass star (Fig. 1.4.1). For every routes, each step of the star formation process is characterised by different chemical species, which can be the "signatures" of each of these steps.

All the stars, ejecting gas and dust into the ISM through their wind, influence the interstellar chemistry and thereby the star formation rate. Actually, winds from low-mass stars control the total mass balance of interstellar gas and contribute substantially to the injection of dust and polycyclic aromatic

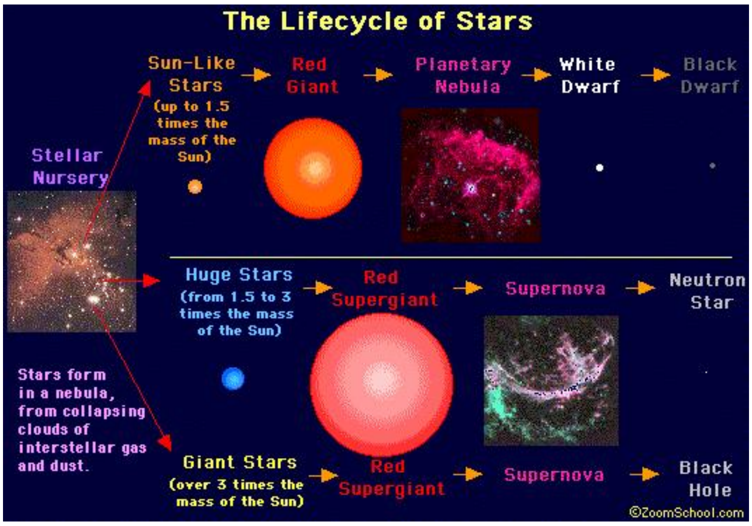

Figure 1.4.1: According to the initial mass of the collapsing object, star's evolution can follow three different routes.

hydrocarbon molecules (PAHs), that are important heating agents in the interstellar gas because likely act as electron donors in the photoelectric effect induced by UV absorption. On the other side, massive stars regulate the ultra-violet photon energy budget and the cosmic-ray flux, which are important heating, ionization and dissociation sources of the interstellar gas. They are also the source of intermediate-mass elements that play an important role in the interstellar dust.

Because of all these interactions, it is worth stressing that the complexity of the ISM is also due to the fact that this environment is far from being in thermodynamic equilibrium. In fact, in thermodynamic equilibrium, matter is characterized by a single temperature, which describes the velocity distribution, excitation, ionization and molecular composition of the gas. The velocity distribution of the interstellar gas can generally be well described by a single temperature, but excitation, ionization and molecular composition are often very different from thermodynamic equilibrium values at this temperature.

Chapter 2

The experimental apparatus: FORMOLISM

All the experiments described in this thesis are performed in the astrophysical laboratory in Cergy-Pointoise University (France). The apparatus is called **FORMOLISM**, i.e. **FOR**mation of **MOL**ecules in the **ISM**, and it is dedicated for investigation of physical-chemical reactions on surfaces of astrophysical interest, in condition roughly similar to the interstellar one, namely low temperature and low density.

I spent about half of my Italian doctorate in that university. Thanks to the availability, the patience and the competence of the scientific team of FORMOLISM, in a short time I became self-confident with the complex experimental device. Actually, I was personally able to carry out all the experiments that will be reported in next chapters.
The present chapter describes in detail the laboratory equipment, focusing in particular on the experimental devices used during my experiments.

2.1 Overview of experimental apparatus

A schematic drawing of FORMOLISM (the experimental equipment in Cergy-Pointoise University) is shown in the Fig.2.1.1. Following the numbers in the figure, the apparatus consists of:

1. An ultra high vacuum (UHV) chamber, i.e. the main chamber;
2. A quadrupole mass spectrometer (QMS);
3. A sample holder connected to a cryostat;
4. Two triple differentially pumped atomic/molecular beam lines.

Each part will be described in detail in the next sections.

2.2 The main chamber

The main chamber consists of a stainless steel cylinder, with radius equal to 15 cm and height equal to 120 cm. So, its volume is $\sim$ 85 litres, and it is mainly evacuated by a turbo molecular pump (with pumping speed $\sim$ 1000 l/s), but also by an ion pump and a titanium sublimation pump. In this way, the residual pressure inside the chamber (mainly due to molecular hydrogen and water vapour) can reach values lower than 10^{-10} $mbar$, corresponding to a molecular/atomic density of 2×10^{6} cm^{-3}. Actually, this density is still rather high compared to the interstellar one: in a dark cloud, density is estimated to be $\sim 10^{4}$ cm^{-3} (*Williams & Herbst*, 2002). However, to date it is technically impossible to get better vacuum in terrestrial laboratories. There is, in fact, a continuous desorption of species (H_2 and H_2O, mainly) coming from the different portions of the apparatus, especially from the walls of the vacuum chamber. In order to minimize this effect, the chamber is periodically warmed up to 100 °C for a few days (*baking procedure*). In this way, the rate of degassing is drastically cut down when the room temperature is established again into the chamber. Further details about this *baking procedure* can be found in next Section.

Anyway, residual pressures into the main chamber are low enough to make not very important the pollution level on the surface of the solid sample: indeed, it is easy to evaluate that, at a pressure of 10^{-10} $mbar$ and a surface

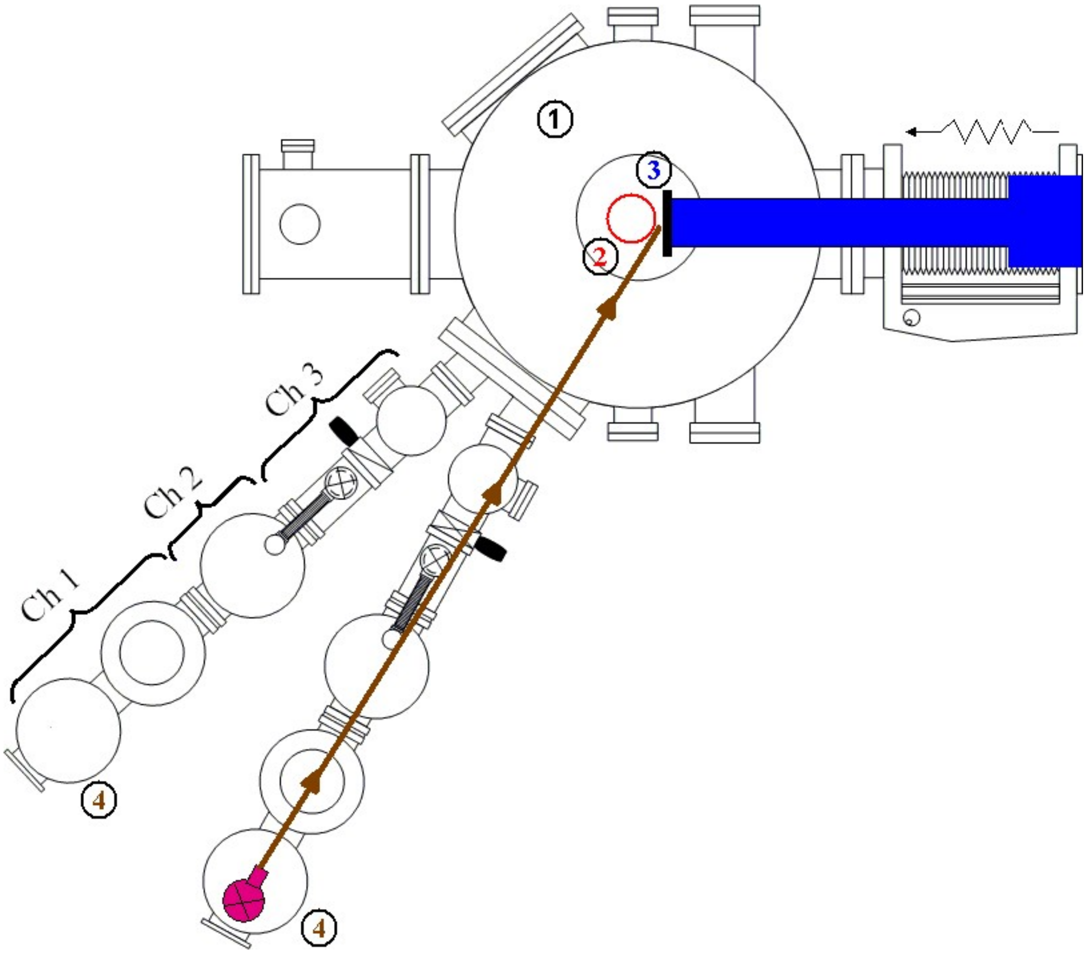

Figure 2.1.1: Scheme of FORMOLISM (top view), the laboratory equipment dedicated to the study of solid state for Astrophysics, in Cergy-Pontoise University.

temperature of 10 K, the sample-holder is coated with ~1 ML of water vapour only after ~ 5000 minutes.

Althoug not shown in Fig.2.1.1, the chamber houses a leak valve equipped with a microchannel doser. Once the leak valve is opened, water vapour diffuses into the chamber via a micro capillary array. The controlled dosing of the water vapour allows to grow interstellar ice analogues on the previously cooled surface. Two different experimental methods are used depending on the kind of ice we want to grow. Both methods will be carefully described in Section 3.1.

In the experiments discussed in this thesis, the porous ice films (few layers of H_2O as thickness) are grown on the top of a quite thick (~100 ML) compact ice layer. In this way, our samples are completely isolated from the Cu sample-holder surface, avoiding, thus, complication in the TPD spectra arising from the interaction of the gas with the underlying hydrophilic substrate.

2.2.1 Baking procedure

A continuous desorption of species (H_2 and H_2O, especially) coming from the walls of the chamber affects the quality of the vacuum into the chamber. Of course, this desorption is compensated by continuous pumping; the combination of desorption and pumping gives the limiting pressure value.

The rate of degassing from the walls can be drastically cut down through the so called *baking procedure.* This operation is performed whenever the residual pressure in the chamber at room temperature is higher than 10^{-9} *mbar*, for example after each opening of the experimental set-up.

Actually, the *baking procedure* consists on heating up to ~100°C the main chamber for few days. In this way, the rate of desorption is temporarily increased and a large amount of the adsorbed species is removed from the walls of the chamber. Thus, when cooling down back to room temperature, the rate of degassing is cut down, and consequently the base pressure is lowered.

During my long stay in the research team of FORMOLISM, we were obliged to open the apparatus many times because of the failures in the mass spectrometer and the appearance of micrometric leaks in the chamber. For this reason, baking procedure was repeated many times.

Before the heating phase, the apparatus must be coiled with proper electric-heating wires and then covered with isolating aluminium foils that help to maintain and homogenize the temperature of the walls. A homemade Labview procedure drives the heating phase, allowing the regulation and the control of the heating rate; in this way, the most fragile parts of the set-up (like the windows) are safeguarded from excessive heating.

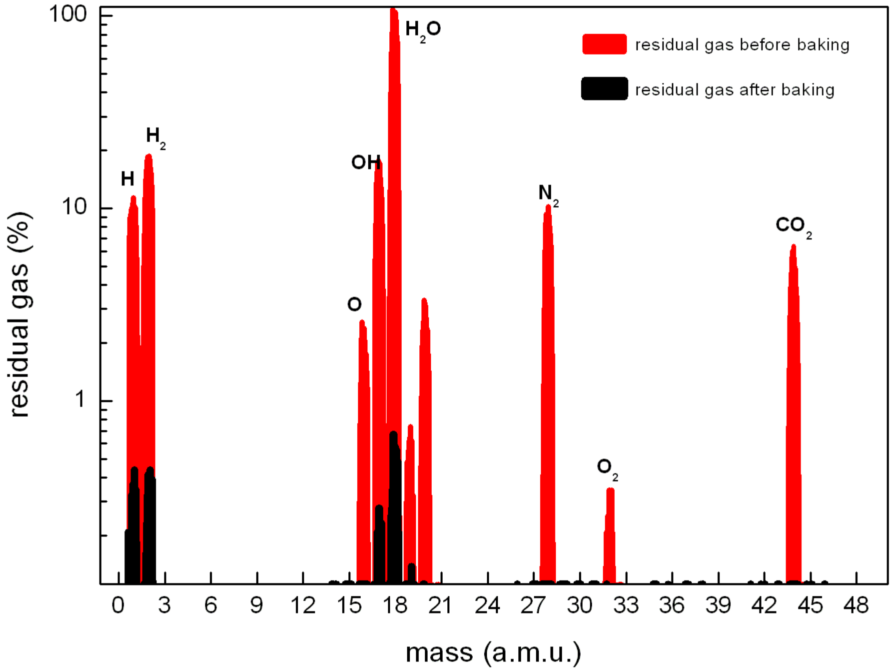

Figure 2.2.1: Residual gases detected by the mass spectrometer in the UHV chamber before (red) and after (black) a baking procedure. The different species are normalised respect to water vapor (100%) detected before the baking.

Fig.2.2.1 illustrates the importance of the baking procedure, showing the different abundances of the various species forming the residual gas in the main chamber before and after the baking. In the figure, signals detected by the QMS for every mass have been normalized to that of H_2O detected before heating of the set-up. After baking, nitrogen has almost completely disappeared, while the amount of water vapour is reduced by a factor of 100.

2.3 The sample holder

The sample holder consists of an high conductivity copper circular cylinder, with radius equal to 5 mm. It lies in the main chamber, at the same height of the beam lines, and is connected with the so-called "800 K interface". A very thin silver foil insures a good thermal conductivity between these two elements. Finally, the "800 K interface" is mounted on the second stage of the cryocooler (Fig.2.3.1).

The "800 K interface" (sold by *ARSCRYO*) contains an internal thermal switch which protects the cold end of the cryostat from excessive and potentially harmful heat while experiments are carried out at elevated temperatures. In particular, the switch is automatically open when the temperature of the sample holder becomes higher than 350 K: in this way, the heat transfer to the coldest end of the cryostat results unimportant. Moreover, "800 K interface" having an electric resistance, is able to heat the sample holder until 800 K. Therefore, our sample holder can withstand a range of potential temperatures between 8 and 800 K.

The cryostat connected to the "800 K interface" is a two stage cryocooler that operates on the principle of the *Gifford-McMahon refrigerator cycle* [1]. Although the temperature at the bottom of the second stage is 4.2 K, the lowest temperatures reached by the sample are never lower than 8 K because of the natural thermic losses.

The whole set is mounted on a translation plate, that allows us to move back and forth the sample holder with respect to the centre of the chamber in order to allow a better positioning of the QMS or the water vaporizer.

As shown in Fig.2.3.1, a thermic buckler - made of a mixture of copper and nickel - is screwed at the base of cryostat. It protects and isolates the sample holder, the "800 K interface" and the second stage of the cryostat from IR radiation (the thermal one) coming largely from the wall of the chamber. In this way, it is possible to keep rather stable the temperature of

---

[1] Although out of the aims of this thesis, it is worth spending some words about the Gifford-McMahon cycle. Actually, Gifford-McMahon (GM, briefly) refrigerators are the largest application of cryocoolers. A GM cooler is a variation of a Stirling one, because the physical principle is the same. Helium is used as working fluid because of its ideal gas properties and its high thermal conductivity. In practice, the coordinated motion of a piston and a displacer allows the realization of the GM cycle: the thermal cycle consists in a (quasi) isothermal compression and in a (quasi) isothermal expansion of the He gas, besides two isometric transformation.

the sample holder, minimizing the heating effect due to the IR irradiation.
Fig.2.3.1 shows also the position of the three different types of sensors that measure the temperature. Thus, there is a KP-type thermocouple (*Au-Fe*/Chromel), a K-type thermocouple (Nickel-Chromium/Nickel-aluminium) and a Silicone diode.
The thermometers and the electric resistance in "800 K interface" are connected to a controller (*Lakeshore 340*), that allows the reading of the different temperatures and the regulation of the sample temperature, just by varing the power of the heating resistance.
A homemade software code (using *Labview*) enables us to check and control the sample temperature by a computer. That is very important because *Labview* is able to control accurately the heating power setting in order to get a linear increase of the sample temperature during a TPD experiment. Moreover *Labview* allows also to monitor and to record the trend of the different temperatures measured by every thermometer as function of the elapsed time.

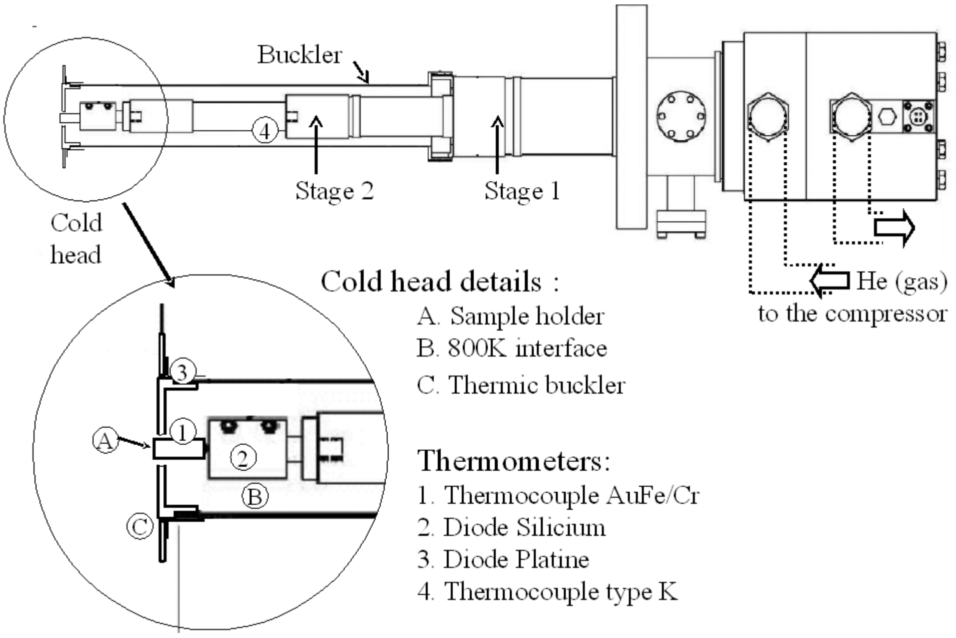

Figure 2.3.1: Scheme of the cryostat, with longitudinal section of the farthest part.

2.4 The water vapour diffuser

The water diffuser in the main chamber can be easily moved and placed in two main positions (in front of or above the sample holder) depending on the kind of water ice we would like to grow (see Paragraph 3.1 for further details).
A small glass vial ($\sim 100\ cm^3$) containing liquid water [2] is connected with the UHV chamber via a low rate leak valve. The small vial is also connected to a turbo pump and a pressure gauge. In this way, we are able to read and to controll the saturating water vapour pressure behind the leak valve, before its opening. Generally its value is fixed $\sim 20\ mbar$.
Once the leak valve is opened, water vapour diffuses into the chamber via a micro capillary array diffuser at the end of $\sim 30\ cm$ stainless steel tube: this rather long pipeline ensures the uniformity of water vapour flux. The micro-capillary system presents a round surface ($\sim 1\ cm$ in diameter) composed of hundred channels with an aperture of $\sim 45°$.

2.5 The quadrupole mass spectrometer

A movable quadrupole mass spectrometer (QMS) is mounted in the upper part of the main chamber: at the moment, it represents the main analysis instrument in this laboratory [3].
The QMS (an *HIDEN model*) is able to analyze the composition and the abundances of the residual gas into the main chamber or to characterize the atomic/molecular jet coming from the beam lines or to check the desorbed species from the sample during a TPD experiment.
The QMS can be translated vertically and rotated. In the upper position, it serves to analyse the gases present in the chamber, while in the lower position it can either face one of the beams to characterize them and to measure the dissociation rate or face the sample surface to measure the desorption rate.

Fig.2.5.1 shows schematically the main parts that form a QMS. The in-

---

[2] When it is necessary to fill the vial, the demineralised water undergoes a purification process. It consists in a series of solidification - fusion cycles: in this way, all the gaseous impurities dissolved in the water are released in the gas phase and can be pumped out.

[3] FORMOLISM will be soon enriched with an infrared spectrometer able to analyse the icy sample in situ

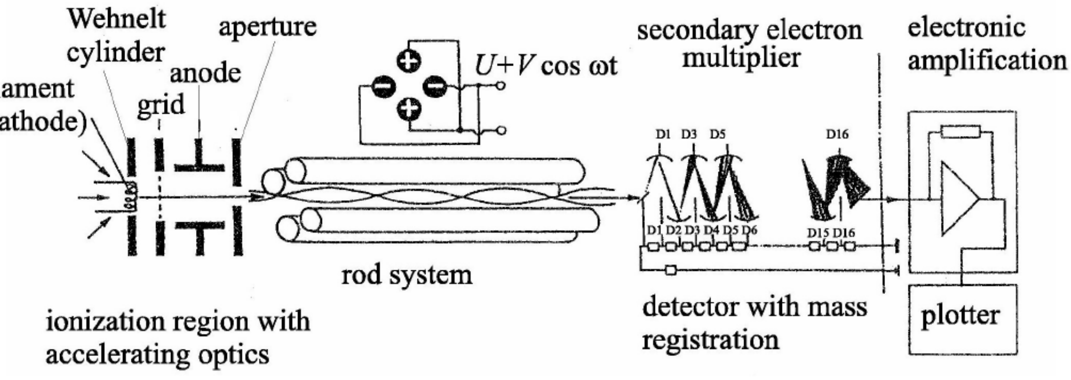

Figure 2.5.1: Schematic description of a quadrupole mass spectrometer (QMS).

strument can be divided into three parts: the ionization zone, the ion flight zone and the ion detector. So, atoms/molecules, entering the quadrupole probe, are ionized via electron bombardment by passing near to a heated tungsten filament and are subsequently accelerated towards the four straight and parallel rods (the ion flight zone). These four metallic rods represent the ion mass filter able to select species according to their mass-to charge ratio (m/z); in fact, a voltage combination of a direct and a radio frequency component is applied between adjacent and opposite rods. Once inside the quadrupole, only ions of a certain m/z will reach the detector, guided by the resonance with the oscillating voltage. The other ions will be expelled from the ion flight zone. Varying the direct and the radio frequency component, the QMS is able to scan all the ions up to a chose mass to charge ratio technically fixed (in our case 50 m/z).
The ion detector is a *Channeltron*, that is an electron multiplier able to induce a cascade of secondary electrons for each ion impact. The output current so generated in the *Channeltron* is converted into a digital signal. The digitalized signal is then controlled by a software provided by *HIDEN*. It allows to monitor and record the acquired information, but also to adjust the electronic setting of the QMS and the dwelling times between two measurement. Moreover, it is possible to record simultaneously the sample temperature measured by *Lakeshore* controller during TPD experiments.
Our detector must work with residual pressures lower than 10^{-6} $mbar$, and it is able to detect partial pressures up to 10^{-14} $mbar$.

2.6 Beam lines and microwave cavity

FORMOLISM uses the same architecture devised by *Pirronello et al.* (1997), i.e. it is equipped with two triple differentially pumped atomic/molecular beam lines that are connected with the main chamber and aimed at the surface of the sample holder (Fig.2.6.1). In this way, it is possible to expose the sample to two different species simultaneously (e.g. D/D_2 and O/O_2). Each beam line is composed of three differentially pumped stages: thus a rather low and well-collimated flux of particles can be created in the direction of the sample. The rationale is to select in the gas phase only particles with a precise trajectory, thereby enabling them to reach the sample surface with a very small solid angle ($\sim 8 \times 10^{-6}$ str). In fact, the gas beam, prior to reach the UHV chamber, must pass in the three stages (i.e. chambers pumped

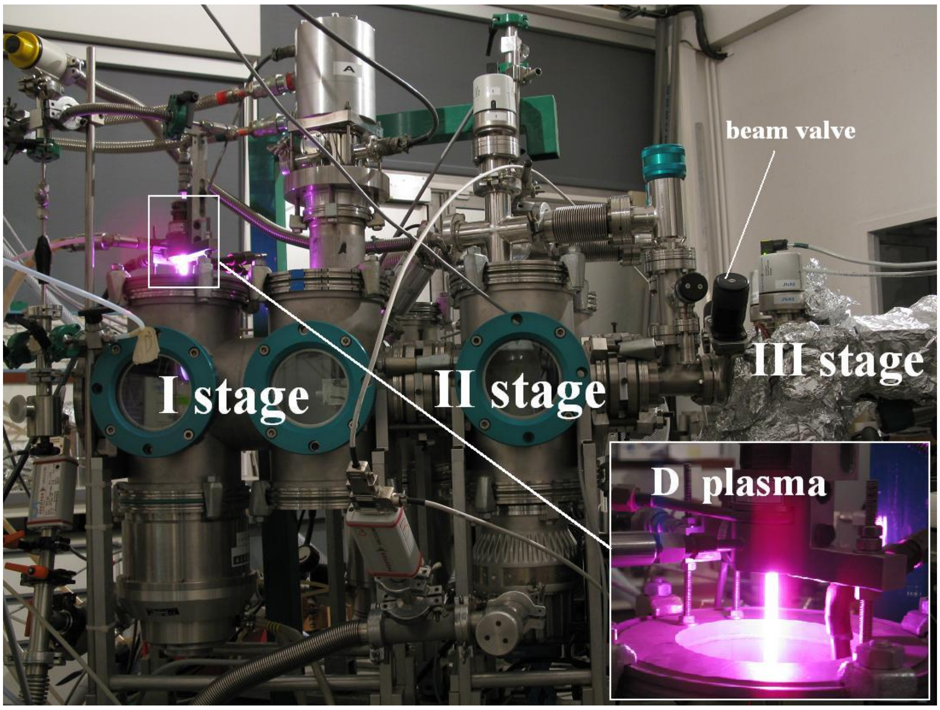

Figure 2.6.1: Photo of the three diffentially pumped beam line in FORMOLISM. As here shown, a plasma of deuterium can be created in the tube, behind the first stage.

separately) shown in Fig.2.6.1: three aligned (millimetric) diaphragms connect each stage with its adjacent. During this three steps, the gas pressure decreases gradually from 1 $mbar$ (in the initial tube) to 10^{-10} $mbar$ (in the main chamber).
In practice, the gas (molecular hydrogen, for example) is introduced into the first stage of the beam line, with a pressure of 1 $mbar$ as order of magnitude. Through a first tiny diaphragm, a small quantity of the gas passes into the second stage, where there is a lower residual pressure. Here, a second tiny diaphragm (aligned with the previous and the next one) connects to the third stage, where there is a residual pressure of $\sim 10^{-8}$ $mbar$. Between the second and the third stage there is a valve, because last stage is directly connected with the main chamber by the third diaphragm.
A small revolvable metallic plate (called "beam flag") is placed between the third stage and the main chamber. When this flag is closed, the jet of particles reaches directly the sample surface. On the contrary, when the flag is open, the jet is broken and its particles do not arrive straight to the icy sample, but they fill the main chamber: in this case, the particles will condense on the icy sample by "background" deposition.
The methods used to estimate the atomic/molecular flux will be described in the next Chapter. Anyway, its estimation is $\sim 10^{12}$ - 10^{13} $cm^{-2}s^{-1}$, namely several order of magnitude higher than the interstellar ones. Therefore, models are often necessary in order to extrapolate from laboratory data information useful for astrophysics.

The first stage of each beam line houses a microwave cavity (a Surfatron cavity delivering 300 W at 2.45 GHz) for dissociating molecular gases such as hydrogen, deuterium or oxygen. Microwaves are, in fact, able to transfer their energy to the gas, thereby exciting and ionizing the gas that is thus changed into a plasma.
In order to inhibit (or, better, to minimize) the spontaneous recombination of the atomic species on the walls of the discharge tube (a quartz one), the system is cooled by a constant jet of compressed air round the tube and by a water circuit round the metallic parts.
In particular, it is estimated that, in our apparatus, the rate of dissociation is about 70-90% for D_2 and 60-80% for H_2. These values are determined by the mass spectrometer, just comparing the molecular signal (H_2 or D_2) when the microwave discharge is switched on and when it is switched off (look at

Fig.3.3.2).

Chapter 3

Experimental procedures

This chapter is devoted to the description of all the experimental procedures used to carry out our experiments. The order of the sections that constitute the present chapter follows the logical succession of operations made during the experimental work. Therefore the methods used to grow water ice films with different porosity on the cold sample holder; the TPD technique and the method used to probe the morphology of an icy sample by studing the thermal desorption of gases adsorbed on it; the different methods used in order to calibrate the experimental beams.

3.1 Water ice films on the sample holder

It is known that in nature water ice exists in a large number of phases (amorphous, hexagonal, cubic, rhomboedric, etc.), depending on the temperature and the pressure under which it is formed (*Petrenko & Whitworth*, 2002).
Spectroscopy studies of dark clouds have emphasized that the water ices mantles grown over dust grains are mainly amorphous, namely without some crystalline structure (*Leger et al.*, 1979). Although there is quite a general consensus that interstellar water ice is mainly amorphous, its morphology (more or less porous, see Fig.3.1.2) still remains poorly known.

As the experiments described in this work are mainly aimed at the study of interstellar ice analogues, films of amorphous solid water (ASW, briefly) are grown under ultrahigh vacuum by slow deposition of water vapor over the cold sample holder.

As already studied (e.g. *Stevenson et al.*, 1999), in the laboratory ice morphology depends on two main factors as the surface temperature during deposition and the angular distribution of the water molecules incident from the gas phase. Because of the configuration of the set-up FORMOLISM, ice morphology can be settled only by the choice of the surface temperature during the deposition.

Two different methods of water ice growing are used in our set-up: either the *spray deposition* or the *background deposition*. Both of them will be described in the following two sections.

3.1.1 Spray deposition

The deposition by spraying is a direct method to grow the ASW quite fast. For this reasons, it is used to deposit large amount of water molecules, for example when we want to grow a substrate of compact ice that isolates another type of ASW film from the metallic sample holder.

During the spray deposition, the microchannel array doser is installed at 2 cm in front of the sample holder surface maintained at 120 K, as shown in Fig.3.1.1. As already described in the previous chapter, a small glass vial contained liquid water is connected with the water diffuser into UHV chamber via a low rate leak valve. When we open this leak valve, the local pressure in the region between the diffuser and the copper substrate is estimated $\sim 10^{-6}$ $mbar$, while the residual pressure into the chamber is regulated around 10^{-9} $mbar$. It has been evaluated that the mean free path of H_2O molecules is about 1 m while the residual pressure is 10^{-6} $mbar$. As the distance between diffuser and cold surface is very short compared to the mean free path, we can say that the majority of the water molecules will hit and stick the sample holder and the cryoshield. For this reason, water molecules put into the chamber during the direct deposition contribute marginally to the global pressure.

We have calculated that spray deposition allows the grown of about a hundred monolayers of ASW during 5 minutes of deposition (i.e. ~ 0.33 ML/s), while

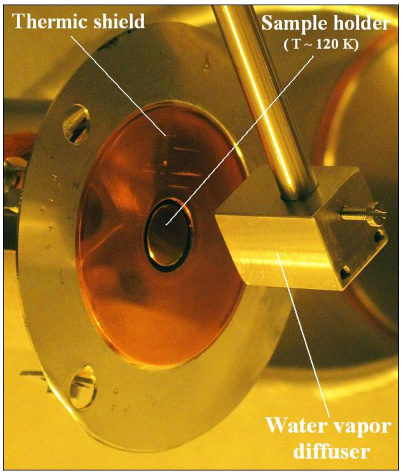

Figure 3.1.1: Photo of the water diffuser facing the sample holder surface, during a water ice grown. The temperature of the copper surface is fixed at 120 K, in order to form a compact ASW.

the residual pressure into the chamber is maintained 10^{-9} $mbar$. This method does not allow to know exactly the number of layers deposited on the sample holder; however, that is not very important: the lack of a network of pores makes the kinetics characteristics of a compact ice non dependent on its thickness. Moreover, often the compact is grown just as insulating layer over which a porous sample is created.

3.1.2 Background deposition

During the background deposition, the microchannel doser is placed high above the sample holder surface. This method provides that water vapor fills uniformly the entire volume of the chamber before its condensation on the cold surface. Hence, the angular distribution of the water molecules impinging on the sample holder from the gas phase is, in this case, fully isotropic.

An ad hoc software is able to evaluate, during each second of deposition, the quantity of molecules already stuck on the cold surface, just monitoring in real time the water partial pressure into the chamber. In fact, knowing pressure (P), temperature in the chamber (T) and mass of impinging molecules (m), the flux φ of molecules hitting the cold surface can be easily evaluated as follows:

$$\varphi = \frac{1}{4}\overline{v}n = \frac{1}{4}\,\frac{P}{KT}\,\sqrt{\frac{8KT}{\pi m}} \tag{3.1.1}$$

where $\overline{v}$ and n are respectively the molecular mean velocity and the molecular density. The factor $\frac{1}{4}$ is a geometric factor that allows for the bidimensional sample holder: in practice, $\frac{1}{4}$ is a corrective factor due to the projection of a sphere on a disk.

In theory, the sticking coefficient has to be taken in consideration. However, the sticking probability of H_2O in the range of temperature 10 - 120 K is close to unity (*Tielens*, 2005); in other words, almost 100 % of the molecules hitting the cold surface will stick on it.

It is worth stressing that background method can be used only for growth of thin ice films. In fact, as the water molecules can be adsorbed from the wall of chamber, this method could deteriorate the vacuum into the chamber, if used for long deposition.

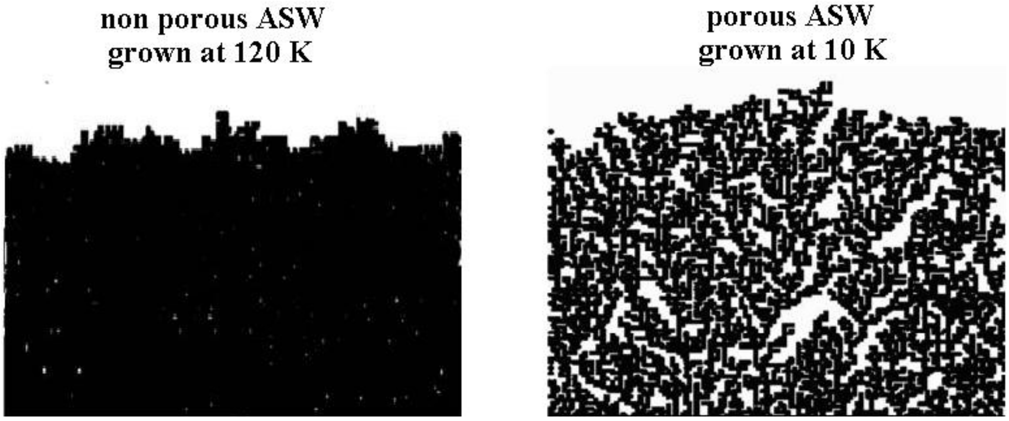

Figure 3.1.2: Two different methods allow the growing of ice films with different morphology: non porous ice (left) and porous ice (right).

In the experiments discussed in this thesis, background deposition is used to create thin films of highly porous ice on the top of a compact ASW thick substrate, previously grown at 120 K by spraying and then held at 10 K. Maintaining 10^{-8} *mbar* the value of the pressure into the chamber during the background deposition, 1 ML of water will be grown after 5 minutes, namely a rate of water growing equal to $\sim$ 0.003 ML/s.

3.2 TPD technique

3.2.1 Theoretical considerations

The Temperature Programmed Desorption (**TPD**) is a straightforward and powerful technique for the determination of kinetics and thermodynamical parameters of desorption processes. Experimentally, TPD technique is very simple: a sample surface at low temperature is heated with a linear ramp and the partial pressures of atoms and/or molecules desorbing from the sample are measured by a mass spectrometer. In particular, when the surface reaches a specific temperature, called *desorption temperature* (different for each adsorbed species), the energy transferred to the adsorbed species causes its desorption, namely the rupture of adsorption bonds and the resulting removal of adsorbed particles from the surface. By carefully controlling the temperature ramp, the time-dependent thermal desorption process can be converted to a temperature-dependent process: in this way, we can obtain additional information on properties of adsorbate and on desorption kinetics. The thermal desorption of an adsorbate specie from a cold surface follows Polanyi-Wigner law:

$$QMS\ signal \propto -\frac{d\vartheta(t)}{dt} = A_m\ \vartheta(t)^m\ e^{-E_d/kT} \tag{3.2.1}$$

where

$d\vartheta(t)/dt$ **:** the rate of desorption;

$\vartheta(t)$ **:** the coverage (i.e. the number of adsorbed atoms or molecules);

m **:** the order of the desorption process (m is an integer number, $0 \leq m \leq 2$);

A_m **:** the pre-exponential factor;

E_d **:** the energy barrier for desorption;

k **:** the Boltzmann constant;

T**:** the absolute temperature.

The three following figures show the different profiles that characterize the TPD curves of zero, first and second order.

Zero-order desorption kinetics ($m = 0$)

Zero-order implies that desorption rate does not depend on the coverage, such as in the case in which desorption comes from a multilayer adsorbate. As evident in Fig.3.2.1, TPD spectra show a common leading edge for all coverages and a rapid drop when all the molecules have desorbed.

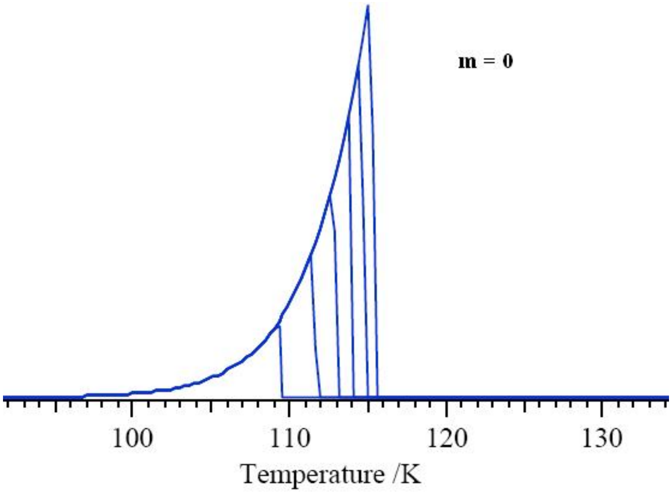

Figure 3.2.1: Typical thermal desorption profiles of zero-order.

First-order desorption kinetics ($m = 1$)

First-order implies that desorption rate is proportional to the instantaneous coverage. It corresponds to the thermal desorption of molecules already adsorbed on the cold surface. As evident in Fig.3.2.2, peak positions in desorption spectra does not change with the coverage; moreover, peak shapes are asymmetric.

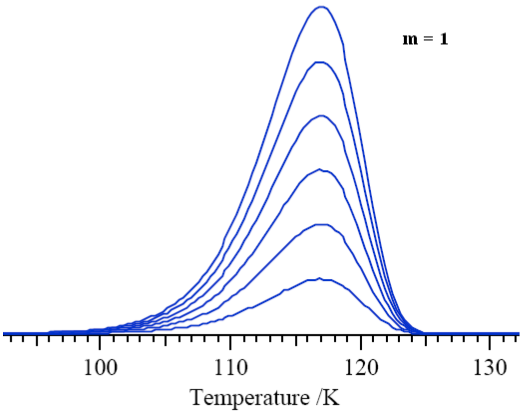

Figure 3.2.2: Typical thermal desorption profiles of first-order.

Second-order desorption kinetics ($m = 2$)

Second-order implies that the desorption rate is proportional to the square of the adsorbate density. It is observed when the reaction occurs between two adsorbate species that become mobile on the surface during the heating and react with each other before desorbing. Fig.3.2.3 shows a common high temperature tail; moreover the position of the maximum shifts to lower temperature with increasing the coverage. Each spectrum has a symmetric peak shape.

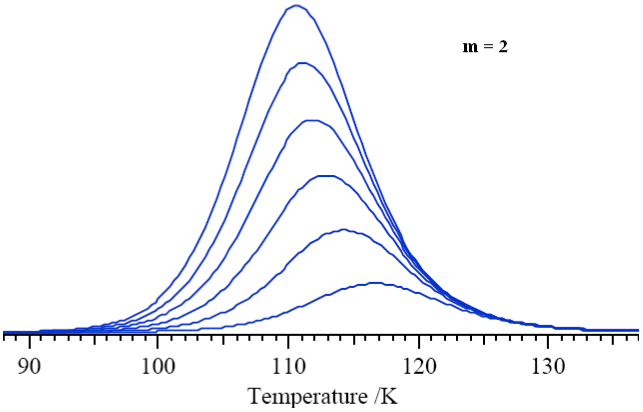

Figure 3.2.3: Typical thermal desorption profiles of second-order.

Every TPD profile presents a maximum at a fixed temperature (T_{peak}); for this reason, in this point the first derivative of the equation 3.2.1 will be zero. Thus, the energy of desorption (E_d) can be obtained by differentiating that equation:

$$\frac{d^2\theta(t)}{dt^2} = 0 \quad \Rightarrow \quad E_d = kT\,\frac{\nu_m}{\beta}\;m\theta(t)^{m-1}\;e^{-E_d/kT} \tag{3.2.2}$$

where $\beta = dT/dt$ represents the rate of sample heating.

Unfortunately, as the energy appears in both members of equality, the equation 3.2.2 cannot be solved analytically, but only graphically.
Moreover, the pre-exponential factor (ν_m) has a value not always constant; in fact, as discussed in *Amiaud et al.* (2006), there is often a correlation between ν_m and E_d. It is possible to uncouple the two terms, although the method demands complex analysis that are not related to the aims of this thesis. We can just keep in mind that, in case of first order desorption, ν_1 corresponds to the vibrational frequency of the molecules at the surfaces and its value is typically considered to lie between 10^{12} and 10^{13} s^{-1}, at least for low mass molecules, as D_2.
Eventually, it is worth noting that the area subtended by each TPD profile is proportional to the amount originally adsorbed, namely proportional to the surface coverage. Moreover, the position of the peak is related to the enthalpy of adsorption, or, in other words, to the strength of binding to the surface. So, when multiple peaks are observed in a TPD spectrum, it means that there are more binding states for the adsorbed molecules on a surface.

3.2.2 Study of ice morphology through TPD technique

Thermal desorption of a previously adsorbed specie allows to characterize the morphology of a icy sample. The influence of the surface porosity on the desorption kinetic of molecules deposited on ASW at low temperature is widely known in literature (for instance, look at *Fillion et al.*, 2009 or *Ayotte et al.*, 2001). This probing method is also used in the experiments discussed in the next chapters.
In practice, the icy sample maintained at 10 K (the temperature chosen for our experiments) is exposed to a certain amount of D_2. After that, the mass spectrometer is placed in front of the surface, that is then heated following a

linear heating ramp of 10 K/min up to 32 K, while the QMS monitors the desorption signal of D_2. For each water ice structure, D_2 desorption has a unique TPD profile and a unique desorption temperature.

For several reasons (*Amiaud et al.*, 2006), D_2 seems to be the more appropriate molecule for our kind of experiments: first of all, diffusion of molecular hydrogen within the connected network of pores in an ASW results efficient at 10 K, by contrast with other gases. Moreover, D_2 is weakly bound to the surface and its desorption occurs below 30 K: this temperature limit is not high enough to induce severe transformations of the ice structure, that, on the contrary, occurs using the thermal desorption of other species. Therefore, the thermal desorption of molecular hydrogen or deuterium adsorbed on an amorphous ice is particularly sensitive to the morphology of the sample. That appears clear in Fig.3.2.4 that shows two TPD spectra relative to D_2 desorption from a non porous ASW (solid line) and from an highly porous ASW (dashed line): no significant desorption is measured above 21 K from the compact surface, whereas desorption from the porous surface persists up to 25 K. Therefore, the higher the porosity is, the higher is the desorption temperature. So, the different positions between the two desorption peaks stress that porous ice is characterized by sites with higher binding energy.

TPD experiments using D_2 are very sensitive to the ice thickness as well as the morphology. In fact, Fig. 3.2.5 shows a comparison of several TPD spectra relative to D_2 desorption from a compact ASW (curve(a)) and from different thickness of highly porous ices grown over compact ice. These TPD spectra are obtained at equivalent low D_2 exposure (~ 0.15 ML): their peaks shift to higher temperatures as the porous ice network is progressively formed. In other words, the formation of more energetic binding sites is related to the increasing porous ice thickness. In fact, as evident in Fig. 3.2.5, the overlap with the profile relative to D_2 desorption from compact ice is important for the film of 1 ML of porous ice, but it becomes gradually smaller with the increasing of the porous ice films. In a very recent work, *Fillion et al.* (2009) have stressed that an ultra-thin film of porous ice (≤ 5 ML) grown on the top of a compact ice substrate shows behaviours characteristic of a non porous ice too: in this case, the experimental D_2 TPD profile can be simulated by fitting a convolution of two TPD profiles seen for compact and porous ice.

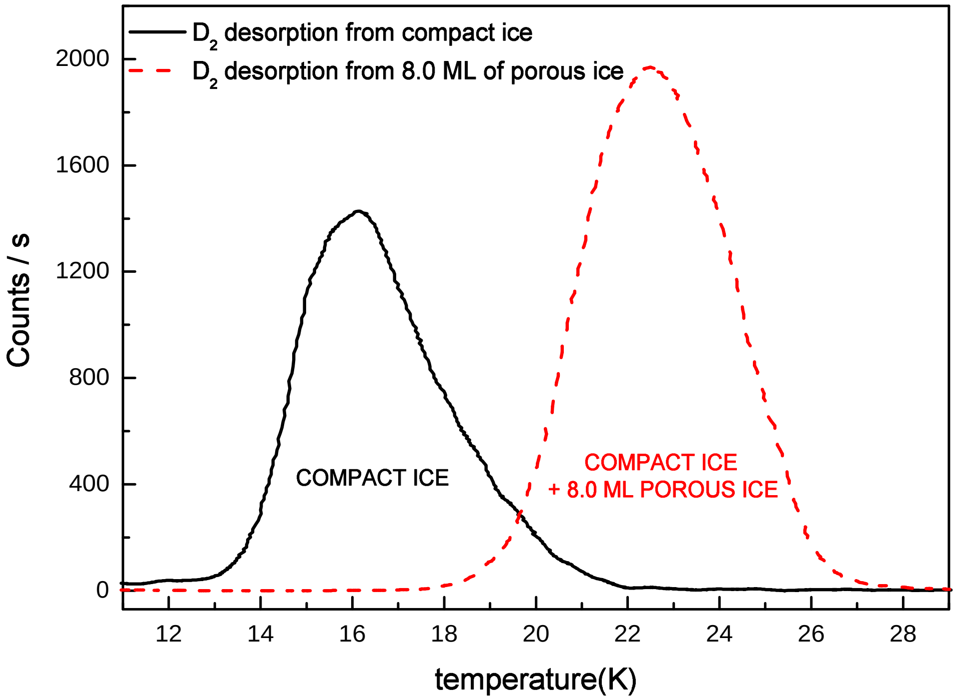

Figure 3.2.4: TPD spectra of 0.15 ML D_2 adsorbed on a compact ASW (solid line) and on 8.0 ML of highly porous grown over a compact ice ASW (dash line). The linear heating ramp used for these TPDs is 10 K/min.

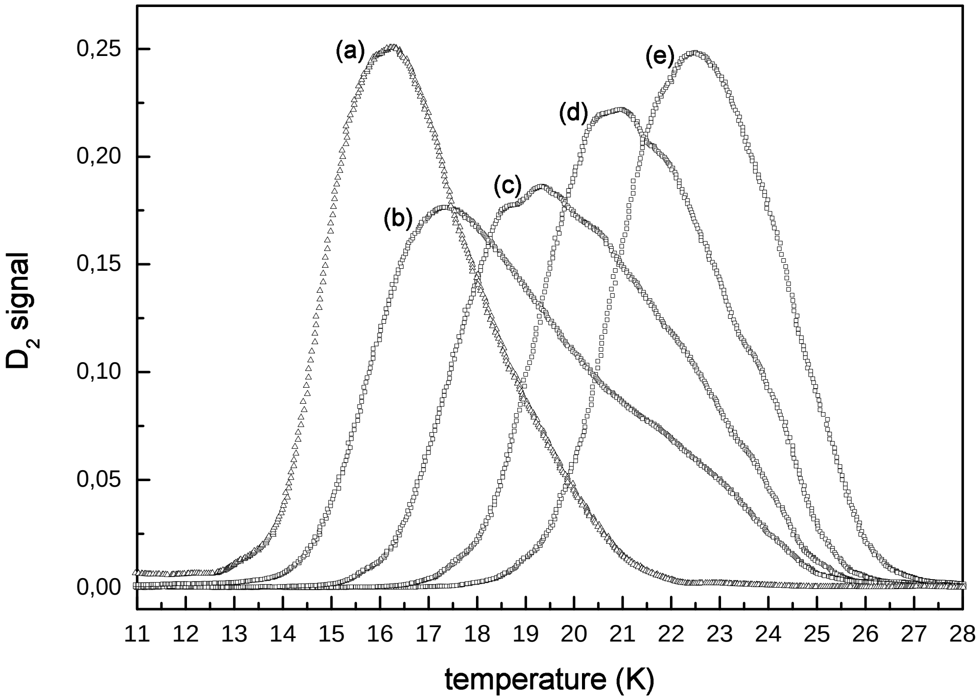

Figure 3.2.5: Comparison of TPD spectra obtained after equivalent D_2 exposure ($\sim$ 0.15 ML) from compact ice (**a**) and from different thickness of highly porous ices grown over a compact ice: compact + 1ML porous ASW (**b**), compact + 2ML porous ASW (**c**), compact + 4ML porous ASW (**d**) and compact + 8ML porous ASW (**e**).

3.3 Flux calibration of the beams

In the experiments that will be described in the next chapters, it is crucial to know how many molecules or atoms are aimed each second on the sample's surface during the irradiation. In fact, our final purpose is to link the experimental results with the astrophysical evidences, that come from the observations. We know that the flux of interstellar particles is many order of magnitude lower than experimental one: the order of magnitude of the atomic hydrogen flux in a molecular clouds is $\sim 10^5$ *atoms / s* cm^2 (*Li & Goldsmith*, 2003), while the D-atoms flux in FORMOLISM set-up is $\sim 10^{13}$ *atoms / s* cm^2. However, considering the so-called *fluence* (namely, the number of incident particles per unit area), our experiments can reproduce in some minutes the chemical-physical reactions occurring in thousands of years in an interstellar cloud. For this reason, it is important to know as accurately as possible the number of the impinging particles during the irradiation: in fact, a rough estimation of the experimental fluences in the beam lines could lead to incorrect conclusions from the astrophysical point of view.

3.3.1 Calibration of deuterium beam

In order to evaluate the flux of D_2 molecules coming from the experimental beam, the so-called *King and Wells method* has been used. This experimental method, accurately described by *Amiaud et al.* (2007), is generally used to measure the sticking coefficient of particles incident on a surface. However, the experiments described in the above-mentioned article can be compared with similar ones that we have carried out. From this comparison, it is possible to obtain an evaluation for our experimental beams. The simple experimental procedure is described hereunder.

First of all, a non porous ASW film ($\sim$ 100 ML, as thickness) is grown at 120 K on the copper sample holder. Afterwards, the icy sample is cooled down until 10 K and then irradiated with molecular deuterium. At the same time, the mass spectrometer (placed out of the beam axis) detects the indirect D_2 signal in the vacuum chamber in the real time. The variation of the D_2 signal with the time monitored by QMS and shown in Fig.3.3.1 arises from the interaction between deuterium molecules and ice surface. In fact, this is the interpretation of the Fig.3.3.1: D_2 exposure begin when the beam is released into the main chamber at $t = 0$ s. During the first 50 s, a linear

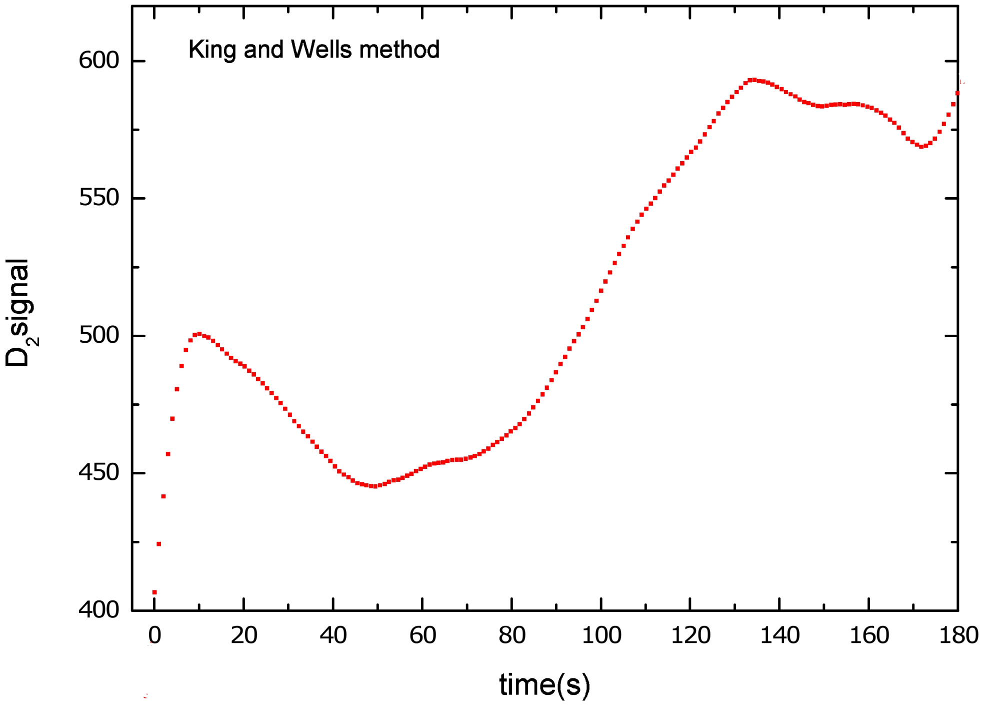

Figure 3.3.1: Background signal of molecular deuterium detected into the chamber by the mass spectrometer during the D_2-atoms exposure of a compact ice. The D_2 signal trend allows the calibration of the molecular beam (see text for details)

decrease of D_2 signal is observed; then, there is a rising edge that reaches a plateau at $t = 130 - 140$ s: the plateau lasts as long as the surface is exposed to the beam. Indeed, this region represents the steady state regime, because the number of molecules hitting the surface is equal to the number of molecules escaping from it. On the contrary, the initial decrease of D_2 signal ($0s < t < 50s$) can be interpreted as an increase of the sticking coefficient in the icy sample. Because of the gradual saturation of the surface after 50 s, the D_2 signal into the chamber begins to increase, thereby stressing that a lower number of molecules are sticking on the compact ice film.

According to the estimation made by *Amiaud et al.* (2007), a compact ice grown using our method begins to saturate after an exposure to 0.45 ML of D_2 (i.e. 0.45×10^{15} mol/cm^2). Between our experiments and Amiaud's ones, the only parameter than can change is the beam flux. Hence, in conformity with the results already discussed, as our ice film begins to saturate after 50 s of D_2 exposure, the flux of D_2 beam can be determined as follows:

$$\Phi_{D_2} = \frac{0.45 \times 10^{15}}{50} \approx 9.0 \times 10^{12} \; mol/cm^2 s \tag{3.3.1}$$

In order to evaluate the atomic deuterium flux, first of all we have to know the rate of molecular dissociation (τ) when the microwave cavity works. It is not hard to work out τ, every time the atomic beam is aimed at the surface of the sample holder. For this purpose, the mass spectrometer must be placed in front of the atomic beam: in this way the QMS is able to monitor the direct signal due to the molecular deuterium when the microwave discharge is on and when it is off. Therefore, analysing the variation of the D_2 signal detected by QMS and shown in Fig. 3.3.2, the fraction of gas dissociated in the beamline can be simply evaluated as follows:

$$\tau = 1 - \frac{ON - BKG}{OFF - BKG} \tag{3.3.2}$$

where

ON : D_2-signal detected by QMS, when the microwave cavity is turned on

OFF : D_2-signal detected by QMS, when the microwave cavity is turned off

BKG : it is the background signal detected by the mass spectrometer, and normally present in the chamber

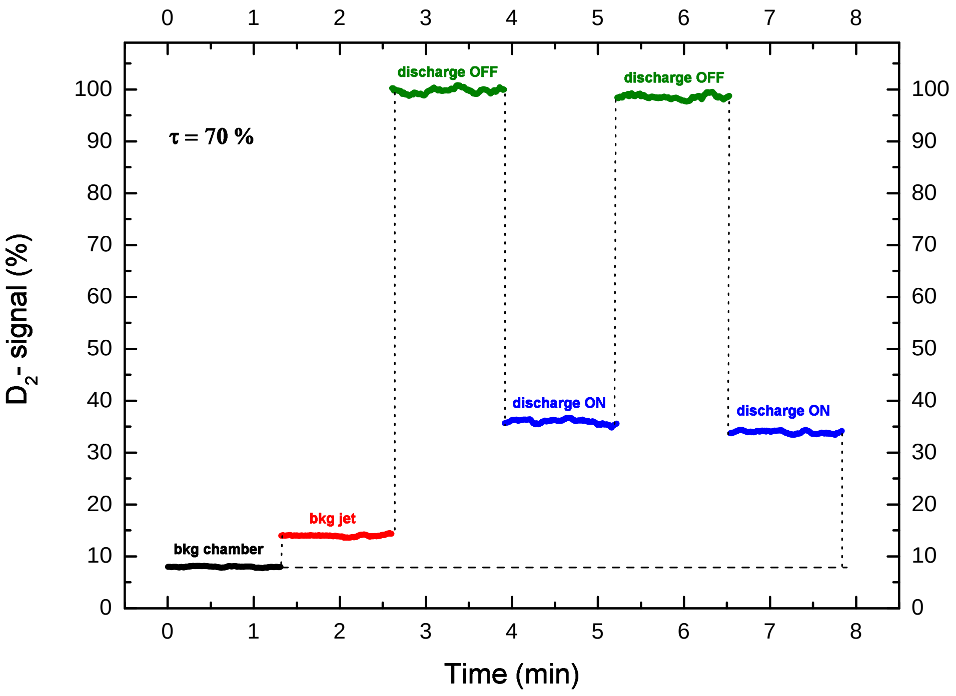

Figure 3.3.2: D_2 signal detected in the chamber by the mass spectrometer before (black curve) and after the opening of beam valve. The highest D_2 signals (green curves) are detected when the RF cavity is not in operation. Blue curves represent the D_2-signal, when the RF cavity does work. When the beam valve is barely open, the QMS detects the background signal of the molecular jet (red curve)

Although almost negligible for our estimation, red line in the Fig.3.3.2 shows that, when the beam valve is open, a small fraction of D_2 signal ($< 5\%$) is due to the background signal of the jet. Of course, this signal comes from the jet, even if it depends on the molecules that arrive to the detector following different paths. We are able to detect the background signal when the beam valve is barely opened.

According to the experiment shown in Fig. 3.3.2, the rate of molecular dissociation is $\sim 70\% \pm 1\%$. However, the value of τ is not always the same: for example, it can vary between 60% and 90% for molecular deuterium.

Hence, knowing the value of τ, it is possible evaluate the atomic flux as follows:

$$\Phi_D = 2 \times \tau \times \Phi_{D_2} = 1.2 \times 10^{13}\ mol/cm^2s \tag{3.3.3}$$

where the factor 2 in the equation arises from the fact that the cracking of D_2 produces two atoms of D.

3.3.2 Calibration of O_2 beam

A different method has been utilized in order to evaluate the experimental beam of molecular oxygen. But even in this case, the O_2 beam calibration is performed by determining the exposure time corresponding to saturation coverage of the first monolayer of O_2 adsorbed on amorphous water ice. The procedure is explained hereafter.

In practice, an amount of molecular oxygen is grown on a substrate constituted by a non-porous amorphous ice maintained at 15 K. Then the sample is heated with a linear ramp up to 45 K, while the mass spectrometer monitors the thermal desorption of O_2. Afterwards, the temperature of the ice surface is cooled again to 15 K, and the identical procedure can be repeated once again, but growing a greater amount of O_2. Fig.3.3.3 shows the result of this experience, obtained iterating many times the aforesaid procedure: we can see a series of O_2 TPD spectra corresponding to increasing coverages of O_2 on compact ice. Indeed, when a dose greater than 1 ML of O_2 is deposited on the non-porous ice substrate, the shape of its corresponding TPD spectrum changes: multilayer peak in the $\mathrm{O_2}$ TPD profile starts to show up, thereby marking the saturation of the first monolayer and the desorption of O_2 from the second layer. The feature that denotes in TPD spectra the desorption

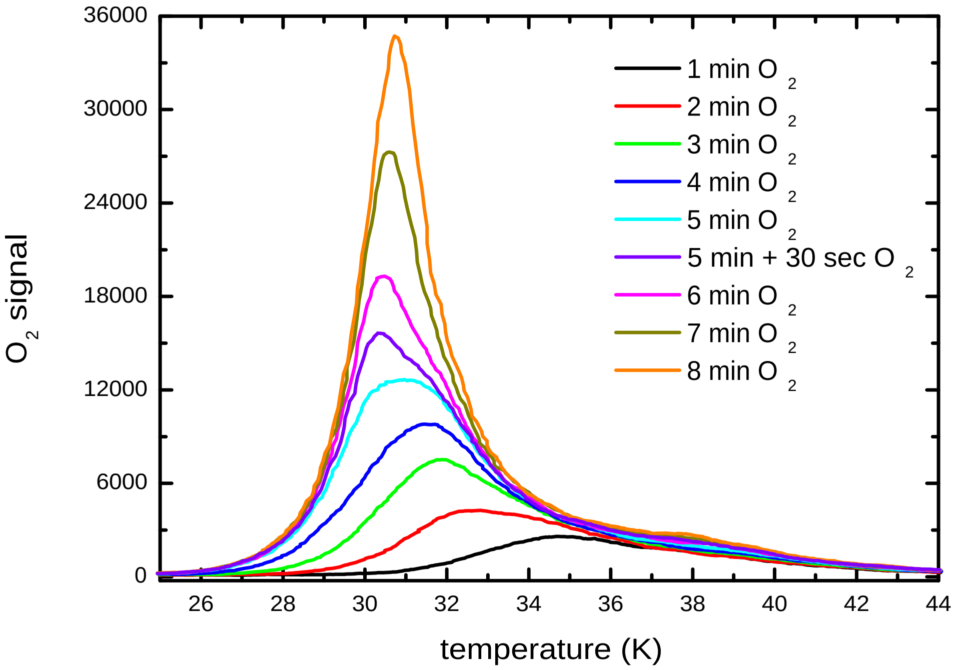

Figure 3.3.3: Temperature programmed desorption of O_2 from a compact non porous ASW. The different O_2 exposure are displayed in the figure

from the second layer ($\sim$ 31 K) begins to appear after doses larger than 6 minutes of O_2 exposure (Fig. 3.3.3).

Modelling of TPD traces

The submonolayer O_2 TPD spectra can be fit using the first-order desorption, whereas higher O_2 coverages give rise to a second peak at lower temperature ($\sim$ 31 K), which exhibits zero-order kinetics, "signature" of the multilayer desorption (Fig.3.3.3). Therefore, the experimental thermal desorption from O_2 multilayers can be simulated by fitting the convolution of two different rates of desorption: the first-order desorption for the first layer of O_2 and the zero-order desorption for the other layers of O_2. The good agreement between simulated and experimental TPD spectra can be seen in Fig.3.3.5.
To extract the kinetic parameters of desorption, it has been used the direct inversion of the Polanyi-Wigner equation (eq.3.2.1). For the first layer of O_2, the choice of the first-order desorption ($m = 1$) seems reasonable. On the other hand, for the sake of simplicity, the pre-exponential factor of desorption (ν_m in eq.3.2.1) has been assumed constant: $\nu_1 = 10^{15}\ s^{-1}$, as reported in *Schlichting et al.*, 1993. This simplification is widely assumed by several authors in this kind of simulations, even if it is known the correlation between ν_m and the coverage θ.
Therefore, considering all the aforesaid assumptions, we can derive the desorption energy ($E(\theta)$) for each TPD spectrum relative to the submonolayer coverage as follows:

$$E(\theta) = -kT \ln\left[-\frac{d\theta/dT}{\nu_1\ \beta\ \theta}\right] \tag{3.3.4}$$

where $\beta = dT/dt$ is the heating rate ($\beta = 10\ K/min$, in our experiments).
The $E(\theta)$ curve extracted from the TPD spectrum corresponding to $\sim$ 1 ML dose (red data points of Fig.3.3.5) is shown in Fig.3.3.4. The desorption parameters, ν_1 and $E(\theta)$, can then be used to simulate the complete set of submonolayer desorption spectra by numerical integration of the Polanyi-Wigner equation.

For higher coverages than 1 ML, it is not hard to distinguish in TPD spectra the feature due to zero-order desorption from the second layer of adsorbed O_2. A simple leading edge analysis of the zero-order desorption rate from the second-layer peaks allows to evaluate the pre-exponential factor

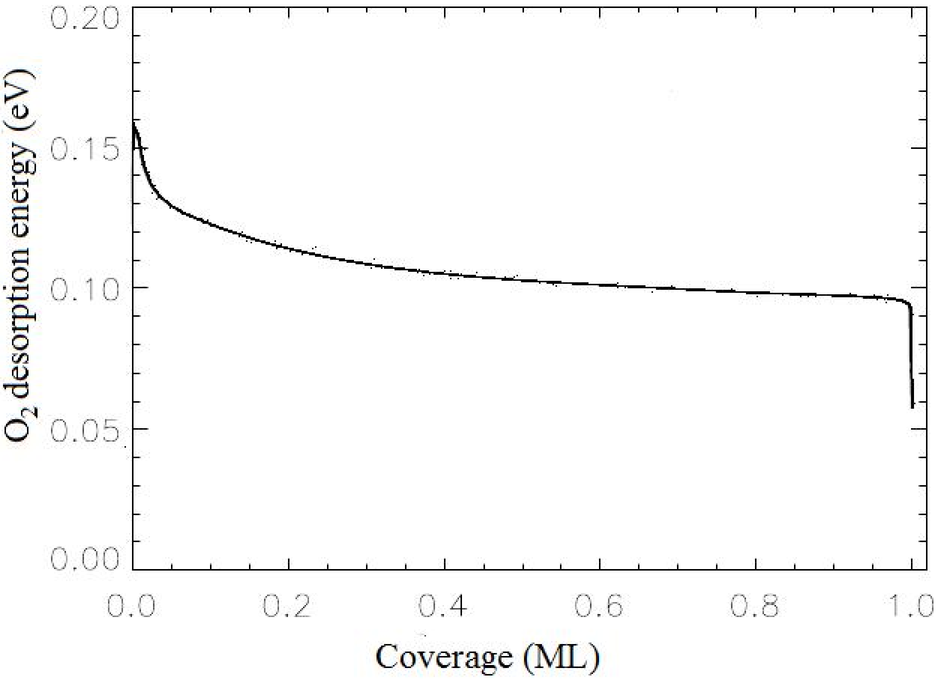

Figure 3.3.4: Desorption energy vs relative O_2 coverage obtained from the 1 ML TPD spectrum shown in Fig.2 (red data points) by inversion of the Polanyi-Wigner equation.

($\nu_{multi} = 6.11 \times 10^{17}\ s^{-1}$) and the desorption energy ($E_{\mathrm{multi}} = 0.124\ eV$). Fig.3.3.5 shows the result of our simulation. For thickness larger than 1 ML, the convolution among the first-order desorption of the first layer of O_2 and the zero-order desorption of the other layers of O_2 is in good agreement with the experimental curves, thereby providing some confidence in the coverage θ inferred at the beginning.

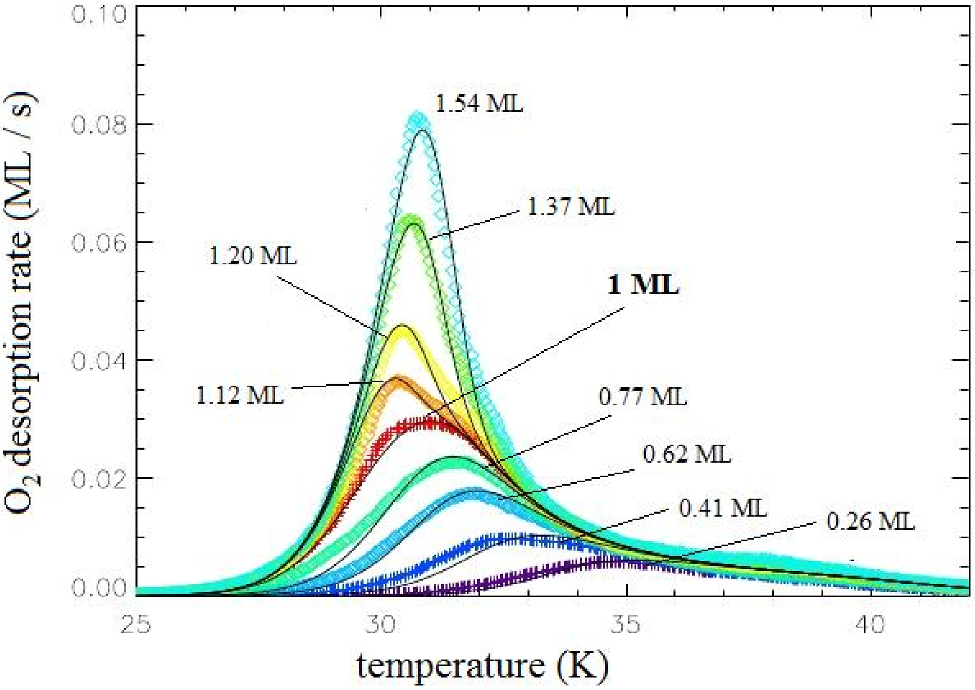

Figure 3.3.5: O_2 TPD spectra after various exposures to O_2 beam (1, 2, 3, 4, 5, 5.5, 6, 7, 8 minutes) on a compact ice surface. Simulated TPD spectra are over-plotted on the experimental curves (see text for detail about the method of simulation).

Chapter 4

Hydrogen exposure of interstellar ice analogues

Although it is widely accepted that H_2O ice in dense molecular clouds is amorphous (*Smith et al.*, 1989), there is still poor knowledge about its degree of porosity. However, in the last years, observations (e.g. *Keane et al.*, 2001) and laboratory experiments (e.g. *Palumbo*, 2006; *Raut et al.*, 2007) seem to indicate the predominant non-porous nature of interstellar ices. Ice porosity may be identified in the laboratory through the weak infrared absorption feature (~ 2.7 μm) related with the presence of dangling OH-bonds on the porous surface. To our knowledge, there has been to date no detection of such absorptions in the infrared spectra of interstellar ices. On the other hand, laboratory simulations have recently confirmed that interstellar porous ice may be compacted quite efficiently by the transient heating of UV stellar radiation (*Chakarov et al.*, 1998) and by cosmic ray bombardment (*Palumbo*, 2005 and *Raut et al.*, 2008).

The experimental work described in the present chapter shows how relevant changes in the ice morphology are possible even as a consequence of atomic hydrogen exposure and its recombination on the icy surface. In particular, it is shown that a thin highly porous ice film is gradually changed into a more compact structure, following D-atoms exposure. This phenomenon is probably due to the transient heating caused by the energy released to the ice during H_2 formation, when two hydrogen atoms encounter each other on the icy surface; the local heating thus might change the local morphology, acting like a sort of local annealing. Therefore, even if we grant for the sake of argument that the water ice is porous at the beginning, the hydrogen recombination on the surface of interstellar ice mantles can compact their structure concurrently with the other envisaged process.

4.1 The experimental method

In the present experiments, we have studied the effect of D-atoms exposure on porous ASW samples of five different thickness, ranging from 1 to 8 ML. Fig.4.1.1 summarizes schematically the experimental procedure utilised in our experiments, for each ice thickness:

1. the copper sample holder is cooled down to 120 K;
2. a film of $\sim$ 100 ML of compact ASW is grown by spraying on the cold surface. This film is used as an insulating layer over which a porous ASW layer will be grown;
3. the sample holder and the compact film are now cooled down to 10 K;
4. the morphology of the compact film is probed. In practice, the ice is exposed to 30 s of D_2 flux ($\sim$ 0.15 ML of D_2); then, the sample is heated to 30 K with a linear ramp (10 K/min), while the mass spectrometer monitors the thermal desorption of D_2;
5. the sample holder and hence the compact film are cooled again till 10 K. Afterwards, a sample of few monolayers of porous ASW is grown over the top of the compact ice by background deposition. Then, the newly formed sample is annealed to 30 K, in order to stabilize the surface morphology before subsequent heating sequences;
6. the morphology of the sample is tested using the method described above (point 4);

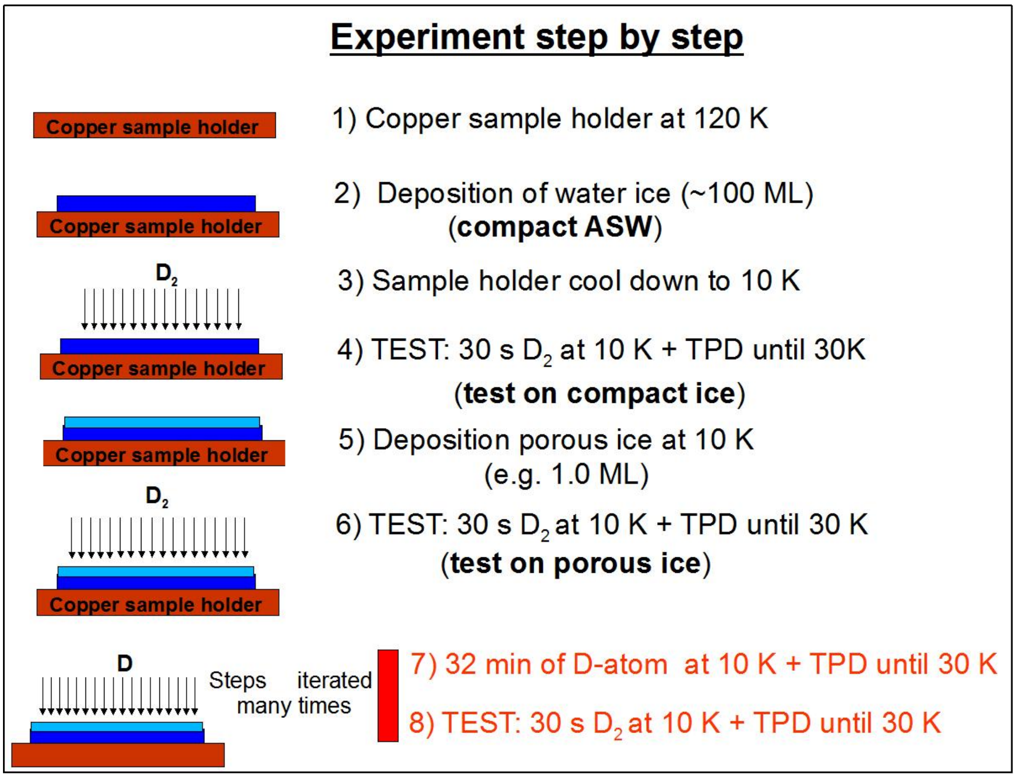

Experiment step by step

1) Copper sample holder at 120 K

2) Deposition of water ice (~100 ML) (**compact ASW**)

3) Sample holder cool down to 10 K

4) TEST: 30 s D_2 at 10 K + TPD until 30K (**test on compact ice**)

5) Deposition porous ice at 10 K (e.g. 1.0 ML)

6) TEST: 30 s D_2 at 10 K + TPD until 30 K (**test on porous ice**)

Steps iterated many times

7) 32 min of D-atom at 10 K + TPD until 30 K

8) TEST: 30 s D_2 at 10 K + TPD until 30 K

Figure 4.1.1: Experimental procedure utilised in our experiment, step by step

7. **the sample (at 10 K) is exposed to a flux of D-atoms for a fixed time interval. At the end of each interval, the temperature of the sample is increased to 30 K. In this way, it is completely removed both the molecular deuterium formed into the ice when two D atoms encounter each other and also D_2 molecules coming as an undissociated fraction directly from the source, that does not produce pure D atomic beam;**

8. **the porosity of the irradiated sample is checked using the method described above (point 4).**;

Points **7** and **8** have been iterated many times: in this way, it is possible to study the evolution of the ice morphology as a function of D-atoms fluence. It is important to stress that the collapse of the porous structure in an icy film can be considered irrelevant during each TPD experiment involving the desorption of molecular hydrogen in the 10-30 K temperature range. In fact the annealing up to 30 K at the beginning (point 5) serves to arrange water molecules on the surface.

4.2 The experimental results

Films of highly porous ice are, thus, exposed to D-atoms fluxes in order to study the evolution in their morphology. After each time interval of D-atoms exposure, the morphology of the irradiated sample is probed, according to the method described in details in the paragraph 3.2.2. In practice, the sample is exposed to a certain amount of D_2. Then, heating the sample with a linear ramp (10 K/min), D_2 thermal desorption is monitored through the mass spectrometer. The different TPD spectra obtained in such a way before and after hydrogen exposure (see Fig.4.2.1) give us information about the evolution of the ice morphology as a function of D-atoms fluence. This procedure is repeated for every ice thickness analysed.

Fig.4.2.1 shows the effects of D-atoms exposure on the morphology of two different ice thickness: 1 ML (Fig.4.2.1a) and 4 ML (Fig.4.2.1b) of porous ASW. TPD profiles due to thermal desorption of D_2 from samples exposed to atomic hydrogen (see in the figure spectra (iii) and (iv) for 1ML and spectra (vii), (viii) and (ix) for 4 ML) show their gradual transformation from

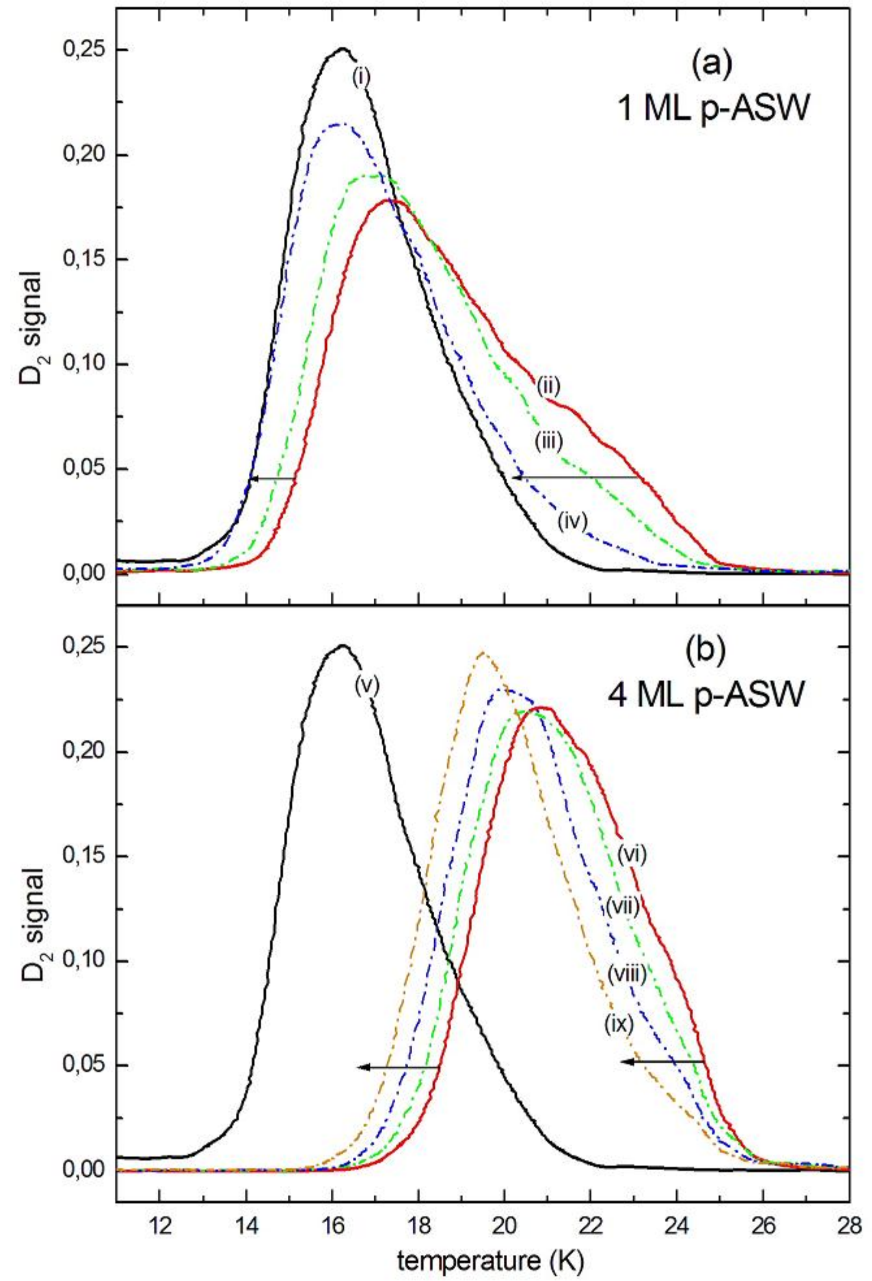

Figure 4.2.1: Normalised TPD spectra of ≈ 0.15 ML of D_2 from 1 ML (**a**) and from 4 ML (**b**) of porous ASW, before and after D-atoms exposure. In particular, in the upper figure (**a**) it is shown the thermal D_2 desorption from a bare compact ASW (i) and from 1 ML of porous ice, before D-atoms exposure (ii) and after 64 min (iii) and 160 min (iv) of D-atoms exposure. In the lower figure (**b**) it is shown the thermal D_2 desorption from a bare compact ASW (v) and from 4 ML of porous ice, before D-atoms exposure (vi) and after 64 min (vii), 224 min (viii) and 288 min (ix) of a flux of atomic deuterium.

porous toward compact films. In fact, a progressive leftward shift towards lower temperatures occurs in the thermal desorption peaks while the hydrogen (deuterium) fluence on the sample increases, as the arrows indicate in the figure. Similar changes in the peak position of the TPD spectra are observed for the other ice thicknesses analysed, but not shown here: it seems that thinner is the sample faster is its compaction.
Finally, it is worth stressing that our set of experiments has also demonstrated that the compaction is strictly due to the atomic hydrogen (deuterium) recombination that takes place on the surface of interstellar ice analogues; in fact, no changes of ice morphology has been observed for a porous ice film, after a long molecular deuterium exposure.

4.3 Analysis of the experimental data: method of direct inversion

4.3.1 Description of the method

Our experimental evidences have shown that after atomic hydrogen (deuterium) exposure the porous structure of water ice is partially collapsed. Therefore, it is worth studying how the distribution of the adsorption sites in the irradiated ice changes as a function of D-atoms fluence.
A first analysis of the experimental data can be obtained by the so-called *method of direct inversion*, namely the direct inversion of the different D_2 TPD curves (this method is widely known: look for example *Zubkov et al.*, 2007).
It has already been discussed in the paragraph 3.2 that the thermal desorption is a powerful technique used to obtain information on the kinetics of reactions. Each TPD spectrum follows the *Polanyi-Wigner equation* (see eq.3.2.1). Assuming our TPD spectra are of the first-order, by inverting the Polanyi-Wigner equation, we can obtain the desorption energy as a function of D_2 molecules still present on the surface ($E(\vartheta)$) as follows:

$$E(\vartheta) = -kT \ \ln \frac{r}{A\vartheta} \tag{4.3.1}$$

where $r = -d\vartheta/dt$ is the rate of change of coverage, ϑ the number density of molecular deuterium adsorbed on the ice surface at each instant, A is

the so-called pre-exponential frequency factor, k is the Boltzmann constant and T the absolute temperature. The pre-exponential factor, in the case of first-order desorption, corresponds to the vibrational frequency of molecules in the adsorption site, and is typically considered to be between 10^{12} and $10^{13}\ s^{-1}$ (*Amiaud et al.*, 2006). For our experimental data, we have chosen $A = 10^{13}\ s^{-1}$
Therefore, through eq.4.3.1, it is possible for each TPD curve to plot the trend of the coverage-dependent desorption energy ($E(\vartheta)$) as a function of instantaneous coverage of D_2 (see Fig.4.3.1). Otherwise, by reversing the viewpoint, each point of each curve in Fig.4.3.1 gives us information about the number of D_2 molecules still bound to the icy sample with a given energy.

Actually, Fig.4.3.1 stresses that adsorption sites with an energy greater than 53 meV can be certainly associated with porous ice, whereas sites with lower energy can be associated with both ice morphologies either compact or porous. In fact, the trends of $E(\vartheta)$ shown in Fig.4.3.1 emphasize that a compact ice film has sites with depth never larger than 53 meV, that, on the contrary, characterize even an ultra-thin porous ice film. Actually, even the overlap of the TPD curves in the 17-21 K temperature range in Fig.4.2.1 between compact and porous ice sample can be interpreted as an uncertainty about the morphology of the ice. Indeed, as discussed in details in *Fillion et al.* (2009), for porous ice layers thinner than 5 ML, the contribution of the compact underlayer is not negligible. In fact, the effective binding-energy distribution can be represented by using a linear combination of two energy distribution, one associated to a bare compact ice and the other associated to a porous ice film.
Let's just consider sites certainly linked to the porous structure of the ice, i.e. sites of energy higher than 53 meV. Fig.4.3.1 shows that for 1 ML, the number of the most energetic binding sites in the ice decreases gradually while increasing the D-atoms fluence on the sample; for instance, the number of molecules bound to 1 ML porous ASW with energy 60 meV is greater in the sample irradiated with 64 min of D-atoms than in the same sample irradiated with 224 min of D-atoms, demonstrating the progressive compaction of the sample after D-atoms exposure.

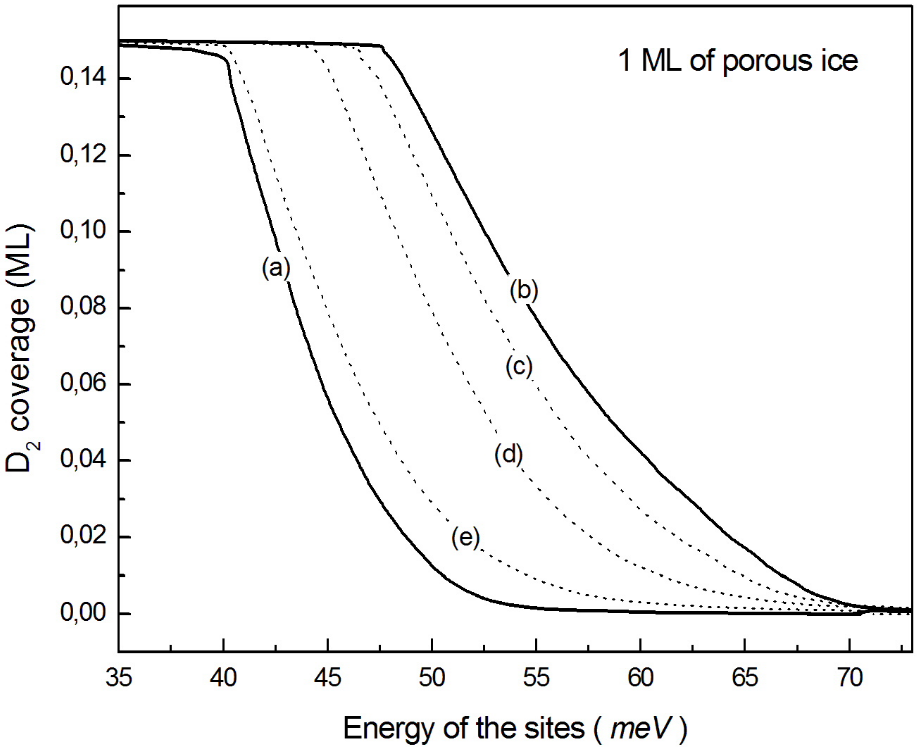

Figure 4.3.1: D_2 coverage vs desorption energy. It is evaluated the distribution of the adsorption sites for a compact ASW (**a**), for 1 ML of porous ice, before D-atoms exposure (**b**) after 64 min (**c**), 160 min (**d**) and 224 min (**e**) of D-atoms exposure.

4.3.2 Porosity reduction

It is possible to follow the evolution of the ice porosity as a function of D-atoms exposure. For this purpose, it has been evaluated how, for each ice thickness analysed, the distribution of the higher binding sites changes as consequence of D-atoms exposure.

In Fig.4.3.2 it is shown the fraction of D_2 molecules bound to the surface of the sample with energy $> 66\ meV$. The adsorption sites with energy greater than 66 meV are strictly related to the area subtended by each TPD curve

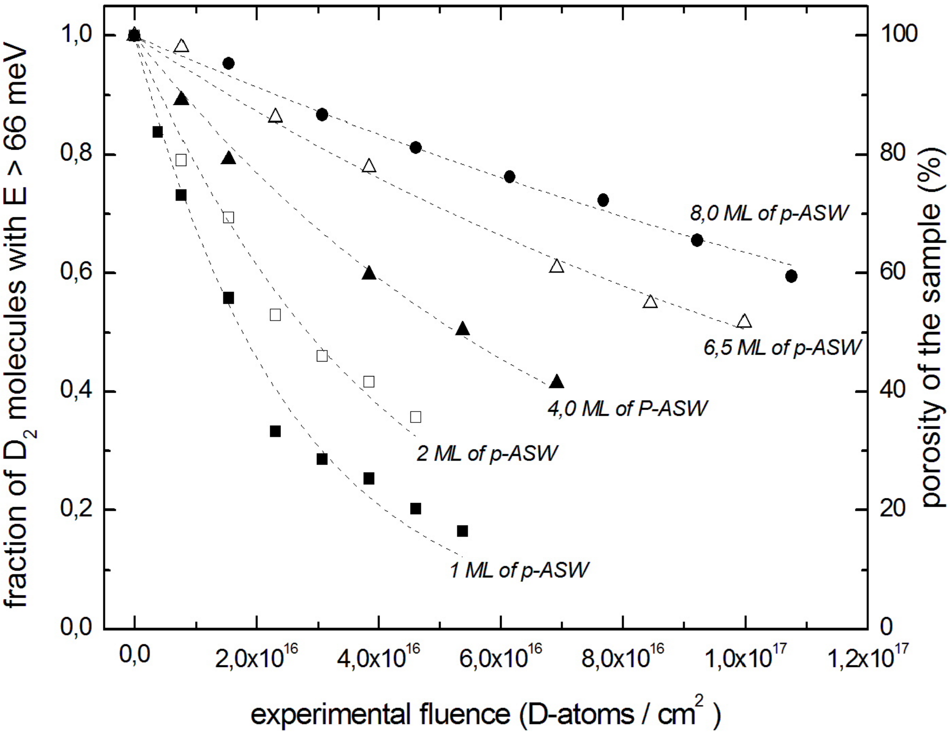

Figure 4.3.2: Fraction of D_2 molecules remaining on the ice surface in sites of depth larger than 66 meV vs D-atoms fluence, for different thicknesses of ice: 1 ML plain squares; 2 ML empty squares; 4 ML plain triangles; 6.5 ML empty triangles; plain circles 8 ML.

for temperatures higher than 22.5 K. In fact, the trailing edges of the TPD traces give information on the distribution of adsorption sites available in the ice, thereby giving a "signature" of the ice morphology. We will discuss later about the choice of the cutting value of 66 meV.
We see in Fig.4.3.2 that, for each ice thickness, the number of molecules bound on the surface of the sample with an energy larger than 66 meV decreases gradually, while increasing the D-atoms fluence. As it appears clear in Fig.4.3.2, the experimental points for each ice thickness are well fitted by an exponential decrease with an unique adjustable parameter. Each exponential curve can be identify by a characteristic value that can be expressed both in term of the time of D-atoms exposure (t_c) and hence in term of the atoms fluence (φ_c). Anyway, it represents the number of D-atoms impinging on the ice (or the time of D-atom exposure) necessary to reduce by 64% its initial porosity; the values of t_c and φ_c for each exponential curve are reported in Tab.4.1.

In Fig.4.3.3, the values of φ_c extracted from the exponential curves are reported as a function of the ice thickness: for a thicker ice a greater fluence is needed to obtain the same reduction in porosity; actually it seems that, within the experimental errors, there is a linear relation between the ice thickness and the characteristic fluence φ_c.

Ice thickness (ML)	$t_c(min)$	$\varphi_c(D-atoms/cm^2)$
0.0	0	0
1.0	125.3 ± 11.2	$(3.7 \pm 0.7) \times 10^{16}$
2.0	171.8 ± 4.6	$(4.1 \pm 0.3) \times 10^{16}$
4.0	268.6 ± 24.5	$(7.0 \pm 0.7) \times 10^{16}$
6.5	587.6 ± 20.2	$(1.4 \pm 0.1) \times 10^{17}$
8.0	765.7 ± 21.3	$(1.8 \pm 0.1) \times 10^{17}$

Table 4.1: D-atoms fluence and time of D-atoms exposure needed to reduce by 64% the initial porosity of the ice layer, for different thicknesses.

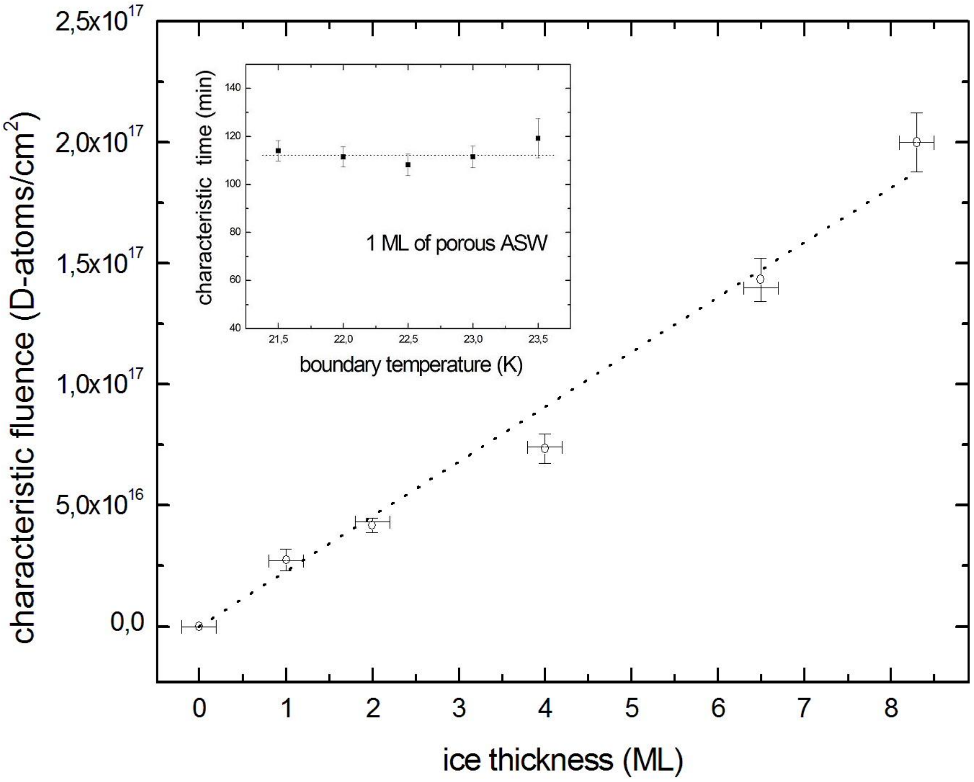

Figure 4.3.3: Characteristic fluence φ_c vs porous ice thickness. The inset shows that the characteristic time of D-atom fluence t_c is not dependent on the choice of the temperature boundary limit (see text for details).

Finally, from the slope of the linear best-fit, it is possible to extract a characteristic hydrogen fluence (φ_0) needed to destroy the ice porosity per each layer of water ice. The value thus calculated is $\varphi_0 = 2.2 \times 10^{16}\ D-atoms/cm^2$ per H_2O ML.

4.3.3 Discussion

First of all, we have to spend some words about the choice of the energy value (66 meV) used to obtain information on the ice morphology. A first logical choice might be a boundary energy of 53 meV (corresponding to 21 K on TPD curves). However, for 8 ML porous ice film, the adsorption sites with energy of 53 meV seem to be not enough populated. Actually, Fig.3.2.5 in the previous Chapter shows the thermal desorption of D_2 from layers of porous ice with thickness ranging from 1 to 8 ML: the overlap between all the trailing edges of TPD spectra is confined in the range 22.5 - 25 K, thereby accounting for the choice of the energy limit of 66 meV (corresponding to 22.5 K on TPD curves).

It is worth saying that, within the range 22.5 - 25 K, the choice of the boundary temperature (or the adsorption energy limit) is unimportant and does not change the results shown. Indeed, the inset of Fig.4.3.3 shows that, even if calculated using different boundary temperatures, the different values of t_c for 1 ML are very close each other, and thereby can be considered identical inside the error bars. Of course, the same behaviour has been observed for all the ice thicknesses studied. This means that apparently the decrease of the porosity does not seem to be dependent on the binding energy of the sites, namely the same reduction occurs independently of the binding energy of the sites. This is not obvious at first sight because we could imagine that the most bounded sites should have a larger probability to be visited from the impinging D-atoms, and thus a larger probability to be destroyed.

Therefore, the local annealing due to the atomic hydrogen (deuterium) recombination during the exposure is apparently not sensitive to the binding energy of the sites. This may mean that the probability of being in a site or in another is equiprobable, which implies that the diffusion barriers between the sites are the same or are independent from the binding energies.

4.4 Analysis of the experimental data: Thermal equilibrium model

In a previous study, *Amiaud et al.* (2006) proposed a simple statistical approach to model the distribution of D_2 on the adsorption sites in a porous ice, and its dependence on surface temperature and coverage. There are two fundamental assumptions in this model: 1) molecular hydrogen is constantly in complete equilibrium with the surface, even during the heating process; 2) molecular hydrogen explores all available adsorption sites. The binding-energy distribution is described by a polynomial function $g(E) = a(E_0 - E)^b$, where a, E_0 and b are parameters to be determined from the TPD analysis. At a given temperature and a given coverage, this distribution is assumed to be populated following a Fermi-Dirac statistical law, because one adsorption site can be filled by one molecule solely. Therefore, the population of molecules distributed over a set of available sites g(E), at a given temperature will be:

$$P(E,T,\mu) = g(E)\ (1 + e^{-\frac{E-\mu}{kT}})^{-1} \tag{4.4.1}$$

where μ is the chemical potential. Considering that the number of molecules (dn) adsorbed in sites with binding energy between E and $E + dE$ is:

$$dn = P(E,T,\mu)\ dE \tag{4.4.2}$$

The closing relation:

$$\vartheta = \int dn = \int_E P(E,T,\mu)\ dE \tag{4.4.3}$$

allows thereby the calculation of the chemical potential μ.
The heating of the sample is simulated by calculating first order thermal desorption rate expressed by the Polanyi-Wigner equation at each temperature. In practice, the variation of coverage due to a small increase of temperature during a TPD experiment is evaluated through equation 3.2.1, and thus the population distribution is continuously calculated at each temperature step through equation 4.4.1.

This model has been used also for our experimental data. The agreement between simulated and experimental TPD curves is shown in Fig.4.4.1. The simulated curves (c) and (d) in Fig.4.4.1 relative to 8 ML irradiated sample

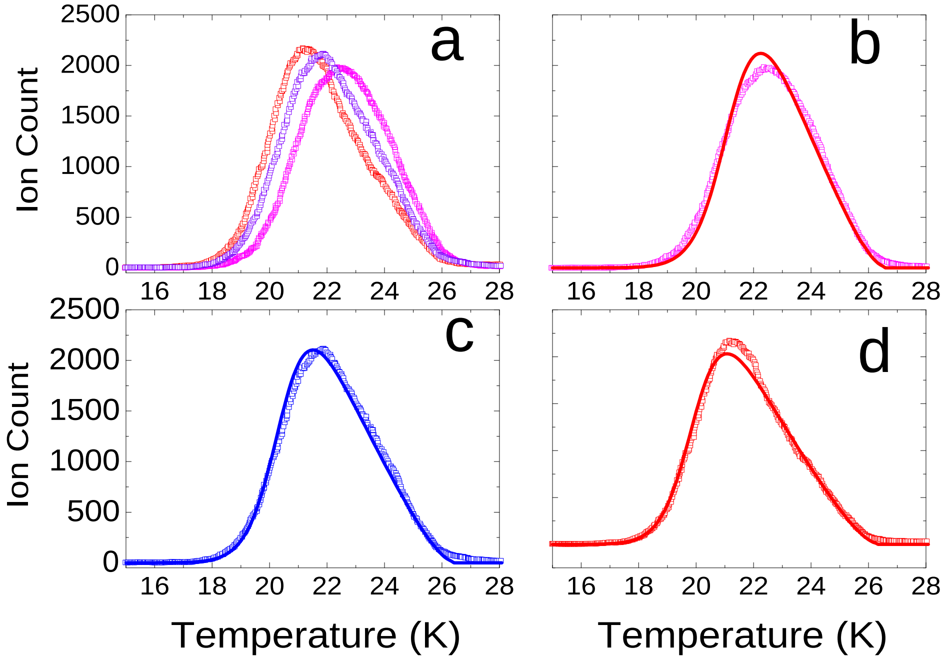

Figure 4.4.1: Scatter points: TPD curves of ~ 0.15 ML of D_2 desorbing from a porous ice of 8 ML of thickness, after no D-atoms exposure (a,b), 256 min of D-atoms exposure (a,c) and 448 min of D-atoms exposure (a,d). Solid line: TPD simulations (b,c,d) using model from *Amiaud et al.*, 2006.

are thus obtained just changing by a scale factor the number of accessible sites on the ice. The assumption (justified from the results already discussed in the previous section) is that the decrease of the ice porosity after D-atoms exposure is independent of the different binding energy of the sites. Therefore, after each time interval of hydrogen exposure, all the distribution of sites in the ice is only scaled by a constant factor R_p. The gradual reduction of the porosity (emphasized by the factors R_p) can also be plotted as a function of the time of irradiation, and an exponential decrease is also observed in this case. However, the characteristic time found is slightly higher (10 - 20%) than the value determined for the same ice thickness through the exponential decay shown in Fig.4.3.2. This difference might be attributed to the contribution of the leading edges in the TPD profiles, which are taken into account in the Fermi-Dirac equilibrium model, whereas in the case of the classical inversion, only the tails contribute to the evaluation of the distribution of energies.

The difference between the results obtained through the two methods is acceptable; for this reason we think that the *method of direct inversion* analysis is a simpler tool, that is able to give a correct description of the reduction of the ice porosity, just with one adjustable parameter (t_c).

4.5 Origin of the decrease of the porosity

The origin of the decrease of the ice porosity following the D-atoms exposure lies in the energy released (4.48 eV) when the adsorbed atoms react to form D_2 molecules. A fraction of this energy is absorbed by the ice, and can change locally its morphology, by acting like a local annealing.

Kimmel et al. (2001), by measuring the amount of N_2 adsorbed, have shown that the porosity slowly decrease with the annealing temperature until it is finally reduced to zero when annealing to 140 K. The re-arrangement of water molecules as consequence of the annealing implies the diffusion of H_2O molecules on the surface.

Let's therefore consider an activation energy for this diffusion E_d, that has as a consequence to reduce the porosity. We suppose that a unique reaction ($D + D \rightarrow D_2$) will provide locally a temperature T that gives the probability of diffusion close to one ($P_d = 1 = A\ exp(-E_d/T)$). Taken $A \sim 10^{15}$ s as the molecular dynamic time scale (value chosen according to *Schlichting et* *al.*, 1993), there is a set couples T and E_d that satisfy the relation. These couples can be (38 K, 110 meV), (90 K, 270 meV) and (140 K, 415 meV). The temperatures have been chosen as reasonably linked to the thermal annealing: in fact, 38 K represents the beginning of the irreversal change in the morphology (*Jennikens et al.*, 1995), 90 K is the boundary temperature required to grown compact ice (*Kimmel et al.*, 2001) and 140 K is the extreme temperature before crystallization (*Smith et al.*, 2006). On the other hand, 110 meV, 270 meV and 415 meV represent respectively 2.5%, 6% and 9% of the total energy released during the atomic hydrogen ricombination. It has been evaluated (*Takahashi et al.*, 1999) that 3-5% of H_2 formation energy is absorbed by the ice. Therefore, according to considerations about the annealing due to the local heating, we can predict that not all the reactions are able to change the ice morphology because the energy transmitted to the surface (3-5%) is not that well above the energy barrier of the diffusion of water (2-9%).

We try now to estimate which is the probability of destroying adsorption sites in the ice per each atomic recombination. It has already been evaluated (Fig.4.3.3) that the dose required to decrease the porosity by 64% of one layer of p-ASW is the fluence $\varphi_0 = 2.2 \times 10^{16}\ D - atoms/cm^2$ per H_2O ML. However, the recombination efficiency is not unity for a porous ASW: it has been found to be ~ 0.3 by *Hornekaer et al.* (2005) and ~ 0.1 by *Manicó et al.* (2001). So, if we assume the atom recombination efficiency to be $R = 0.2$, the number of reactions needed to decrease the porosity by 64% is thus $\varphi_0 \times R/2 = 2.2 \times 10^{15}\ reactions/cm^2/H_2O\ ML$ (the factor 2 is required because 2 atoms form 1 molecule).

The complex geometry of the ice film (that contains tunnels and pores) leads to a large variety of adsorption sites, namely to a wide energy distribution. *Amiaud et al.* (2006), studying the adsorption of D_2 on 10 ML of porous ice, estimated 3×10^{15} (3 ML) the number of adsorbing sites on 10^{16} (10 ML) total H_2O molecules. According to this result, the number of adsorbing sites in our icy sample is $\sim 0.3 \times 10^{15}$ per H_2O ML.

Therefore, taking into account both the density of adsorption sites per ML of ice and the number of atomic recombination responsible for the compaction of the ice, we can conclude that only one reaction over 7 contributes to the re-arrangement of the ice structure because i) not all the reactions provide enough energy; ii) not all the adsorption sites can be easily re-arranged; iii) the energy can be spread along more than one water molecule, even other coadsorbate molecules.

4.6 Astrophysical implication

Finally, we want to estimate the time necessary to obtain the effects observed in laboratory in interstellar dense clouds. Actually, we want to know whether or not the decrease of the ice porosity after the above discussed hydrogen exposure is astrophysically relevant.
The ice mantles in dark clouds are believed to be 40-100 molecular layers thick (*Pontoppidan et al.*, 2003). There are already arguments to say that the ice cannot be fully porous. For instance, in the next Chapter of this thesis,we will show that the morphology of the water formed through the pathway $D + O_2$ on an interstellar ice analogue is compact in structure. This result is also confirmed by a recent article (*Oba et al.*, 2009), even if our experiments are performed in conditions that are more relevant to astrophysical scenarios. By the present study, we can say that if the growth of the water ice is 1/14 lower than the H accretion, then, the water layer porosity is reduced as fast as the mantle grows. This should happen if the H flux is 14 times higher than the O flux, which is the case of several interstellar environments, except the densest and coldest one where, on the contrary, O is the most abundant specie in atomic form (for instance, *Caselli et al.* (2002) have estimated the ratio H/O $\sim 1/7$ for a cloud density of $10^5\ cm^{-3}$). The flux of hydrogen atoms impinging on dust grains for an interstellar cloud can be calculated as follows:

$$\Phi_H = \frac{1}{4} n_H v_H \tag{4.6.1}$$

where n_H is the HI density in gas phase and $v_H = (\sqrt{8kT/\pi m}$ is the mean velocity of an hydrogen atom.
In particular, considering the physical parameters of a dark cloud, $n_H = 2.3\ cm^{-3}$ (*Li & Goldsmith*, 2003) and T = 10 K. Thus, the estimated flux for a molecular cloud is $8.35 \times 10^{11} atoms/cm^2\ yr$.

Fig.4.6.1 shows the reduction of the ice porosity with the time, under different initial thickness of the porous ice. We can notice that, in the case of 1 ML or even 10 ML, the ice compaction arises in times reasonably short

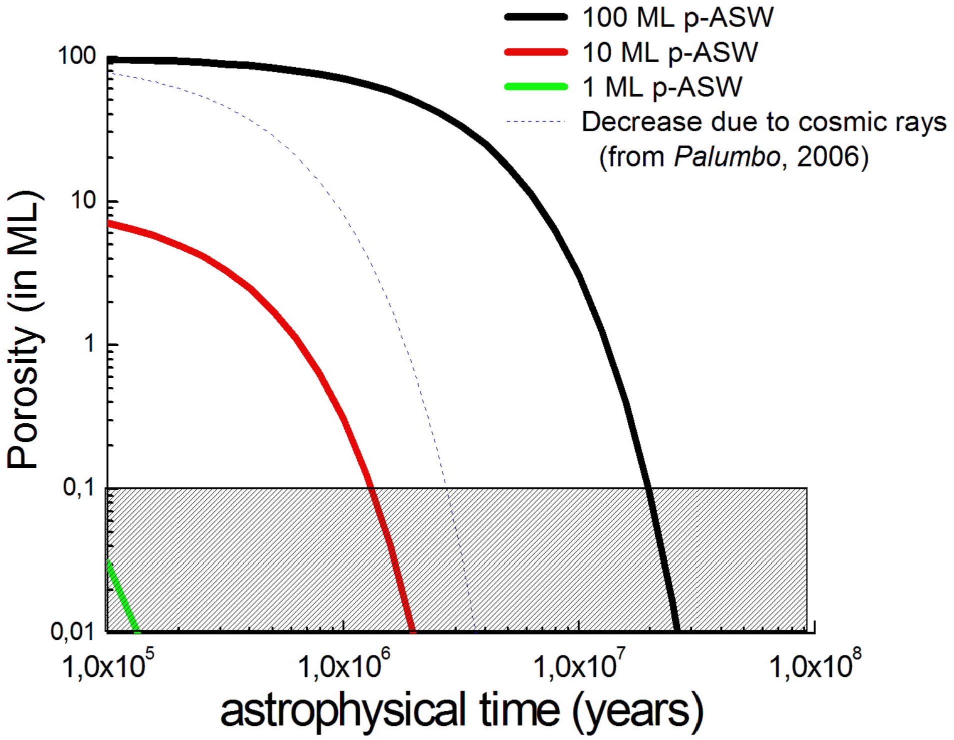

Figure 4.6.1: Estimates of the time needed to change the interstellar ice porosity as a function of the initial thickness of the porous ice.

with respect to the typical range of molecular cloud lifetimes as reported by *Greenberg* (1982) (3×10^7 - 5×10^8 years). For thickest ices, the time of compaction is about 2×10^7 years.
Fig.4.6.1 shows also the compaction of a porous ice after interactions with cosmic rays, as experimentally studied by *Palumbo* (2006). Of course, as the penetration of the cosmic rays is large compared to typical interstellar ice thickness, her result is independent of ice thickness. However, we can see that, if the initial thickness is not higher than a few tens of ML, the compaction of ice due to atomic hydrogen exposure is more efficient than that due to the interaction with cosmic rays, which remains a rather rare process.
As a conclusion, we can say that, in the ISM where O is lacking in comparison to H, the compaction of ice as consequence of H-atoms recombination should be a very efficient process, even taking account water formation (whatever is its initial morphology). In case of denser and coldest clouds, the H_2 formation, even though reduced, is still efficient enough to reduce drastically the porosity of the ice. It seems therefore that, whatever is the medium where ice is formed and stay, the compaction by H atoms should be an efficient process.

4.7 Alternative analysis of the experimental data

In this section, we will present a new model, developed by Dr. Giulio Manicó, to fit the experimental data. This model is semianalytical and assumes more realistically that a film of ASW has a discrete distribution of binding sites on its surface. The hydrogen recombination occurring on the surface as consequence of D-atoms exposure might destroy preferentially the most energetic sites, thereby changing the total distribution of binding sites. At the moment, this model has been successfully tested only on 1 ML p-ASW. Although the model discussed in the previous section works rather well, the alternative model that we will describe hereafter seems to be more intuitive and realistic from the physical point of view. In any case, as we will see, the results obtained with both models are not very different.

4.7.1 Theoretical bases of the new model

In chapter 3, we briefly discussed how it is possible to fit TPD spectra using the Polanyi-Wigner law. We have also shown the different shapes of the spectra according to the order of desorption, namely the zeroth, the first and finally the second order desorption. In all of these simulations, it has been assumed that atoms or molecules are bound to the substrate with a given unique binding energy. Actually, what usually we see in experiments (like the ones we performed) is a substrate with a distribution of sites with different binding energies; spectra are therefore broader than the theoretical ones.

It is reasonable to think that molecular hydrogen colliding with the surface of an icy sample accomodates on adsorbing sites of different energies. Let's assume n the number of different kind of sites with different depths. Let it be E_i the binding energy of a hydrogen molecule on the i-th site of this distribution of sites. If ϑ_i is the number of sites with energy E_i which are populated, then desorption from these sites occurs according to the Polanyi-Wigner law:

$$r_i = -\frac{d\vartheta_i}{dt} = A\,\vartheta_i\,e^{-E_i/T} \tag{4.7.1}$$

where A is the oscillation frequency of the adsorbed molecule in the potential well and r_i is the desorption rate, equal to the rate of decrease of ϑ_i. During each TPD experiment, the sample temperature is increased linearly according to the law:

$$T = T_0 + \beta t \tag{4.7.2}$$

where T_0 is the sample temperature during exposure ($T_0 = 10K$) while β represents the heating rate, equal to 10 K/min in our experiment.
The aforesaid relation between temperature and time allows us to solve analytically the first order differential equation 4.7.1.

$$\frac{d\vartheta_i}{\vartheta_i} = -A\,e^{-E_i/T}\,dt = -\frac{A}{\beta}\,e^{-E_i/T}\,dT \tag{4.7.3}$$

by integrating we get:

$$ln\frac{\vartheta_i}{\vartheta_{i,0}} = -\frac{A}{\beta}\int_{T_0}^{T} e^{-E_i/T}\,dT \tag{4.7.4}$$

i.e.:

$$\vartheta_i = \vartheta_{i,0}\, e^{-\frac{A}{\beta}\,\mathcal{F}(T,E)} \tag{4.7.5}$$

where $\mathcal{F}(T,E) = \int_{T_0}^{T} e^{-E_i/T}\, dT$.
Substituting the obtained solution in equation 4.7.1, we obtain:

$$r_i = A\, e^{-E_i/T}\, \vartheta_{i,0}\, e^{-\frac{A}{\beta}\,\mathcal{F}(T,E)} \tag{4.7.6}$$

i.e.:

$$r_i = A\, \vartheta_{1,0}\, e^{-\frac{A}{\beta}\,\mathcal{F}(T,E)-\frac{E_i}{T}} \tag{4.7.7}$$

The overall desorption rate from our icy sample is given by the sum over all the distribution of sites:

$$R_d = \sum_{i=1}^{n} r_i = A \sum_{i=1}^{n} \vartheta_{i,0}\, e^{-\frac{A}{\beta}\,\mathcal{F}(T,E_i)-\frac{E_i}{T}} \tag{4.7.8}$$

If we define:

$$\varepsilon_i(T) = e^{-\frac{A}{\beta}\,\mathcal{F}(T,E_i)-\frac{E_i}{T}} \tag{4.7.9}$$

and we put:

$$x_i = \vartheta_{i,0} \tag{4.7.10}$$

we obtain:

$$R_d = A \sum_{i=1}^{n} x_i\, \varepsilon_i(T) \tag{4.7.11}$$

In order to fit our experimental data with equation 4.7.11, we will use the *least squares method*. Let us define:

$$\lambda = \sum_j \left[R_d(T_j) - y_j\right]^2 = \sum_j \left[A \sum_i x_i\, \varepsilon_i(T_j) - y_j\right]^2 \tag{4.7.12}$$

where the y_i-s represent the measured desorption rates at the temperature T_i.
Let's now minimize λ by finding the roots of the partial derivatives calculated

respect to the populations x_i:

$$\frac{\partial \lambda}{\partial x_k} = 0 \tag{4.7.13}$$

$$\frac{\partial \lambda}{\partial x_k} = \sum_j \; 2[A \sum_i \; x_i \, \varepsilon_i(T_j) - y_j] \; \varepsilon_k(T_j) = 0 \tag{4.7.14}$$

$$\sum_j \varepsilon_k(T_j) \, [A \sum_i \; x_i \, \varepsilon_i(T_j) - y_j] = 0 \quad , \quad k = 1, ..., n \tag{4.7.15}$$

Let's put $\varepsilon_{ij} \equiv \varepsilon_i(T_j)$ for short. We then have:

$$\sum_j \varepsilon_{kj} \left(A \sum_i \; x_i \, \varepsilon_{ij} - y_j \right) = 0 \tag{4.7.16}$$

$$\sum_{i\,j} A \, x_i \, \varepsilon_{ij} \, \varepsilon_{kj} - \sum_j \; y_j \, \varepsilon_{kj} = 0 \tag{4.7.17}$$

$$A \sum_i \; x_i \, \sum_j \varepsilon_{ij} \, \varepsilon_{kj} = \sum_j \; y_j \, \varepsilon_{kj} \tag{4.7.18}$$

Now let's define:

$$B_k = \frac{1}{A} \sum_j^n \; \varepsilon_{kj} \, y_j \tag{4.7.19}$$

$$A_{ki} \; = \sum_j^n \; \varepsilon_{ij} \, \varepsilon_{kj} \tag{4.7.20}$$

Then, we obtain:

$$\sum_i^n A_{ki} \, x_i = B_k \qquad k = 1, .., n \qquad \Rightarrow \qquad \mathbf{A} \cdot \mathbf{x} = \mathbf{B} \tag{4.7.21}$$

namely a system of linear algebraical equations.

4.7.2 Results obtained with the new model

By solving the system of equations 4.7.21, we obtained the populations of the sites at any binding energy. The model assumes we know what are the energies of the site distribution. In order to find the best distribution, we have to choose, first of all, an interval of binding energies large enough to include all the possible sites. If we exceed in the choice of the interval, we will have, for sites with too small or too large energy, a zero population as a result of the fit. For the choice of the number of sites with different energies, we will assume a constant step in energy between a site and another, and we fit on the value of this step. Our best fit gives an energy step of 24 K ($\sim$ 2.2 meV).

First of all, we will focus on the experimental TPDs related to D_2 desorption from 1 ML of p-ASW after D-atoms exposure (see Fig. 4.2.1a). As already stressed, these spectra show a shift towards lower temperatures and this suggests that D-atoms exposure changes the morphology of the ice. Actually, we think that the porous structure of the ice is gradually changed because of the atomic recombination of hydrogen: the energy released to the sample upon this esoenergetic reaction is large enough to 'destroy' the site where recombination occurred. This effect could be intesified during the TPDs, because the increase of temperature can increase the mobility of D-atoms on the icy surface.
Our results confirm a change in the population of the sites distribution for the icy sample as consequence of D-atoms exposure.

Fig.4.7.1 shows the result of the best fit procedure and the experimental points relative to thermal D_2 desorption from the sample not yet exposed to D-atoms flux. On the contrary, Fig.4.7.2 shows only the best fits related to the TPD spectra from the icy sample after several D-atoms exposures.

The change in the site distribution due to the exposure to atomic hydrogen is shown in Fig.4.7.3. As it can be seen, lower energy sites become more populated with increasing irradiation. Actually, Fig.4.7.4 emphasizes the difference between the populations of adsorption sites of the sample before (0 min) and after the exposure to atomic hydrogen (224 min): adsorption sites with energy lower than 500 K (i.e. 45 meV) are more populated in the case of samples exposed to 224 min of D-atoms exposure.

Now we can ask whether, after exposure to atomic hydrogen, the sticking of D_2 on 1 ML porous ice changes, because some sites are destroyed and

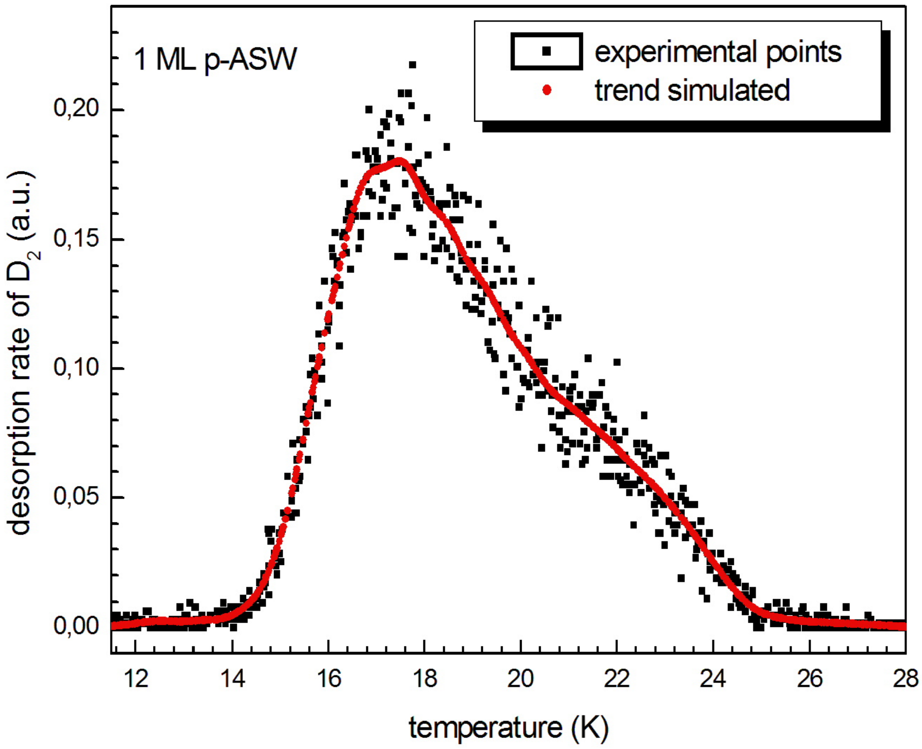

Figure 4.7.1: Thermal D_2 desorption from 1 ML of porous ice, before D-atoms exposure. Experimental data (black points) are fitted through the method of least squares, as the red curve emphasizes (see text for more details).

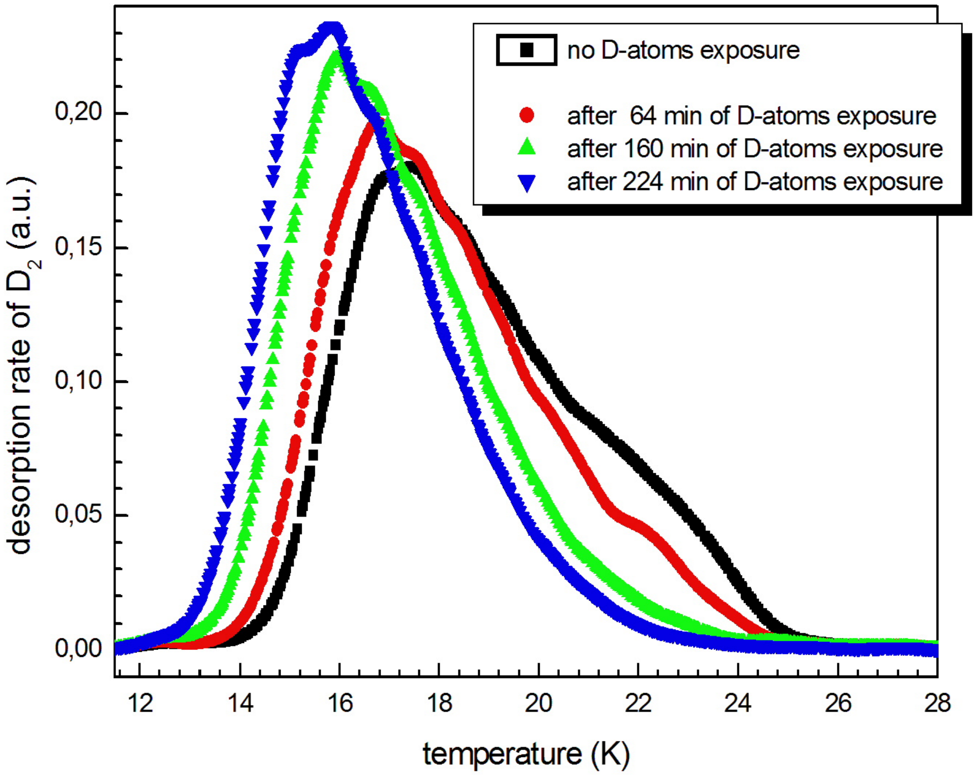

Figure 4.7.2: Thermal D_2 desorption from 1 ML of porous ice, before and after the D-atoms exposure. Experimental points are not shown here, but just their best fits.

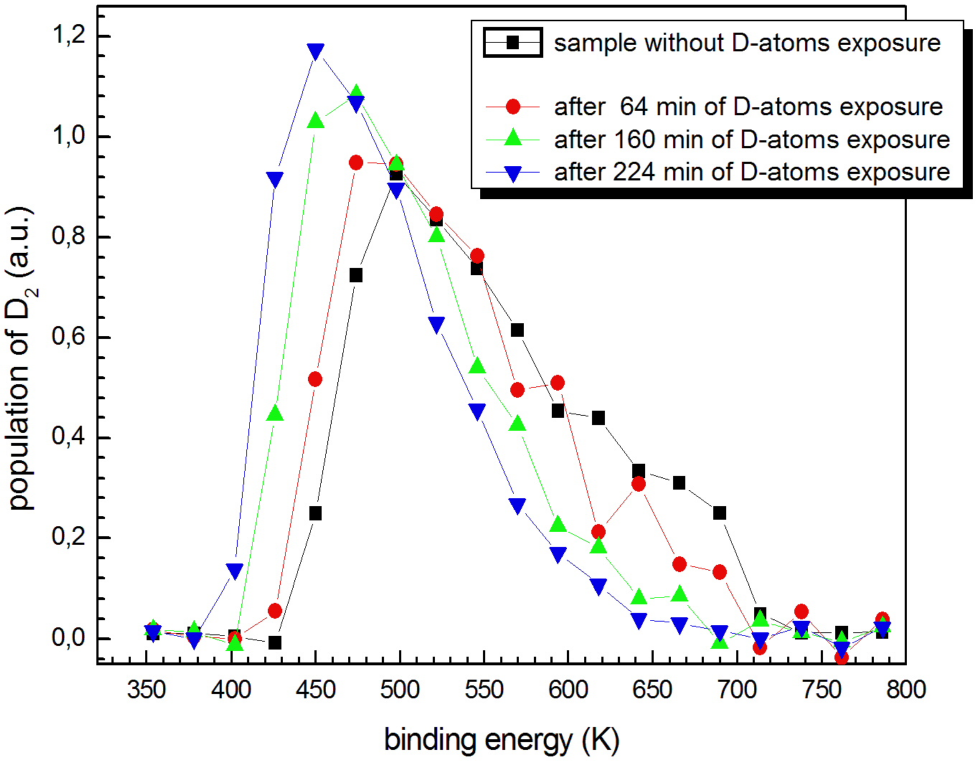

Figure 4.7.3: Distribution of adsorption sites for a porous ASW ice, before and after atomic hydrogen exposure. Sites are progressively destroyed as consequence of D-atoms exposure, stressing the gradual compaction of the sample.

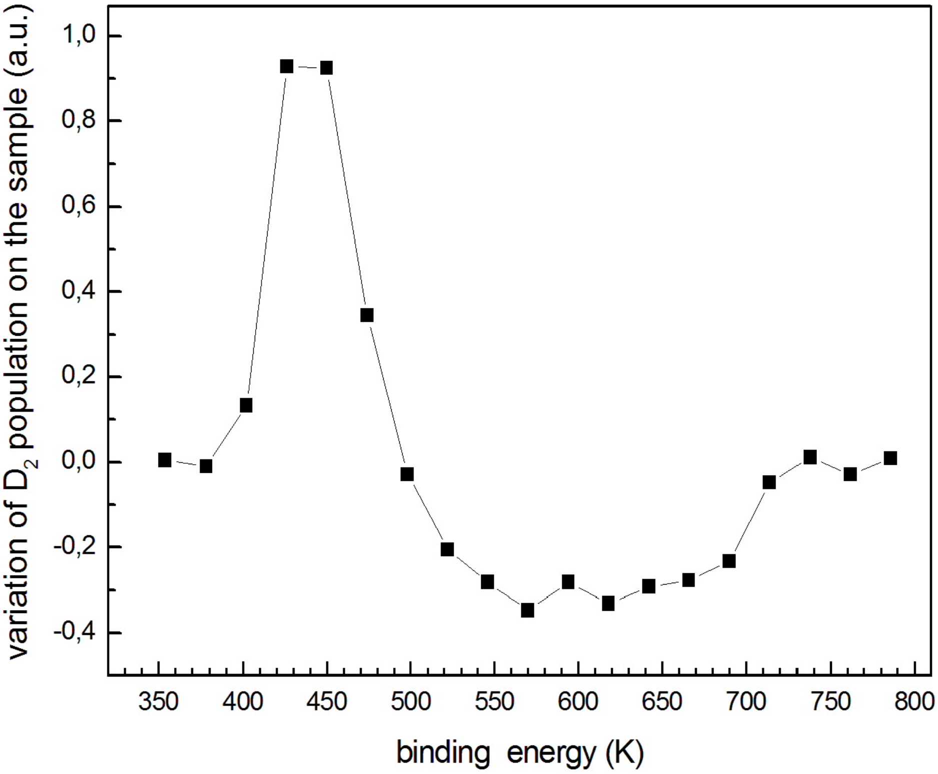

Figure 4.7.4: The difference between the populations of adorption sites in the sample before (0 min) and after the exposure with atomic hydrogen (224 min).

molecules hitting the place where there are no potential wells return to the gas phase. In order to check this possibility, we plot, for each time interval of hydrogen exposure, the sum of the differences in population (for every step of energy) with respect to the population without irradiation. If the same amount of molecules is adsorbed onto the sample, according to the new distribution of sites, we theoretically should obtain a value close to zero in this plot. Indeed a slight decreasing is observed with more and more times of D-atoms exposure (Fig.4.7.5). Therefore, neglecting the small decrease and assuming that at each TPD roughly the same amount of molecules desorbs from the sample, we can estimate the number of binding sites destroyed by atomic hydrogen exposure. In practice, it is necessary to compare the distribution of D_2 population in the icy sample before and after the hydrogen atoms exposure. Results of this analysis are showed in Fig.4.7.6. Now, we can evaluate the number of sites destroyed per H_2 molecule formed. The flux of the D_2 beam, used as a probe, is 9×10^{12} molecules per square centimeter per second. Exposing the sample to the beam for 30 s and assuming a sticking coefficient of 0.7 for porous ice, we obtain that the total amount of D_2 molecules adsorbed during each experiment is about 1.7×10^{14} molecules per cm^2.

During the D-atoms exposure, the flux reaching the sample is $\sim 1.2 \times 10^{13}$ atoms per cm^2 per second. Assuming, for a porous ice, a sticking coefficient of 0.7, during one minute of exposure the number of D-atoms which sticks to the sample is about 5.04×10^{14} per cm^2.

In order to obtain the total number of molecules formed on the sample surface, we have to consider the recombination efficiency: we will assume $\eta = 0.2$, namely an average value between the experimental results obtained by *Manicò et al.* (2001) and by *Hornekaer et al.* (2003). Actually, only a fraction of this total is involved in the annihilation of the sites with higher binding energy. We have estimated this fraction as follows. We assume that the number of D-atoms which stick on the surface goes into sites of different energy according to the distribution we obtained when no irradiation with D-atoms occurs. As we have evaluated the number of sites destroyed as consequence of D_2 formation, taking into account only the tail on the right of the distribution (i.e. the part of the distribution which decreases upon irradiation), we should consider now only D-atoms which are adsorbed on these sites. From this fraction of atoms, we obtain the fraction of molecules formed which could destroy the adsorption site by using the recombination efficiency.

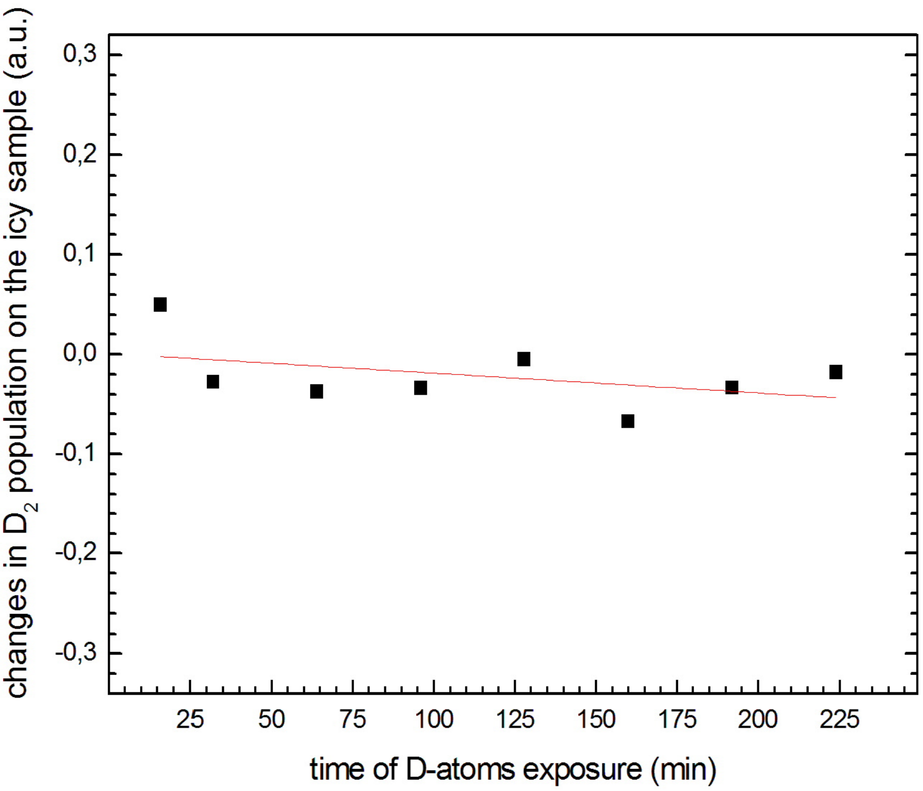

Figure 4.7.5: Black points represent the sum of the differences in population (for every step in energy) with respect to the site population before any irradiation, as a function of the time duration of D-atoms exposure. The very small slope of the red line implies that the sticking coefficient of D_2 remains almost costant during all the experiment.

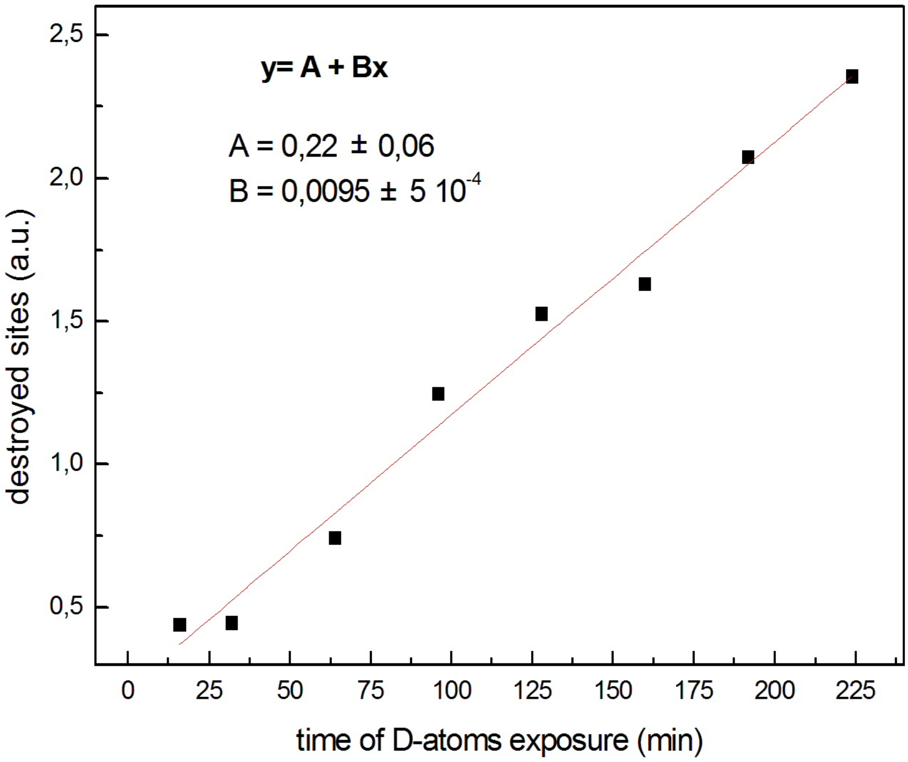

Figure 4.7.6: Destroyed sites versus irradiation time.

Our calculations give a fraction of 0.08. In the light of latest considerations, we can re-plot Fig.4.7.6: the new fit is shown in Fig.4.7.7. Approximately there is a site destroyed every 13 molecules formed.

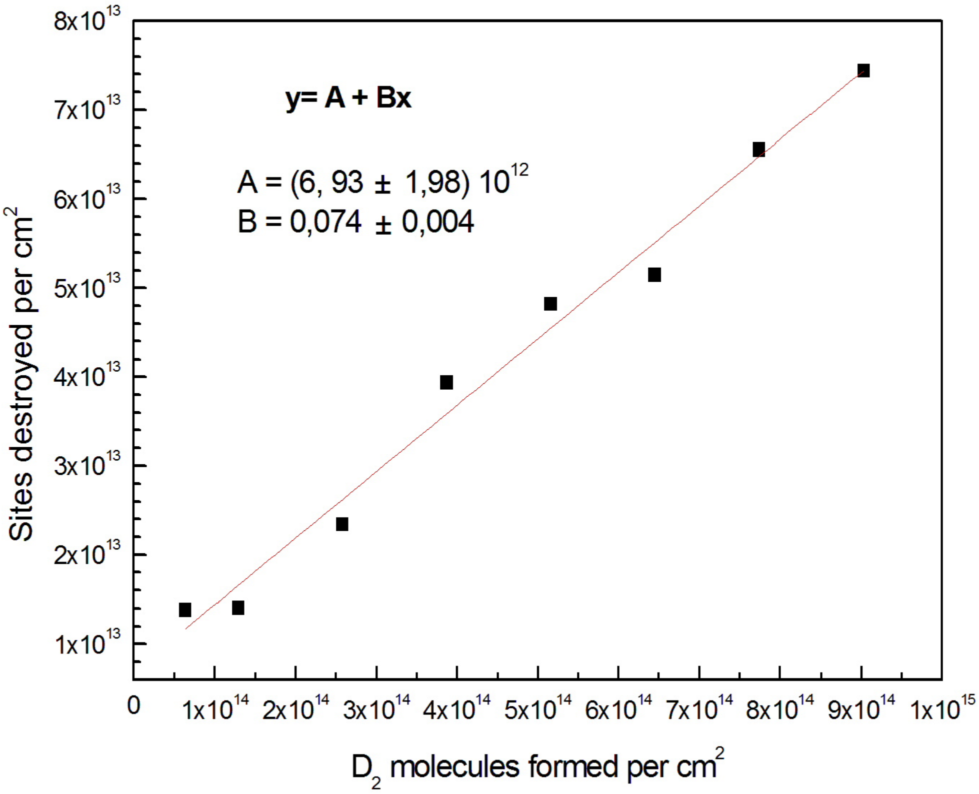

Figure 4.7.7: Number of sites destroyed per each molecule formed.

4.7.3 Estimation of molecules formed during the TPD

We have developed also a model to estimate the hydrogen recombination during the heating process in a TPD experiment, taking into account mobility of H-atoms on the sample and destruction of sites upon H_2 formation.

Assuming N_i the number of H-atoms on the sample with binding energy equal to E_i, the probability of desorption for each hydrogen atom will be:

$$e^{-E_i/T} \tag{4.7.22}$$

Otherwise, the adsorbed atom can diffuse on the sample (forming H_2 if the new site is already occupied) with probability:

$$e^{-D_i/T} \tag{4.7.23}$$

where D_i is the energetic barrier which the atom has to overcome to diffuse. Let's define ν the number of attempts in a time unit to overcome the barrier for desorption (E_i) or diffusion (D_i). Hence, multiplying ν by the probability of desorption or diffusion, we will obtain the rate of desorption or diffusion per single atom. A value of ν largely adopted in literature is 10^{12} - 10^{13} s^{-1} (*Hasegawa et al.*, 1992). Following *Katz et al.* (1999), we will assume $\nu = 10^{12}\ s^{-1}$.
Finally, let's call N_T as the total number of sites on the sample, and $N_{i,tot}$ the total number of sites with energy E_i on the sample.
Now, taking into account all the possibility for the atomic hydrogen adsorbed, we can write the rate of change of N_i, namely the number of atoms adsorbed on sites with binding energy E_i as follows:

$$\begin{aligned}\frac{dN_i}{dt} &= -\nu\, e^{-E_i/T(t)}\, N_i - \nu\, e^{-D_i/T(t)}\, \frac{N_i}{N_T}\, N_i \\ &\quad -\nu\, e^{-D_i/T(t)}\, N_i \sum_{j\neq i} \frac{N_j}{N_T} - \nu\, \frac{N_i}{N_T} \sum_{j\neq i} e^{-D_j/T(t)}\, N_j \\ &\quad -\nu\, e^{-D_i/T(t)}\, N_i \sum_{j\neq i} \frac{N_{j,tot} - N_j}{N_T} \\ &\quad +\nu\, \frac{N_{i,tot} - N_i}{N_T} \sum_{j\neq i} e^{-D_j/T(t)}\, N_j \end{aligned} \tag{4.7.24}$$

where the first term in the right hand side represents the desorption of the atomic hydrogen from the sample; the second term represents the migration of H-atoms to another site with the same binding energy (i.e. E_i), already occupied, with formation of H_2; the third term takes into account the loss of hydrogen atoms which migrate to sites with different binding energy (E_j), already occupied, thereby forming H_2; the fourth term takes into account the loss of atomic hydrogen because of its recombination with atoms coming from sites with different binding energy (E_j); the fifth term takes into account migration of H-atoms toward empty sites with different binding energy; and, finally, the last term represents all H-atoms coming from sites with different binding energy.
Rearranging the terms, the rate of N_i can be re-written:

$$\begin{aligned}\frac{dN_i}{dt} &= -\nu\, e^{-E_i/T(t)}\, N_i - \nu\, e^{-D_i/T(t)}\, \frac{N_i}{N_T}\, N_i \\ &\quad -\nu\, e^{-D_i/T(t)}\, N_i \sum_{j\neq i} \frac{N_{j,tot}}{N_T} \\ &\quad +\nu\, \frac{N_{i,tot} - 2N_i}{N_T} \sum_{j\neq i} e^{-D_j/T(t)}\, N_j \end{aligned} \tag{4.7.25}$$

$$\begin{aligned}\frac{dN_i}{dt} &= -\nu\, e^{-E_i/T(t)}\, N_i - \nu\, e^{-D_i/T(t)}\, \frac{N_i}{N_T}\, N_i \\ &\quad -\nu\, e^{-D_i/T(t)}\, N_i\, \frac{N_T - N_{i,tot}}{N_T} \\ &\quad +\nu\, \frac{N_{i,tot} - 2N_i}{N_T} \sum_{j\neq i} e^{-D_j/T}(t)\, N_j \end{aligned} \tag{4.7.26}$$

Let's now evaluate the formation of molecular hydrogen on a site with binding energy E_i. Defining $N_{2,i}$ the number of molecule formed, we can evaluate the rate of H_2 formation as follows:

$$\frac{dN_{2,i}}{dt} = \frac{1}{2}\,\nu\, e^{-D_i/T(t)}\, \frac{N_i}{N_T}\, N_i + \nu\, \frac{N_i}{N_T} \sum_{j\neq i} e^{-D_j/T(t)}\, N_j \tag{4.7.27}$$

where the first term in the second hand represents the formation of H_2 due to recombination of two H atoms both adsorbed on sites with binding energy E_i, while the second term takes into account of the formation of H_2 molecules on the site with binding energy E_i due to recombination between an H atom already adsorbed on this site and an H atom diffusing from sites with different binding energy.

Whenever two H-atoms react each other to form H_2, there is a probability that the site where recombination occurred can be destroyed. The rate equations related to the change of $N_{i,tot}$ (namely the total number of sites with binding energy E_i) take into account the destruction of sites where recombination occurs in this way:

$$\frac{dN_{i,tot}}{dt} = -\alpha \frac{dN_{2,i}}{dt} \tag{4.7.28}$$

where α is a coefficient that represents the probability to destroy the site; actually, it is the slope of the straight line which fits data in Fig. 4.7.7. Then $\alpha = 1/13 = 0.074$, because approximately one site is destroyed every 13 molecules formed.

Now we are able to integrate the previous differential equation over the typical time interval of a TPD experiment, i.e. $\sim$ 3 min for the range 10 K - 30 K, considering an heating rate of $\beta = 10$ K/min. There is, indeed, a linear relation between time and temperature: $T = T_0 + \beta t$. The number of total sites with binding energy E_i ($N_{i,tot}$) has been evaluated experimentally, analysing the TPD spectrum related to D_2 desorption from the porous ice before the D-atoms exposure.

We assume that, when two adsorbed D atoms meet together on the surface and recombine, the just formed D_2 molecule must spend some of the excess energy to desorb. For this reason, we don't need to know exactly what is the binding energy of D_2 on the surface. Anyway, we can affirm that the distribution of adsorption sites of D_2 is likely obtained by multiplying the energy distribution for D atoms by a constant factor. As we are interested to the binding sites where D atoms recombine to form D_2, for the sake of simplicity we will identify (label) them by using the binding energy of D atoms instead of that of D_2 molecules.

About the barrier of diffusion D_i, we made the typical assumption e largely used in literature, i.e. $D_i = 0.5 \times E_i$, e.

Fig.4.7.8 shows the results of our simulation: for each site of H-atoms adorption (black points), it is reported the efficiency of H_2 formation (red points).

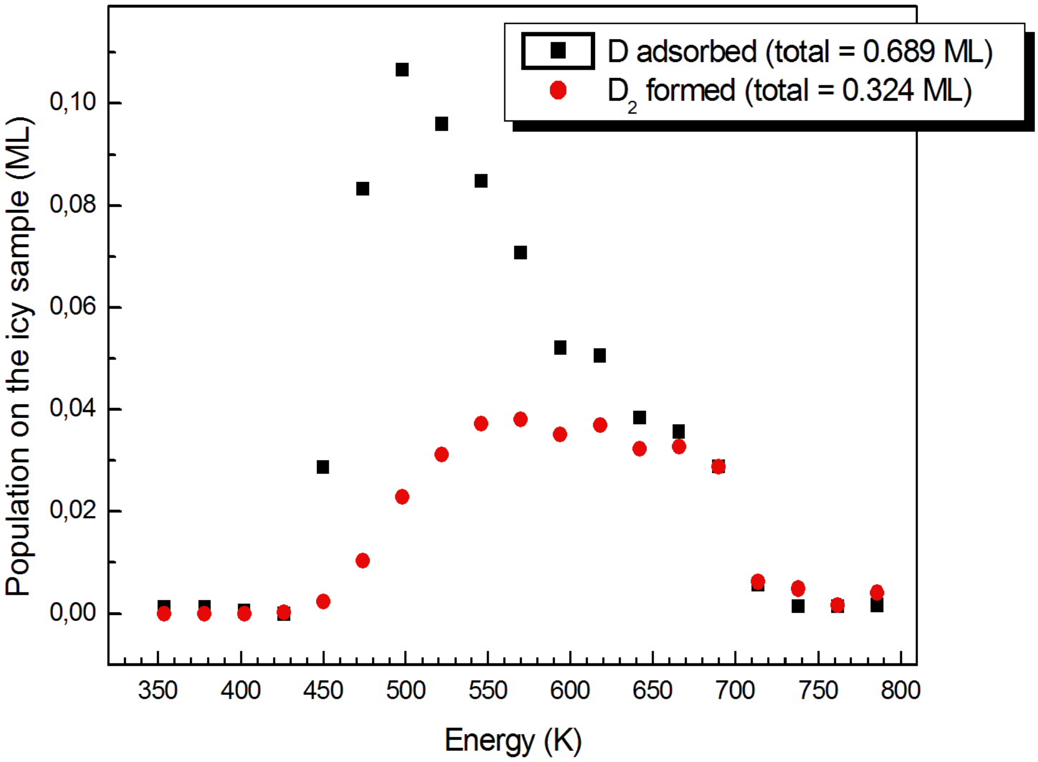

Figure 4.7.8: Rate of H_2 formation in each site of H-atoms adsorption.

Chapter 5

Morphology of just formed water

5.1 Models of H_2O formation

Water has been detected, in gaseous or solid form, in numerous astrophysical environments (such as planets, comets, interstellar clouds and star forming regions). In dark interstellar clouds, it is possible to detect the amorphous solid water through the infrared adsorption feature at 3.07 μm (*Leger et al.*, 1979).

What are the most efficient mechanisms for the water formation is still only partially understood. From the theoretical point of view, different pathways for water formation in the ISM were proposed some years ago by *Tielens & Hagen* (1982). They suggested that H_2O formation would be initiated by H-atoms reacting with O, O_2 and O_3. According to current belief (see e.g. *Ceccarelli et al.*, 2007), water formation in the gas phase is not efficient enough to reproduce the observed abundances. Therefore, water molecules must be synthesized largely by surface reactions on the cold interstellar grains.

The possible processes for H_2O formation occurring on the surface of interstellar grains are:

1. Sequential hydrogenation of O-atoms:

$O + H \rightarrow OH$

$OH + H \rightarrow H_2O$

2. Reactions between OH and H_2:

   $OH + H_2 \rightarrow H_2O + H$

3. Reactions involving O_2 molecules:

   $O_2 + H \rightarrow HO_2$

   $HO_2 + H \rightarrow H_2O_2$

   $H_2O_2 + H \rightarrow H_2O + OH$

4. Reactions involving O_3 molecules:

   $O_3 + H \rightarrow OH + O_2$

   $OH + H \rightarrow H_2O$

   $O_2 + H \rightarrow HO_2$

   $HO_2 + H \rightarrow H_2O_2$

   $H_2O_2 + H \rightarrow H_2O + OH$

5.2 Previous experiments about H_2O formation

Recently, some of the aforesaid reactions have been investigated experimentally. *Miyauchi et al.* (2008) have experimentally analysed the reaction between cold H-atoms and O_2 ice at 10 K: they observed by in situ infrared spectroscopy the formation of H_2O_2 and H_2O molecules and estimated the efficiency of the reaction scheme. *Ioppolo et al.* (2008) performed just after a similar experiment, but also varying the temperature of O_2 substrate: the production of $\mathrm{H_2O_2}$ and $\mathrm{H_2O}$ was confirmed, adding also an estimate of the

reactions upon the temperature dependence.
In a still unpublished work, *Dulieu et al.* (2010) investigated the formation of water molecules via hydrogen and oxygen atoms interacting at 10 K on a realistic surface analogue of grains in dense molecular clouds, i.e. on a film of amorphous water ice. They found a rather high efficiency of water formation (~ 0.5), thereby concluding that $O + H$ could be the most efficient water formation pathway in the boundary layers of dense clouds where UV photons and atomic species dominate.
Cuppen & Herbst (2007), using a Monte Carlo approach, conjectured that under dense cloud conditions the $O_3 + H$ pathway is the most efficient route leading to the formation of H_2O. Actually, in a very recent experimental work [1] (*Mokrane et al.*, 2009), we confirmed that water can be synthetized efficiently on the surface of realistic analogs of interstellar ice via ozone hydrogenation. Moreover, it has been shown that this reaction exhibits no activation barrier at 10 K, thereby corroborating that ozone is a likely precursor to water formation on a water ice layer at 10 K.
Finally, *Oba et al.* (2009) have investigated the formation both of H_2O and of H_2O_2 by co-deposition of H-atoms and O_2 molecules. Through the infrared analysis in situ, they found that just formed water ice in their experiments is amorphous: this results consistent with the observation of H_2O ice in molecular clouds. Furthermore, the lack of dangling OH bonds in the laboratory spectra after codeposition of O_2 and H indicates the lack of microporous structure in the ice formed in this way, suggesting its compact nature.

The experiments described in the present chapter investigate the morphology of the water synthetized through the pathway $D + O_2$. The experiments are performed on realistic grain surface analogues in dense clouds, namely on ASW substrates. Actually, in the dense interstellar environment most of the water molecules should be formed directly above a pre-existing ice layer (typical ice thickness ranges between 40 and 100 molecular layers according to *Pontoppidan et al.*, 2003). Our experiments show that solid water just created has a compact structure.

---

[1] The experiments discussed in *Mokrane et al.* (2009) have been carried out in the set-up FORMOLISM during my stay in Cergy-Pontoise University and I, indeed, participated to its realization.

5.3 The experimental procedure

5.3.1 Controlling the D and O_2 dose

The morphology of the newly synthethized water layer is characterized by studying the thermal desorption of D_2 molecules adsorbed onto the sample (for more details about this technique see the paragraph 3.2.2). For a successful experiment, we need two conditions:

1. Solid O_2 remains isolated on the icy surface (i.e. low coverage regime);
2. All the O_2 is used for the water formation, otherwise the presence of intermediate molecules (such as H_2O_2) might change the properties of D_2 adsorption/desorption;

For this reason, we have studied first the decrease of the O_2 population into the ice as a function of D-atoms fluence. Nevertheless, we want to avoid an excessive D-atoms exposure, that could modify the morphology of the ice substrate, making the interpretation of our experimental data more difficult. For this purpose, a preliminary set of experiments shown in Fig.5.3.1 has been performed. In practice, a non complete layer of O_2 ($\sim$ 0.2 ML) grown over a compact ice is exposed to a dose of D-atoms. After that, increasing the sample temperature till 49 K with a linear ramp, thermal desorption of molecular oxygen is monitored. This procedure is iterated many times, each time after rising the dose of D-atoms. We can notice that the amount of O_2 desorbed decreases with the increase of the D-atoms dose. In particular, the inset in Fig.5.3.1 shows the integrated TPD intensities as a function of D-atoms irradiation: it is emphasized that the amount of O_2 desorbed from the compact ice after D-atoms exposure follows an exponential decay respect to the D-atoms fluence. From the figure, we can see that, after $\sim$ 90 s of D-atoms exposure, the majority of O_2 on the sample is already destroyed. Hereafter we report the sequential reactions occurring on the ice surface when a non-complete layer of O_2 interacts with D-atoms:

$$O_2 \ + \ D \ \rightarrow \ O_2D$$

$$O_2D \ + \ D \ \rightarrow \ D_2O_2$$

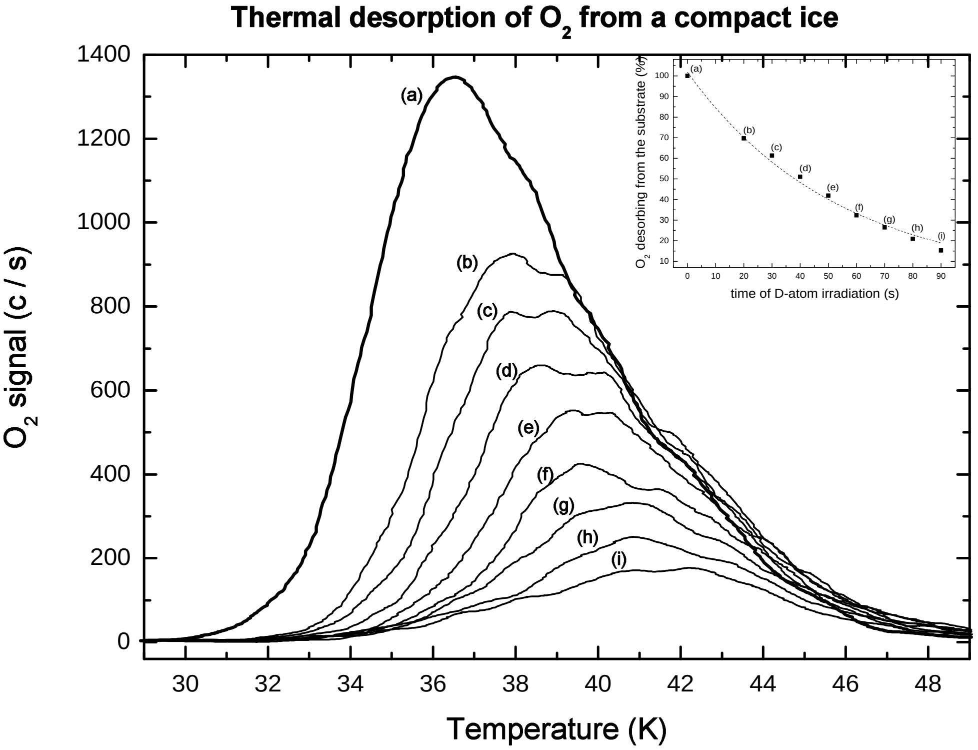

Figure 5.3.1: Thermal desorption of O_2 from a compact ice. O_2 is gradually destroyed following the increase of D-atoms exposure. A film of 0.2 ML of solid O_2 is irradiated with **(a)** 0s, **(b)** 20s, **(c)** 30s, **(d)** 40s, **(e)** 50s, **(f)** 60s, **(g)** 70s, **(h)** 80s and **(i)** 90s of D-atoms.

$$D_2O_2 \; + \; D \; \rightarrow \; D_2O \; + \; OD$$

$$OD \; + \; D \; \rightarrow \; D_2O$$

We have seen that $\sim$ 90 s of D-atoms exposure are necessary to destroy the majority of the molecular oxygen deposited on the ice. As for each oxygen molecule four hydrogen (deuterium) atoms are required in order to form two molecules of water, a dose of deuterium four times greater (i.e $\sim \; 4 \times 90s = 360s$) has to be used: in this way, we are confident that all of O_2 is consumed, by synthetizing only solid water.
We have also made a kinetic model in order to estimate the evolution of species on the icy surface during the D-atoms exposure (Fig.5.3.2). Assuming for a first approximation the same probability for each aforesaid reaction (it means no activation barrier and D-atoms diffusing quickly) and that no molecule desorbs during the hydrogen exposure, we have found that 360 s of D-atoms exposure on 0.2 ML of solid O_2 are able to form an almost pure substrate of water.

5.4 Experiments on a compact ice substrate

Fig.5.4.1 summarizes schematically the experimental procedure used in order to study the morphology of the water formed through the reaction between solid O_2 and D-atoms deposited on the surface of a compact ice substrate.

1. the sample holder is cooled down to 120 K;

2. a film of $\sim$ 100 ML of compact ASW is grown by spraying on the cold surface;

3. the sample holder and the compact film are cooled to 10 K;

4. **the ice substrate is exposed to 1 minute of O_2, corresponding to 0.2 ML of solid molecular oxygen (look to the flux estimation discussed in the Section 3.3.2)**

5. **the sample is then exposed to 6 minutes of D-atoms. Actually, the kinetic model (Fig.5.3.2) guarantees that, with this dose**

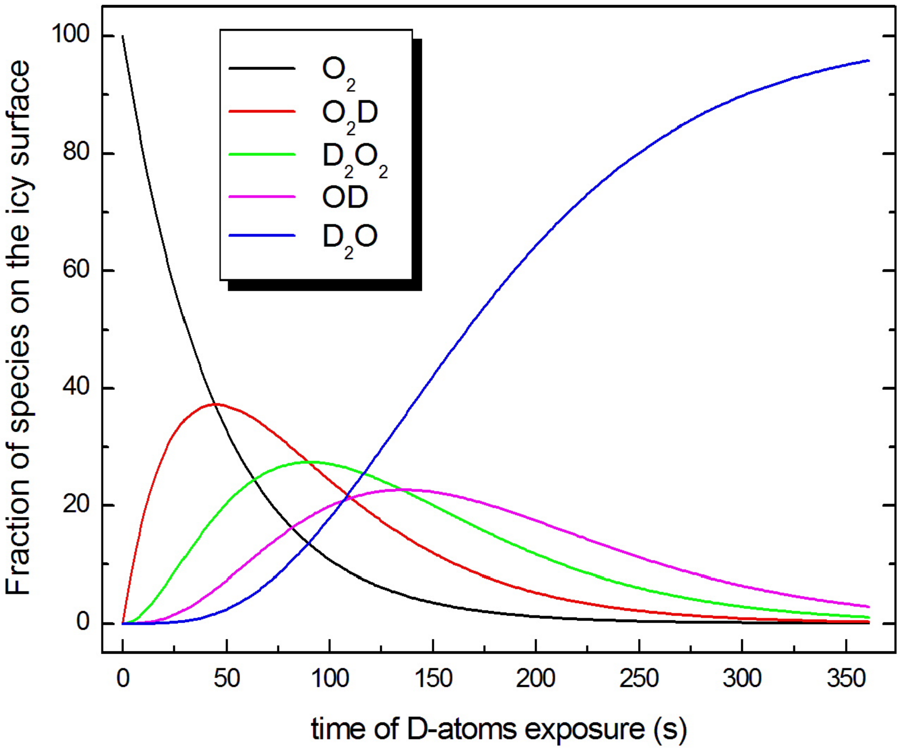

Figure 5.3.2: The present kinetic model show which is the evolution of the species present on the surface during the D-atoms exposure of 0.2 ML of solid O_2. This model assumes equivalent probability of formation and no desorption during the D-atoms exposure (see text for more details).

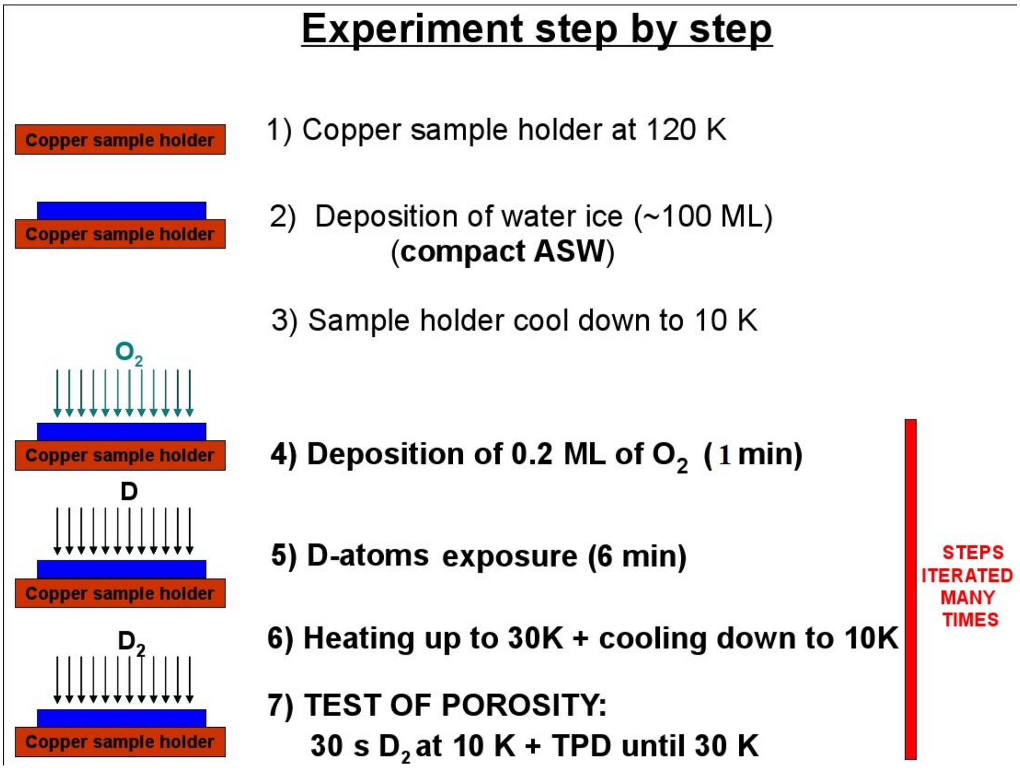

Experiment step by step

1) Copper sample holder at 120 K

2) Deposition of water ice (~100 ML)
(**compact ASW**)

3) Sample holder cool down to 10 K

4) Deposition of 0.2 ML of O_2 (1 min)

5) D-atoms exposure (6 min)

6) Heating up to 30K + cooling down to 10K

7) TEST OF POROSITY:
30 s D_2 at 10 K + TPD until 30 K

STEPS ITERATED MANY TIMES

Figure 5.4.1: Description of the experimental procedure used to study the morphology of the water formed through the pathway $D + O_2$ on a compact ice substrate

of D-atoms, the O_2 is almost entirely locked up in the newly formed water (D_2O);

6. **at the end of each D-atoms exposition, the temperature of the sample is increased to 30 K. In this way, it is completely removed both the molecular deuterium formed into the ice when two atoms of D encounter each another and also D_2 molecules coming as undissociated fraction directly from the source, that does not produce pure D atomic beam. After that, the sample is cooled again to 10 K;**

7. **the porosity of the irradiated sample is checked. In practice, the ice is exposed to 30 s of D_2 flux ($\sim$ 0.15 ML of D_2), then, heating the sample until 30 K with a linear ramp (10 K/min), while the mass spectrometer monitors the thermal desorption of D_2.**

5.4.1 H_2O formed on a compact ice substrate

As already discussed, the study of the desorption kinetics of a small controlled amount of D_2 adsorbed on ASW gives us information about the morphology of the sample (see Paragraph 3.2.2 for more details).
Fig.5.4.2 shows the probing of the morphology of the sample after the D-atoms exposure of 0.4 ML, 0.8 ML, 1.2 ML and 1.6 ML of solid O_2, namely after the formation of respectively 0.8 ML, 1.6 ML, 2.4 ML and 3.2 ML of solid water. Within the experimental uncertainties, the four TPD profiles can be considered identical, and their behaviour emphasizes D_2 desorbing from a compact ice substrate.

The abrupt beginning of D_2 desorption shown in Fig.5.4.2 reflects the malfunctioning of the cryocooler: we were obliged to perform the experiments maintaining the sample at 15 K, instead of 10 K. First experiments performed maintaining the icy substrate at 10 K (but in less controlled conditions of O_2 and D flux) gave similar results: after water formation, no desorption of D_2 occurs above 22 K, thereby giving the "signature" of D_2 desorption from a compact surface. Therefore, even if the experiments discussed have not been carried out in the best condition, nevertheless we can certainly declare that the hydrogenation of solid O_2 produces water ice with a compact structure.

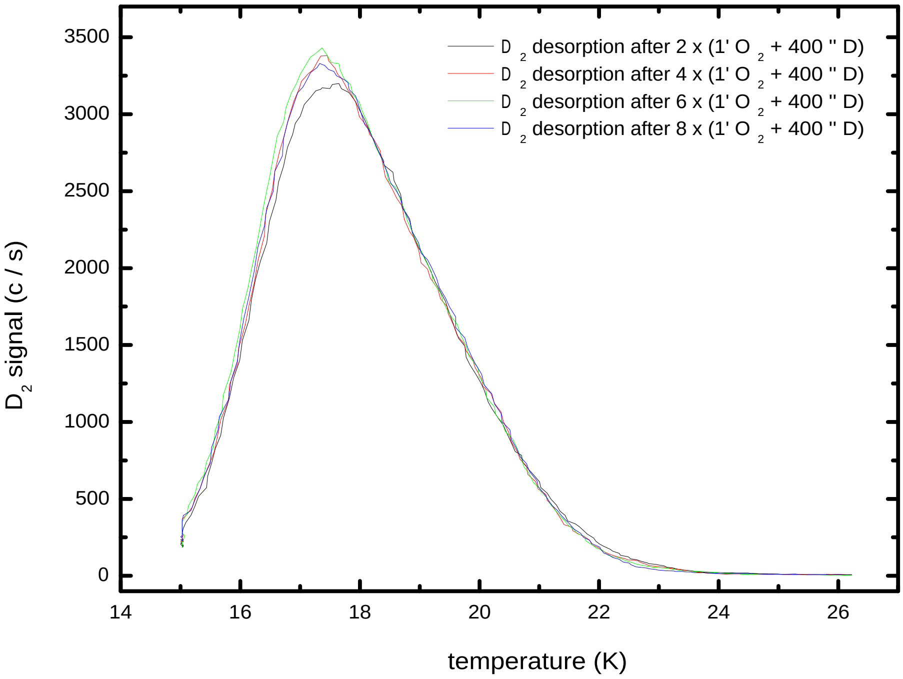

Figure 5.4.2: TPD spectra of 0.15 ML of D_2 from a compact ice substrate, after formation of water via $D + O_2$ pathway.

5.5 Experiments on a porous ice substrate

Fig.5.4.1 summarizes schematically the experimental procedure used in order to study the morphology of the water formed through the reaction between solid O_2 and D-atoms deposited on the surface of a porous ice substrate. The procedure is almost the same used for a compact sample, but in this case the sample (a film of porous ice) is grown over a thick compact ice layer. The thickness chosen (5 ML) is the thinnest that shows 100% of porous ice energy distribution: in fact thicknesses lower than 5 ML show a binding-energy distribution partially due to the compact ice substrate, as it has been emphasized by *Fillion et al.* (2009).

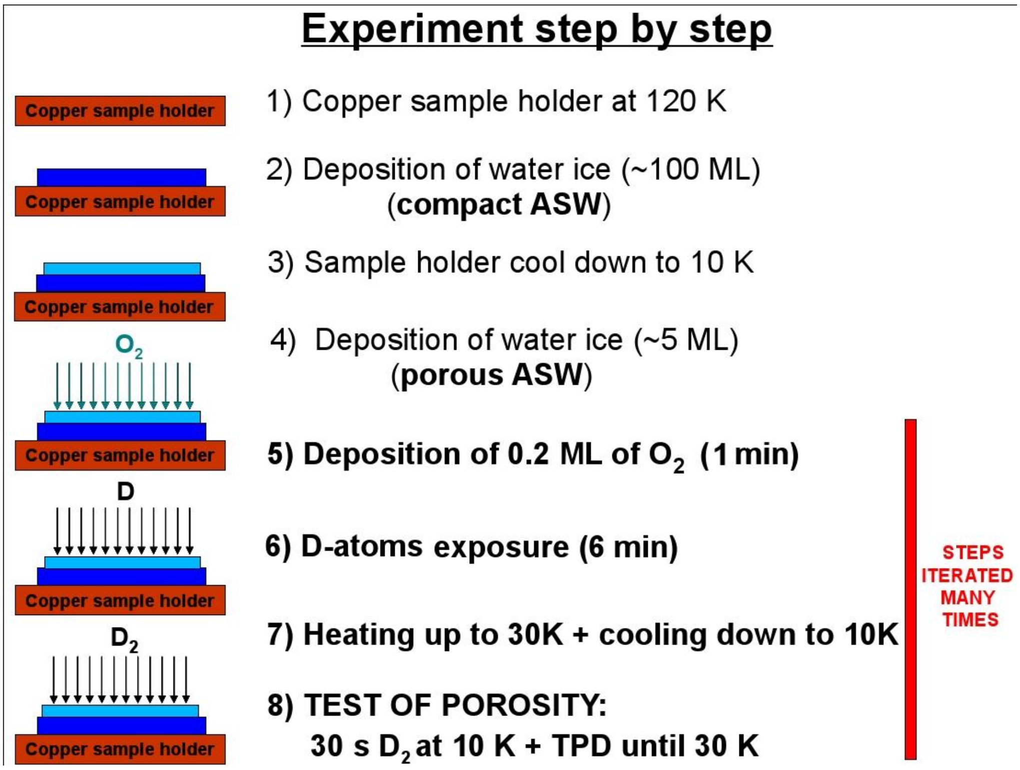

Experiment step by step

1) Copper sample holder at 120 K

2) Deposition of water ice (~100 ML)
(**compact ASW**)

3) Sample holder cool down to 10 K

4) Deposition of water ice (~5 ML)
(**porous ASW**)

5) Deposition of 0.2 ML of O_2 (1 min)

6) D-atoms exposure (6 min)

7) Heating up to 30K + cooling down to 10K

8) TEST OF POROSITY:
30 s D_2 at 10 K + TPD until 30 K

STEPS ITERATED MANY TIMES

Figure 5.5.1: Description of the experimental procedure used to study the morphology of the water formed through the pathway $D + O_2$ on a porous ice film

5.5.1 H_2O formed on a porous ice substrate

Similarly, the morphology of the water formed through the pathway $D + O_2$ in a porous ice has been investigated. Fig.5.5.2 shows the test about the morphology of the sample after the formation of 0.4 ML, 2.0 ML and 4.4 ML of solid water, on an initial 5 ML porous ice substrate grown at 15 K.

A gradual shift towards lower temperatures in the TPD profiles appears as the solid water is progressively formed. Like in Fig.4.2.1 of previous chapter, we have a demonstration that the compaction occurs. Nevertheless, the

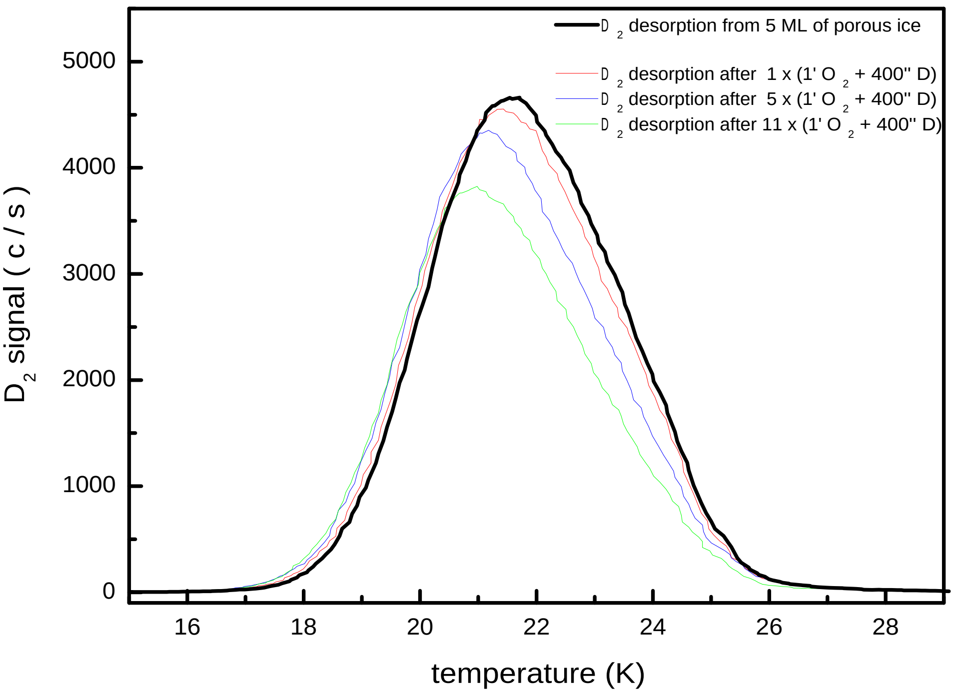

Figure 5.5.2: TPD spectra of 0.15 ML of D_2 from a porous ice substrate, after formation of water via $D + O_2$ pathway. The shift towards lower temperatures in the TPD profiles emphasizes the formation of water with a compact structure.

interpretation of the experimental data is not obvious in this case. Actually, if the progressive compaction of the sample appears evident, it might not be due to the water formation, but only induced by the D_2 recombination occurring at the same time on the surface. In fact, as widely shown in the previous chapter, a similar behaviour has been observed following D-atoms exposure of a porous ice.

Fig.5.5.3 shows the comparison between the two different mechanisms that lead to the gradual compaction of a porous ice sample. The initial thickness of the ice is not exactly the same (5 ML vs 6.5 ML), but the fluence is about the same (74 minutes vs 96 minutes), and we have seen previously that it is the D-atoms fluence per H_2O ML which leads the decrease of the porosity. Comparing the upper figure (water formation) and the bottom figure (pure D-atoms exposure), we can notice that the shape of the TPD profiles changes in a different way. In particular, the compaction of the sample as consequence of the water formation appears clearly more efficient, stressing the likely compact nature of the just formed water. Even in this case, we can analyse the decrease of the ice porosity, with a similar method used in the previous chapter. We see in Fig.5.5.2 that the initial porosity of the ice thick 5ML is reduced about one half after the formation of 4.4 ML of solid water on its surface.

In order to explain our experimental results, we propose here a very simple model: if the new water molecule is formed on a porous site, we can suppose its transformation in a compact ice site, whereas if the new water molecule is formed on a compact site, we can suppose that no change occurs in that site. Moreover, we assume that each H_2O molecule of the porous ice substrate is associated with one adsorption site, and we do not consider the fact that indeed one O_2 molecule produces two water molecules. The full triangles in Fig.5.5.4 represent the decrease of the porosity estimated calculating the area subtended by each TPD curve for temperatures higher than 23 K. On the other hand, the solid black line shows the decrease of more binding sites as evaluated by our model, based upon a random localization of sites for the formation of water. The reduction of the porosity seems slightly less rapid than with a pure statistical model.

Actually, the assumption that each H_2O molecule of the porous ice substrate is associated with one adsorption site is rather rough: a more realistic value seems to be 0.44 sites per H_2O molecule, as evaluated by *Kimmel et al.* (2001) studying N_2 desorption from a porous ice substrate. Therefore, the

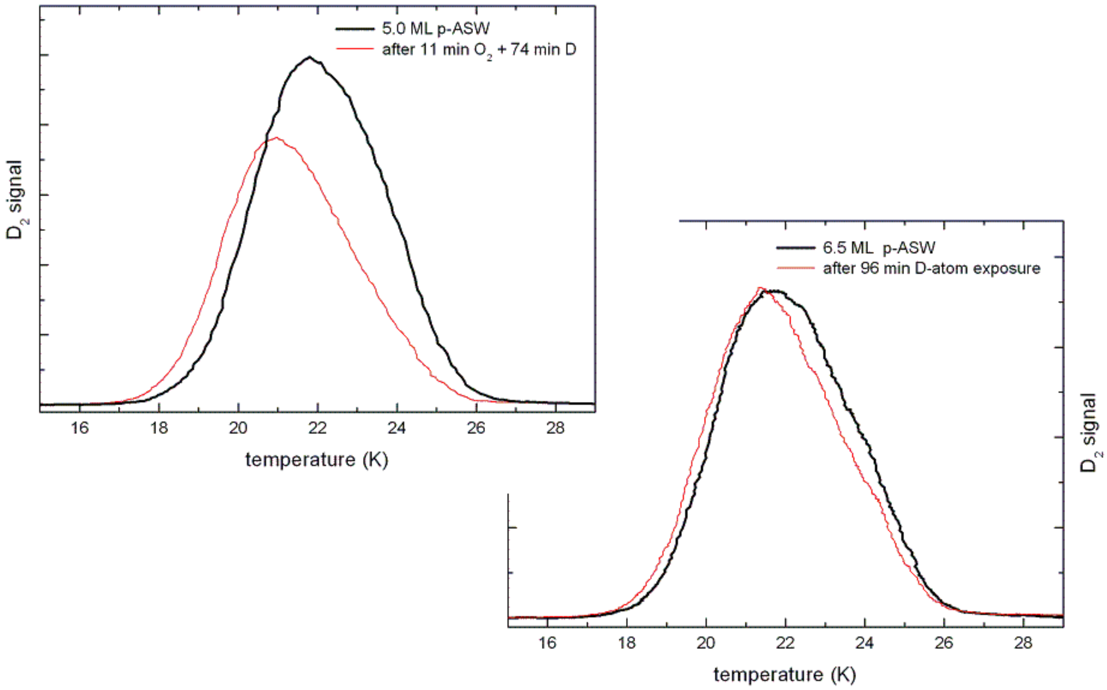

Figure 5.5.3: The two figures show two different mechanisms that lead to the compaction of the sample: the formation of compact ice following D-atoms exposure of solid O_2 upon a porous ice substrate (upper graph) and D-atoms irradiation of a porous ice sample (lower graph)

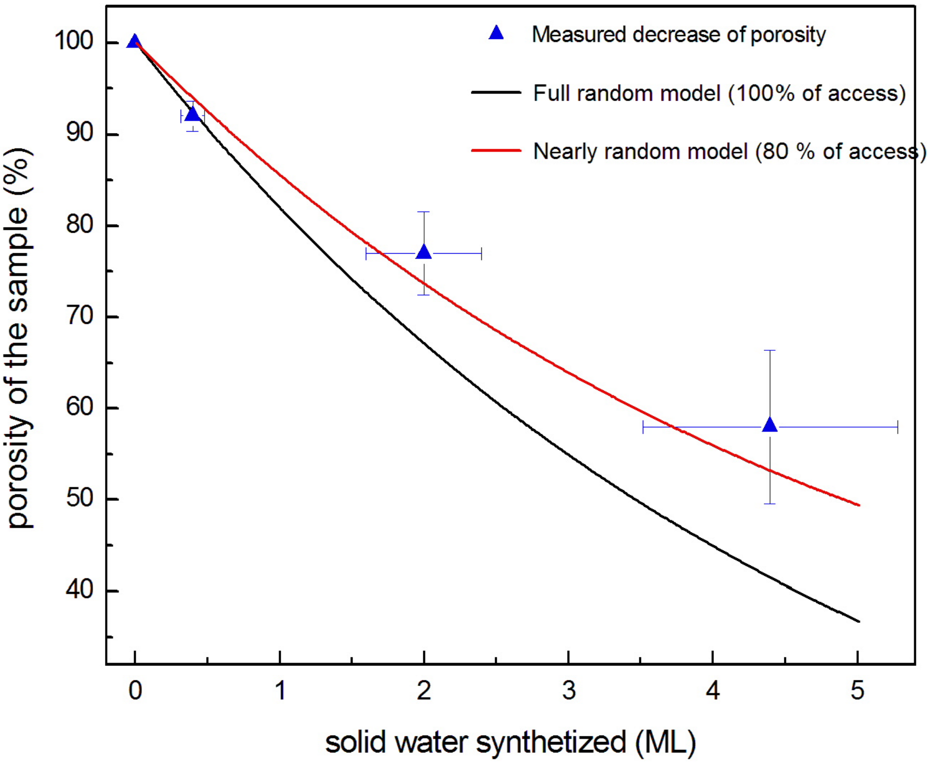

Figure 5.5.4: Decrease of porosity as function of the solid water synthethized on a porous ice substrate. The full triangles show the information about ice porosity extracted by the D_2 TPD profiles in Fig.5.5.2. The solid lines represent the decrease of the ice porosity as estimated by our simple model (see text for details)

number of porous sites available should be scaled by a factor 0.44. A further reasonable improvement of the model should consider that a reaction with one O_2 molecule destroys one adsorption site, therefore scaling the water formation rate by a factor of 0.5. These two factors approximately compensate each other, their combination thereby is not able to explain the light discrepancy between the model and the experimental data.
Inverting the problem, we can verify a discrepancy of about20% between the model and the observed decrease of the porosity. Because of the porous nature of the substrate (that includes tunnels, cracks and voids), it is reasonable that the water ice will be preferentially synthetized on the external edges, and that the sites located inside the thin porous ice layer have a lower probability to be populated, and therefore to be destroyed. Thus, if there is 20% more chance that D_2O is formed on a already compacted site (namely if the assumption of full random access to the sites is not true), then the model will perfectly fit (solid red line in Fig.5.5.4).
In conclusion, we can say that the porosity of the icy substrate is sharply reduced by the formation of water on its surface. It is not due to the D-atoms exposition, and is nearly like a random growth, possibly with the external sites slightly favoured.

5.6 Further experiments planned

The experiments just described allow us to affirm that the solid water synthetized on an icy substrate through the pathway $D + O_2$ has a compact structure. Nevertheless, because of some technical faults occurred to the cryocooler in the set-up FORMOLISM, these experiments were carried out not in the best conditions.
For this reason, further similar experimental investigations has already been planned. Of course, new experiments will be performed maintaining the temperature of the icy substrate at 10 K, rather than 15 K. In the experiments already performed on a substrate of 5 ML of porous ice, we have assumed that 400 s of D-atoms exposure on a film of 0.2 ML of solid O_2 are enough to fully complete the chain of reactions leading to the water formation. Actually, this D-atoms dose has been evaluated just for a compact ice substrate (Fig.5.3.1). Therefore, using a similar procedure, we would perform some experiments in order to establish which is the correct dose of D-atoms for

a highly porous sample. Finally, knowing that FORMOLISM will be soon enriched with an infrared spectrometer, we would like to repeat the same experiments using both the TPD technique and the infrared analysis in situ.

Summary

Water is ubiquitous in space: it has been observed in various astrophysical environments, such as planets, satellites, comets and interstellar clouds. Furthermore, water is by far the most abundant condensed-phase specie observed in the Universe.

In cold and dense interstellar clouds, silicate and carbonaceous dust grains are covered by thin icy mantles (never thicker than 100 ML), consisting mainly of water ice mixed with several other species. To date, the chemical origin of this interstellar ice is still uncertain.

Different pathways probable for water formation in ISM were proposed some years ago by *Tielens & Hagen* (1982). They suggested that H_2O formation would be initiated by H-atoms reacting with O, O_2 and O_3. As recently published by *Ceccarelli et al.* (2007), water formation in the gas phase is believed to be not efficient enough to reproduce the observed abundances. Therefore, water molecules must be synthesized by surface reactions between atoms on cold interstellar grains.

Some of the possible processes for H_2O formation under condition closer to those of dark clouds have been lately investigated. For example, *Miyauchi et al.* (2008) have experimentally analysed the reaction between cold H-atoms and an O_2 ice at 10 K: they observed by in situ infrared spectroscopy the formation of H_2O_2 and H_2O molecules and estimated the efficiency of the reactions. *Ioppolo et al.* (2008) performed a similar experiment but with varying O_2 substrate temperatures: the production of $\mathrm{H_2O_2}$ and $\mathrm{H_2O}$ was confirmed, making an estimate of the reactions upon the temperature dependence about the amount of species produced. In a work not yet published, *Dulieu et al.* (2010) found a rather high efficiency of water formation investigating the interaction between hydrogen and oxygen atoms on an interstellar ice analogue. Finally, I took part in the experimental work recently published (*Mokrane et al.*, 2009) that has for the first time investigated the formation of water molecules via the reaction between ozone and D-atoms.

On the other hand, spectroscopy studies of dark clouds have emphasized that the interstellar water ices are mainly amorphous, namely without any crystalline structure (*Leger et al.*, 1979): for example, the 3.07 μm interstellar absorption band is consistent with the same feature present in laboratory spectra, and due to a pure amorphous ice sample at 10 K. However the real morphology of interstellar ices still remains poorly known.

Several laboratory experiments have stressed the pivotal role of the ice morphology in the gas-ice interaction both in the surface chemistry and in the context of astrochemistry. For example, the fate of the 4.5 eV released after the recombination of two hydrogen atoms on the ice surface is highly dependent on the sample morphology: it has been recently shown experimentally (*Congiu et al.*, 2009) that the atomic hydrogen recombination occurring on the surface of a compact ice releases vibrationally excited molecules in the gas phase, while this behaviour was not observed from a porous ice sample. In other words, the roughness of the surface contributes efficiently to the relaxation of newly formed molecules at the surface.

Porosity appears to be a critical parameter affecting the trapping and the release of a gas as well (*Ayotte et al.*, 2001). Actually, a porous ice film is able to adsorb between 20 and 50 times more gas than a compact. Ballistic deposition simulations (see, for example, *Kimmel et al.*, 2003) provide a picture of a porous ice characterized by a network of nanometric voids that are partially connected together and open to the external surface. Therefore, for a highly porous ice, the effective surface area available for adsorption is much greater than the simple geometric external area of the film (as for the compact ice).

Different ice morphology affects also the desorption kinetics of a gas adsorbed on its surface: the higher is its roughness, the higher is the number of more energetic adsorption sites. Even our study of desorption kinetics of D_2 adsorbed on ASW has stressed this further difference among the characteristics of ices with different morphology: for a highly porous ice, the D_2 desorption peak is found at temperatures higher than those observed in the case of D_2 desorbing from a compact ice.

In the laboratory, ASW is obtained under high vacuum condition by slow vapor deposition of water onto a cold substrate. The morphology of ASW film produced in this way depends on different experimental factors, such as deposition temperature, deposition rate, angular distribution of the incoming water molecules and the thermal history of the ASW film after its formation (*Mayer & Pletzer*, 1986).

In the set-up FORMOLISM used to carry out all the experiments discussed in this thesis, interstellar ice analogues were grown in situ by exposing the cold Cu surface to slow background dosing of water vapour. Non-porous ASW layers were prepared with surface temperature maintained at 120 K, while porous ASW layers were prepared with the surface held at 10 K.

The porosity of ice can be identified in the laboratory through the weak infrared absorption feature ($\sim 2.7\ \mu m$) due to the O-H vibration of dangling bonds on the pore surface (*Rowland et al.*, 1991). According to recent reports (*Keane et al.*, 2001), this feature has never been observed in the interstellar spectra, thereby suggesting (maybe) that the interstellar ices are substantially non-porous.

Experimentally, recent laboratory works carried out under condition closer to those of dense clouds seem to show that the interstellar ices are at least not fully porous. For example, laboratory simulations have verified (*Palumbo*, 2006; *Raut et al.*, 2008) that the cosmic ray bombardment of ice mantles can reduce their porosity over the lifetime of molecular clouds (10^7 yr). Although the details of physical process by which compaction occurs are not fully understood, it is reasonable to think that the energy deposited by the energetic ions is able to rearrange the H_2O molecules, thereby minimizing their surface energy via the removal of pores.

This thesis fits perfectly within the just exposed picture. In fact, as investigated in Chapter 4, it has been observed that relevant changes in the morphology of interstellar ice analogues occur also as consequence of atomic hydrogen exposure. In particular, a thin highly porous ice film is gradually changed into a more compact structure, following D-atoms exposure. Indeed, TPD profiles due to thermal desorption of D_2 from an icy sample[2] shift to-

---

[2] As discussed in the previous chapters, the study of desorption kinetics of gases ad-

wards lower temperatures with increasing the D-atoms exposure, thereby showing a binding energy distribution gradually more similar to that of a compact ice. The phenomenon of ice compaction is probably due to the transient heating caused by the energy released to the ice during H_2 formation, when two hydrogen atoms encounter each other on the icy surface; the local heating thus might change the local morphology, acting like a sort of local annealing. Therefore, even if the water ice is porous at the beginning, the hydrogen recombination on the surface of interstellar ice mantles can compact their structure concurrently with the other envisaged process. But if the energy release during the hydrogen ricombination has an effect in reducing porosity in a porous ice, we may ask which effect this energy has on a compact ice. As compaction cannot occur, it could provoke desorption of adsorbed species or else it could facilitate reactions between adsorbates, by inducing mobility or local annealing. Further experiments to answer to these open questions are thus necessary.

On the other hand, some evidences suggest that the interstellar icy mantles (produced by surface reactions of atoms and radicals or after direct freez-out) come up directly with a compact structure. The validity of such conjecture has been strengthened by our experimental work discussed in Chapter 5. Analysing one of the possible mechanism of water formation (the pathway $H + O_2$) under conditions mimicking those found in a molecular cloud, we have found that the water just synthetized has a non-porous structure. Indeed, the layers of water formed in this way show the kinetic characteristics typical of a compact (non-porous) ice, as for instance the D_2 TPD peak position.

---

sorbed on a water ice film through the TPD technique is a powerful tool that allows to characterize the morphology of the ice sample. In particular, thermal desorption of molecular hydrogen (deuterium) adsorbed on an amorphous ice results particularly sensitive to its porosity.

Bibliography

Amiaud, L., Dulieu, F., Fillion, Momeni, A., Lemaire, J.L. 2007, J. Chem. Phys. 127, 4709

Amiaud, L., Fillion, J. H., Baouche, S., Dulieu, F., Momeni, A., Lemaire, J. L. 2006, J. Chem. Phys. 124, 094702

Ayotte, P., Smith, R. S., Stevenson, K. P., Dohna´lek, Z., Kimmel, G. A., Kay, B. D. 2001, J. Geophys. Res., [Atmosf], 106, 33387-33392

Boonman, A. M. S., Van Dishoeck, E. F., Lahuis, F., Wringht, C. M. & Doty, S. D. 2000 in: *ISO Beyond the Peaks: The Second ISO workshop on Analytical Spettroscopy*, ed. A. Salama, M. F. Kessler, K. Leech & B. Schulz (ESA-SP456; Noordwijk:ESA), 67;

Caselli, P., Stantcheva, T., Shalabiea, O. M., Shematovich, V. I., Herbst, E. 2002, Planetary and Space Science, 50, 1257

Cazaux, S. & Tielens, A. G. G. M. 2002, ApJ, 575, L29

Cazaux, S. & Tielens, A. G. G. M. 2004, ApJ, 604, 222

Ceccarelli, C., Caselli, P., Herbst, E., Tielens, A. G. G. M., & Caux, E. 2007, in Protostars and Planets, ed. V. B. Reipurth, D. Jewitt, & K. Keil

(U. Arizona Press) 47

Chakarov, D. & Kasemo, B. 1998, PhRL, 81, 23

Congiu, E., Matar, E., Kristensen, L. E., Dulieu, F.,Lemaire, J. L. 2009, Mon. Not. R. Astron. Soc. 297, L96-L100

Cuppen, H. M. & Herbst, E. 2007, ApJ, 668, 294

Dohnálek, Z., Kimmel, G. A., Joyce, S. A., Ayotte, P., Smith, R. S., Kay, B. D. 2001, J. Phys. Chem., 105: 3747-3751

Duley, W. W. & Williams, D. A., 1984, Nature, 311, 685

Dulieu, F., Amiaud, L., Congiu, E., Fillion, J. H., Matar, E., Momeni, A., Pirronello, V., Lemaire, J. L. 2010, A&A, in press (*arXiv:0903.3120v1*)

Fillion J. H., Amiaud, L., Congiu, E., Dulieu, F., Momeni, A., Lemaire, J. L. 2009, PCCP, 11, 4396

Fraser, H. J., McCoustra, M. R. S. and Williams, D. A. 2002b, Astronomy and Geophysics, 43, 10

Gibb, E.L., Whittet, D.C.B., Schutte, W.A., Boogert, A.C.A., Chiar, J.E., Ehrenfreund, P., Gerakines, P.A., Keane, J.V., Tielens, A.G.G.M., van Dishoeck, E.F., Kerkhof, O., 2000, ApJ 536, 347

Govers, T. (unpublished); available at *http://hal.ccsd.cnrs.fr/ccsd-00004273/en/*

Hasegawa, T. I., Herbst, E., Leung, C. M. 1992, ApJ Supplement 82, 167

Hollenbach, D. & Salpeter, E. E. 1971 ApJ, 163, 155

Hornekær, L., Baurichter, A., Petrunin, V. V., Field, D., Luntz, A. C. 2003, Science, 302, 1943

Hornekær, L., Baurichter, A., Petrunin, V. V., Luntz, A. C., Kay, B. D., Al-Halabi, A. 2005, J. Chem. Phys., 122, 124701

Ioppolo, S., Cuppen, H. M., Romanzin, C., van Dishoeck, E. F., Linnartz, H., 2008, ApJ 686 1474

Jenniskens, P. & Blake, D. F. 1994, Science, 265, 753

Jenniskens, P., Blake, D. F., Wilson, M. A., Pohorille, A. 1995, ApJ, 455, 389

Katz, N., Furman, I., Biham, O. , Pirronello, V., Vidali,G., 1999, ApJ, 522: 305-312

Keane, J. V., Boogert, A. C. A., Tielens, A. G. G. M., Ehrenfreund, P., Schutte, W. A. 2001a, A&A, 375, L43

Kimmel, G. A., Dohnálek, Z., Stevenson, K. P., Smith, R. S., Kay, B. D. 2001, J. Chem. Phys., 114, 5295 - 5303

Kouchi, A., Yamamoto, T., Kozasa, T., Kuroda, T., Greenberg, J. M. 1994, A&A, 290, 1009

Leger, A., Klein, J., De Cheveigne, S., Guinet, C., Defourneau, D., Berlin, M., 1979, A&A 79, 256

Li, D. & Goldsmith, P. F. 2003, ApJ, 585, 823

Manicó, G., Raguní, G., Pirronello, V., Roser, J. E., Vidali, G., 2001, ApJ Lett., 548, L253

Mathis, J. S. 1996, ApJ, 472, 643

Mayer, E. & Pletzer, R. 1986, Nature 319, 298

Miyauchi, N., Hidaka, H., Chigai, T., Nagaoka, A., Watanabe, N., Kouchi, A., 2008, Chemical Physics Letters, 456, 27

Mokrane, H., Chaabouni, H., Accolla, M., Congiu, E., Dulieu, F., Chehrouri, M., Lemaire, J. L. 2009, ApJ, 705, L195

Oba, Y., Miyauchi, N., Hidaka, H., Chigai, T., Watanabe, N., Kouchi, A. 2009, ApJ, 701: 464-470

Palumbo, M. E., J.Phys. Conf. Ser. 6, 211 (2005)

Perets, H. B. , Biham, O., 2006, Mon. Not. R. Astron. Soc. 365: 801-806

Petrenko, V. F. & Whitworth, R. W. 2002 in: *Physics of ice*, Oxford University Press. ISBN13: 9780198518945

Pirronello, V., Biham, O., Liu, C., Shen, L., Vidali, G. 1997a, ApJ, 483, L131

Pirronello, V., Liu, C., Roser, J. E., Vidali, G., 1999, A&A, 344, 681

Pontoppidan, K. M., van Dishoeck, E. F., Dartois, E. 2004, A&A, 426, 925

Pontoppidan, K. M., Fraser, H. J., Dartois, E., et al. 2003, A&A, 408, 981

Raut, U., Famá, M., Loeffler, M. J., Baragiola, R. A. 2008, ApJ, 687: 1070-1074

Roser, J. E., Manicó, G., Pirronello, V., Vidali, G. 2002, ApJ, 581: 276-284

Rowland, B., Fisher, M., Devlin, J. P. 1991, J. Chem. Phys., 95, 1378

Schlichting, H.; Menzel, D. ReV. Sci. Instrum. 1993, 64, 2013

Smith, R. G., Sellgren, K., Tokunaga, A. T. 1989, ApJ, 344, 413

Smith, R. S., Zubkov, T., Kay, B. D. 2006, J. Chem. Phys., 124, 114710

Snow, T. P., 1980, in *Interstellar Molecules*, ed. B. H. Andrew (Dordrech Reidel), p.247

Snow, T. P. & Witt, A. N. 1996, ApJ Lett., 468, L65+

Sofia, U. J. & Meyer, D. M. 2001, Ap. J., 554, L221-224

Stevenson K. P., Kimmel G. A., Dohnálek Z., Smith R. S., Kay B. D., 1999, Science, 283, 1505-1507

Takahashi, J., Masuda, K. and Nagaoka, M. 1999, ApJ, 520: 724-731

Tielens, A. G. G. M. (2005). *The Physics and Chemistry of the Interstellar Medium*, ISBN 0521826349. Cambridge, UK: Cambridge University Press, 2005.

Tielens, A. G. G. M. & Hagen, W. 1982, A&A, 114, 245

Tielens, A. G. G. M., Tokunaga, A. T., Geballe, T. R., Baas, F. 1991, ApJ, 381, 181

Van Broekhuizen, F. A. 2005, PhD thesis, University of Leiden

Williams, D. A. & Herbst, E., 2002, Surface Sci., 500: 823-837

Wooden, D.H., Charnley, S. B., Ehrenfreund, P., in Comets II, ed. by M. Festou, H.U. Keller (University of Arizona Press, Tucson, 2004), p. 33

Zubkov, T., Smith, R. S., Engstrom, T. R., Kay, B. D. 2007, J. Chem. Phys., 127, 184707

Acknowledgements

The three years just elapsed have been for me full of wonderful and memorable experiences. The most important person in my personal and professional growth has been first of all Professor Valerio Pirronello, who believed in me since the beginning of my Ph.D. experience. His several advices and friendly encouragements helped me through the difficulties I encountered during this period. Moreover, I am deeply grateful to him because he made possible my scientific collaboration with a French team dealing with laboratory astrophysics.

Actually, I spent almost one year and half in the astrophysical laboratory of J. L. Lemaire and F. Dulieu at the University of Cergy-Pontoise (France). At the beginning, it was rather hard to live in France without any rudiments of French language. However, within the laboratory staff, I found immediately an hospitable and comfortable environment, making me feel at once an actual component of the scientific team. Therefore, I am particularly grateful to Professor François Dulieu, the co-tutor of this thesis. He spent a lot of time with me and I learned a lot of things from him, not only about scientific matter. I cannot forget our several conversations about science, French and Italian culture, soccer, fishing and mushrooms.

I owe a special thank-you to my friend Emanuele Congiu who little by little revealed to me all the secrets of the experimental set-up with a lot of enthusiasm. We were not only fellow worker, but we became soon companions, spending times together during the Parisian wild nights!

Thanks to Professor Jean Louis Lemaire, never at a loss for amusing

good stories. He was always very kind to me, sharing with me his knowledge (scientific and not) with a smile.

Special thanks to Dr. Henda Chaaboni, and to my colleagues and room mates Elie and Hakima. They were fundamental for my progressive improvements in French language. Our discussions were continuous exchanges between different cultures: I keep them as precious teaching of my life.

I cannot forget a lot of friends and special people I met during my long French stay, and I still keep them in my heart. The friendship and the time spent with some of them mitigated my homesick.

My gratitude also goes to Dr. Giulio Manicó. His smart suggestions and precise corrections have been fundamental for the final version of this thesis.

I want to thank also Professor Gaetano Giaquinta, coordinator of this Ph.D., for his encouragements during this three years. I am grateful to him because, together with Professor Pirronello, he fought against the Italian bureaucracy so that I could obtain also the French academic title for my Ph.D. .

Finally, I am very grateful to my parents, my brother and my old bosom friends for their lovely support during all the difficult times I lived during this three years.

Dulcis in fundo, I want to thank the little Alice, whom this work has been dedicated. Her generous smiles were for me useful to go ahead with great enthusiasm, during the last harder months.

Catania, December 2009